Inlaid Microfluidics: A Novel Approach to Optical Measurements on Lab-on-Chip Devices

by

Edward Arthur Luy

Submitted in partial fulfilment of the requirements
for the degree of Master of Applied Science

at

Dalhousie University
Halifax, Nova Scotia
December 2020

Contents

List of Tables

List of Figures

Abstract

A novel type of microfluidic optical cell is presented here that inlays black poly(methyl methacrylate) (PMMA) into a clear PMMA substrate to realize an isolated optical channel with microlitre volumes. Optical measurements are frequently performed on microfluidic devices, offering effective, quick, and robust chemical analysis capabilities on small sample volumes. However, sophisticated coordination of light through a small cross-section is needed, often requiring collimating and beam-steering optics. Detailed here is the fabrication process to realize optical cells based on a simple hybrid-material approach. A z-shape microchannel structure crosses a clear-black interface at both ends of the cell, thereby creating integral optical windows that permit light coupling into a microchannel completely embedded in black PMMA. The novel cell design is characterized using typical colourimetric measurements for nitrite, nitrate, phosphate, and rhodamine B with agreement to the literature. Finally, the inlaid cell design is integrated into an automated lab-on-chip nitrite sensor.

List of Abbreviations and Symbols Used

$\sim$	Similar to / Approximately
(β^{-1})	Time Constant
°C	Degrees Celsius
ϵ	Attenuation Coefficient of Species
λ	Wavelength
µ	Micro-
θ_c	Critical Angle
θ_i	Angle of Incidence
A / A(λ)	Absorbance
A_{corr}	Absorbance Minus Background
AU	Absorbance Units
$B_a(\lambda)$	Blank Counts, Absorbance Window
$B_f(\lambda)$	Blank Counts, Fluorescence Window
c	Concentration
C-PC	C-Phycocyanin
CAD	Computer-Aided-Design
Chl a	Chlorophyll a
F.E.D.	Fluorescence Emission Detector
FWHM	Full Width at Half Maximum
F / FL / F(λ)	Fluorescence
GR	Griess Reagent
HAB	Harmful-Algal-Bloom
hr	Hour(s)
I_0	Incident Light Intensity
I	Transmitted Light Intensity
IPA	Isopropyl Alcohol

l	Optical Path Length
LED	Light-Emitting Diode
LOC	Lab-on-Chip
LOD	Limit of Detection
LOQ	Limit of Quantification
M	Molarity
MQ	Milli-Q
n	Nano-
$n(\lambda)$	Refractive Index
NEDD	N-(1-naphthyl)-ethylenediamine dihydrochloride
NH_3	Ammonia
NH_4^+	Ammonium
NO_2^-	Nitrite
NO_3^-	Nitrate
OTS	Off-the-Shelf
PCB	Printed Circuit Board
PD	Photodiode
PMMA	Poly(Methyl Methacrylate)
PO_4^{3-}	Phosphate
$\|R\|_{max}$	Maximum Residual
RFD	Red Food Dye
RMSE	Root Mean Square Error
RT	Room Temperature
S	Sample Intake
S*	Mixed Sample and Reagent
$S_a(\lambda)$	Sample Counts, Absorbance Window
$S_f(\lambda)$	Sample Counts, Fluorescence Window
TIR	Total-Internal-Reflection
UV	Ultraviolet

v/v	Volume-to-Volume (Percent)
V_{bg}	Background Light Voltage Measurement
W	Waste Output
$V_{P,S}$	Photodiode Voltage, Sample
$V_{P,B}$	Photodiode Voltage, Blank
w/w	Weight-to-Weight (Percent)
YFD	Yellow Food Dye

Acknowledgments

The two years that I have spent working on this project have flown by faster than I ever could have imagined. There are a number of people who have supported me along the way, and to them I will always be extremely thankful. It seems only right that I start with my friend Sean Morgan who convinced me to join this project in the first place. What started with a phone call about how much he enjoyed working on this project soon developed into the two of us spending seemingly-countless hours struggling, stressing, and sometimes triumphing in the lab together. We were soon joined by Raha Khosravi, Ben Murphy, and Josh Creelman, and I am immensely proud of all the things we have accomplished together as a group. Beyond that, they are all such fantastic people, and it has been an absolute pleasure to work with them and call them my friends.

Outside of the lab, I have been privileged enough to have some really great people support me. There is no way I could possibly thank all of the people who have been there for me, but my friends Hannah and Eve deserve a special mention. They were there for me two years ago when I was struggling through my undergrad thesis, and somehow they stuck around with me until now to see me do it all again! Whether it was our countless group calls or getting lunch together (sorry Hannah, come visit Halifax!), their friendship has really meant the world to me.

Finally, I want to extend my most sincere gratitude to my supervisor Vincent Sieben. Over the last two years I have been blown away by the amount of passion and dedication he has for our project and for his students. He has always had time to talk about our work no matter how busy he was, and for that I am extremely thankful. Working together with the Sieben lab (as we have called it) has been one of the most enjoyable times of my life, and I look forward to continuing this project together as a team.

Chapter 1

Introduction

1.1 Project Description and Thesis Scope

The purpose of this thesis is to enable the creation of robust low-cost oceanographic sensor systems for wide scale deployment. This thesis focuses on two main sensor systems that are designed to acquire *in situ* measurements of their environment through light absorbance and/or fluorescence measurements. The first type of sensor system is designed to measure concentrations of select nutrients: nitrite, nitrate, and phosphate. The second type of sensor system is designed to use fluorescence measurements as an indicator for potential harmful algal bloom spawns.

This thesis first provides some background on the project. In Chapter 2, the motivation behind the creation of these sensor systems is discussed with reference to current methods of oceanographic variable monitoring. In Chapter 3, the nutrient sensor system is described along with the invention of a novel type of microfluidic light absorbance cell. Some of the more common methods of measuring each nutrient listed above are explored. Nutrient concentrations ranging from 0.1 – 100 μM are measured using varying lengths of the novel light absorbance cell to obtain more sensitive measurements. The microfluidic nature of the optical cell requires microlitre volumes of fluid for even the largest optical cell. The nutrient quantification method that is deemed best-suited for application towards our sensor system is then tested using our novel technology. At the end of the chapter, a complete sensor capable of

deployment is shown with calibration data from a series of nitrite measurement tests.

In Chapter 4, the light absorbance cell of Chapter 3 is modified to simultaneously acquire fluorescence data. This new design is then calibrated using a wide concentration range (0.1 – 10 μM) of a naturally fluorescent dye to evaluate its performance. The integration of this combined absorbance and fluorescence technology towards a more complicated system capable of predicting harmful algal blooms is discussed at the end of the chapter. Finally, in Chapter 5, other potential applications of this technology are discussed as future directions.

1.2 Publications and Conferences

This thesis spans nearly two years of work carried out as a member of the Sieben Lab at Dalhousie University from January 2019 and October 2020. Funding for this research has been provided in part by several parties, including: the Marine Environmental Observation, Prediction and Response Network (MEOPAR), the Natural Sciences and Engineering Research Council (NSERC), the Canada First Research Excellence Fund (CFREF) through the Ocean Frontier Institute (OFI), Innovacorp Early Stage Commercialization Fund (ESCF), and RBR Ltd. This work has also been supported by Dartmouth Ocean Technologies.

Unless when otherwise stated, the work detailed in this thesis is completely my own. Any aspect of this thesis that was performed in collaboration with other(s) is explicitly labeled as such with credit to the person/people involved. Certain sections of this thesis are based on the publications listed below, particularly my first-author peer-reviewed journal article. There is minimal content based on the works of which I was not the first author.

1.2.1 Peer-Reviewed Journal Articles

1 Edward Arthur Luy, Sean Christopher Morgan, Joshua J Creelman, Benjamin J Murphy, and Vincent Joseph Sieben. Inlaid microfluidic optics: absorbance cells in clear devices applied to nitrite and phosphate detection. *Journal of Micromechanics and Microengineering*, 30(9):15, 2020

1.2.2 Peer-Reviewed Conference Proceedings

The following list details my peer-reviewed conference proceedings. This includes abstracts and poster presentations.

1 **Luy, E. A.,** Morgan, S. C., and Sieben, V. J. (2019). Low-cost Microfluidic Nutrient Sensors. Marine Environmental Observation, Prediction and Response Network Annual Conference. Victoria, Canada.

2 Morgan, S. C., **Luy, E. A.**, and Sieben, V. J. (2019). Inlaid Microfluidics for Nutrient Monitoring. The 23rd International Conference on Miniaturized Systems for Chemistry and Life Sciences, (pp. 1714-1715). Basel, Switzerland: Chemical and Biological Microsystem Society.

3 Murphy, B., Morgan, S., **Luy, E.**, Creelman, J., and Sieben, V. J. (2019). Lab-on-a-chip Sensor of In Situ Nutrient Monitoring. OCEANS 2019, (pp. 1 – 7). Seattle, USA: The IEEE Oceanic Engineering Society.

4 Sieben, V. (2020), Microfluidic Nitrate and Phosphate Sensors for Marine Environments, Oceanology, London, UK. Postponed to Dec. 3 due to COVID-19.

1.2.3 Patents

The long-term goal of the work in this thesis is the commercialization of our microfluidic sensors. In March 2019, I helped author a successful application for the Innovacorp Early Stage Commercialization Fund. A collaboration between our lab group and Dartmouth Ocean Technologies soon followed. The work of Chapter 3 provides the foundation of a prototype ocean nutrient sensor in development between our two groups. Similarly, the work of Chapter 4 is in support of an eventual harmful algal bloom detector. Much of the research discussed in this thesis has been to realize and support these eventual greater-complexity systems. The following two provisional patents have followed from work that I have collaborated on:

1 PCT International Application Serial No. PCT/CA2020/050738 – Optical Cell and Methods of Manufacturing an Optical Cell: **Edward A. Luy**, Sean C. Morgan, Vincent J. Sieben.

2 Provisional Patent – Microfluidic Chip, Systems, and Methods for Capturing of Environmental DNA: Joshua J. Creelman, **Edward A. Luy**, Gabryelle Beland, Sean C. Morgan, Julie LaRoche, Mahtab Tavasoli, Robert Beiko, Roger Race, Arnold Furlong, Vincent Sieben.

1.2.4 Manuscripts In-Progress

1 **Luy, E.**, Creelman, J. *et al.* "Simultaneous Absorbance and Fluorescence Using an Inlaid Microfluidic Approach for Harmful Algal Bloom Detection". Based on the work of Chapter 4.

2 Murphy, B., Panzica, K., **Luy, E.** *et al.* Microfluidic Heaters with Application to Nitrate Detection.

Chapter 2

Background

2.1 Ocean Nutrient Concentrations

Dissolved nutrients are essential for the survival of marine life. Nutrients comprised of nitrogen and phosphorus are of particular importance. Nitrogen exists in the worlds oceans in many forms. In order of prevalence: the forms include elementary dissolved nitrogen (roughly 22×10^{15} times more abundant than all others), nitrate ($NO_3{}^-$), ammonia and ammonium (NH_3, $NH_4{}^+$), nitrite ($NO_2{}^-$), and gaseous dinitrogen oxide (N_2O) [2]. Each form, particularly nitrate [3], contributes to the nutrient cycle of natural ecosystems. Phosphate ($PO_4{}^{3-}$), the form of phosphorus that is directly consumed by phytoplankton, is equally important to this cycle [4]. The cycle of these nutrients in the world's oceans is fundamental to the entire food chain.

The concentration profile of nutrients is not homogeneous throughout a body of water. Human industrialization has radically influenced the amount of nutrients in the world's oceans due to nutrient runoff from fertilized land. Oligotrophic[†] and eutrophic [‡] zones provide sub-optimal living conditions for aquatic life. Oligotrophic zones lack a sufficient supply of nutrients needed for consumption by the various lifeforms in the water (*i.e.* phytoplankton). Conversely, eutrophic zones are overly abundant with nutrients and harmful algal blooms (HABs) may spawn. HABs deplete oxygen levels in the water (hypoxia) and can be toxic. Beyond health, HAB proliferation

[†]Low Concentrations of Nutrients
[‡]Excessive Concentrations of Nutrients

has historically yielded significant economic impact [5]. Likewise, shifting ecosystems from anthropogenic induced nutrient changes can also cause species collapses (higher order life) and are a real concern for fisheries and sustainable practices in the ocean. Monitoring nutrient levels is vital towards maintaining habitable waters.

2.2 Lab-on-Chip Technologies and Ocean Sensing

Typically, key nutrients including nitrite, nitrate, and phosphate in water samples from marine environments are measured using benchtop autoanalyzers. While these conventional systems are capable of high-performance, typically nanomolar and micromolar detection limits [6], they are difficult to deploy *in situ* (thus introducing sample transport contamination risks) and consume excessive amounts of sample and reagent (several mL / min).

A number of commercially available *in situ* nutrient sensors exist. Table 2.1 shows the specifications of each of the sensors described in this paragraph. A purely-optical nitrate sensor, the Sea-Bird SUNA V2 UV, uses ultraviolet (UV) light to detect nitrate in its surrounding environment. A clear window separates the internal optics from a fluid reservoir open to the environment. A mechanical arm and brush can be added as an accessory to periodically wipe the optical window. This measure is necessary to correct for biofouling[§] on the window during long-term deployments. With temperature and salinity corrections from external sensors, the SUNA V2 UV advertises a limit-of-detection (LOD) for nitrate of 0.8 μM or 2.4 μM without these corrections. A Deep SUNA variant is also advertised, capable of deployments to 2000 m depths (500 m depth maximum on the SUNA V2 UV). Also available from Sea-Bird is the HydroCycle-PO4 dissolved phosphate wet chemistry sensor. Their sensor

[§]Biofouling: accumulation of microorganisms, plants, algae, or other life forms on wetted surfaces

advertises a 0.024 μM LOD and a maximum sampling rate of four samples per hour. The sensor uses on-board standards to correct for drift during deployments. Reagent consumption is not given but a reagent shelf-life of 5 months is described. The range of the sensor is 0 – 10 μM. Similarly, the WIZ Probe by Systea is capable of measuring nitrite, nitrate, and phosphate among other species. Depending on the species, its range of detection is between 0 – 10.5 μM. Each of these sensors, however, are fairly large ($>$ 1300 cm^3) with significant power consumption (1 – 8 W) and expensive (tens of thousands of dollars Canadian per unit). Likewise, excessive reagent consumption by the wet chemistry sensors remains an issue for long-term deployments.

Table 2.1: Select commercial *in situ* nitrate, nitrite, and phosphate sensors. UV refers to ultraviolet optical measurements while WC refers to wet chemistry. Wet chemistry methods are given superscripts 1 – 3 referring to the modified Griess reaction, the Griess reaction, or the blue phosphate method (described later in Chapter 2). Specifications are accurate as of November 2020 and may be subject to change. [a]Requires external temperature and salinity correction. [b]Accuracy of 2 μM or 10 % of reading, whichever is greater.

Sensor	**SUNA V2 UV**	**Deep SUNA**	**WIZ Probe**			**HydroCycle PO4**
Species	NO_3^-	NO_3^-	NO_3^-	NO_2^-	PO_4^{3-}	PO_4^{3-}
Method	UV	UV	WC[1]	WC[2]	WC[3]	WC[3]
Accuracy (μM)	2	2[b]	N/A	N/A	N/A	N/A
Range (μM)	N/A	3000	8	5.4	10.5	10
LOD (μM)	0.8[a] / 2.4	0.5[a] / 2.0	0.081	0.065	0.063	0.024
Drift (μM/hr)	$<$ 1.0	0.3[a] / 1.0	N/A	N/A	N/A	N/A
Power (W)	7.5	7.5	3 - 8	3 - 8	3 - 8	1 - 2
Weight (kg)	5.1	1.8	N/A	N/A	N/A	7.6
Volume (cm^3)	1748	1384	N/A	N/A	N/A	$\sim$14000
Depth (m)	500	2000	10	10	10	200

In contrast to the described commercial sensors, lab-on-chip (LOC) platforms miniaturize standard analysis techniques to reduce sample volume per measurement. Using fluid channels of sub-millimetre cross-sections, sample volumes of micro- or nano-litre volumes may be interrogated. Specifically, microfluidic technologies have been suc-

cessful in performing chemical analysis methods on automated and portable sensor systems. Several analytical techniques have been implemented on microfluidic devices, including fluorescence microscopy [7], electrophoresis [8], chemiluminescence [9], and Raman spectroscopy [10] among others [11]. Microfluidic implementation of these mainstay techniques has improved resource-efficiency by reducing sample and reagent volume usage per measurement. Fluid optimization is even more important for automated instruments or *in situ* sensors that are intended for remote deployments, which may span multiple years and/or perform thousands of measurements [12]. For example, comprehensive temporal and spatial monitoring of large, dynamic environments like the world's oceans is challenging. This is due to manual collection, preservation, storage and/or transportation of samples for analysis in an on-ship laboratory cabin or an on-shore facility. The high reliance on qualified labour and the cost to manually retrieve samples has resulted in marine environments being severely under-sampled. Ideally, resource efficient sensors would measure the sample at source, thereby negating the need for the above manual process.

Microfluidic technologies have been applied to measure these nutrients *in situ* with reduced volume and reagent consumption. Many microfluidic sensors described in the literature rely on spectrophotometric methods to probe small volumes of fluid in microchannels. These approaches are inexpensive and yet reliable, making them suitable for automated chemical analysis in challenging environments. In the last 10 years there have been numerous examples of spectrophotometric sensing on microfluidic platforms in ocean/marine environments, measuring: nitrite [13, 14, 15], nitrate [13, 16], phosphate [4, 17, 18, 19, 20], ammonia [21, 22] chromium [23], iron/cobalt [24]; pH [25], and silicate [26]. The core component in each sensor is the design of low volume and long path length optical cells. This requires controlled alignment of light through the liquid/fluid sample for detection without background interference

from non-directional and/or ambient light.

A microfluidic optical cell may utilize screwed-in or epoxy-fixed fibers to couple light to/from on-chip waveguides and flow cells for sample inspection [22, 27]. However, fiber-based lab-on-chip sensor designs tend to be less transferable from the lab to the field, where slight mechanical shocks/vibrations can result in reduced optical coupling and sensor measurement error. Further, respecting the necessary bend radius of fiber-based systems presents a physical integration challenge for compact sensors and miniaturization. Alternatively, low-cost robust optical measurements may be realized by using the chip material itself. Sieben *et al.* formed a completely integrated absorbance cell in chips fabricated from carbon-doped (tinted) semi-transparent poly(methyl methacrylate) (PMMA) [14]. Using this approach, light transmittance and measurement was achieved through thin windows which permitted a light-emitting diode (LED) light source and a photodiode detector to be directly coupled to a 2.5 – 10 cm fluid flow cell. When light does not pass through the fluid microchannel, it is mostly attenuated elsewhere on the chip. This optical cell has been successfully applied to various microfluidic sensors [4, 13, 28, 26] that have been deployed in marine environments to acquire thousands of measurements over multi-month durations. While the tinted approach to realizing microchannel absorbance cells provided a reliable core component for lab-on-chip marine sensors, it is based on a challenging alignment and fabrication process. Either UV-curable or time setting two-part epoxies completely immerse the LED and photodiode to hold them in perfect alignment to the microchannel. This requires a skilled and tedious workflow during the manufacturing process of these devices, where measurements must be taken to ensure optical alignment. The manufacturing challenges pose a significant problem to the low-cost mass-production of these LOC sensors.

2.3 Absorbance Spectroscopy and Nutrient Detection Methods

Absorbance spectroscopy is a common and well-established technique for biological and chemical analysis, either in continuous or stopped-flow configurations [29]. It is a simple, quick, and robust method of detecting the presence of a species within a fluid provided the analyte concentration is relatively low and that it has an accessible/unique absorbance spectrum. Incident light passing through a sample will attenuate depending on the molecular absorbance spectrum of the sample, the scattering from particles in the fluid, and the spectrum of incident light. For molecular absorbance, the molecules within the analyte may become excited and thus absorb energy from the incident waves as electrons are promoted to higher energy bands. The relative drop in light energy – or equivalently its intensity – can be used to calculate the absorbance of the sample using the Beer-Lambert law,

$$A = -\log_{10}\left(\frac{I}{I_0}\right) = \epsilon l c, \tag{2.1}$$

where absorbance A depends on the ratio of incident to transmitted light intensities, I_0 and I, respectively. The intensities are used to find the concentration c of the absorbing species as a function of the optical path length l and the attenuation coefficient of the analyte [30]. Here, the effects of scattering attenuation can largely be ignored as the fluid samples are sufficiently filtered (*i.e.* samples are prepared with highly-filtered Milli-Q water or environmental samples are pulled through a filter at the intake). The Beer-Lambert law is intended for dilute samples and can produce non-linear correlations if excessively high-concentrations are used. Significantly, the detection sensitivity has a linear dependence on the length of the optical channel: a challenge for microfluidic devices that aim to minimize physical size. This has prompted the use of techniques like cavity ring down spectroscopy [31].

Colour-developing reagents are used to enable measurements via light absorbance. A reagent is chosen that produces colour only in reaction with the targeted species. For example, to measure the amount nitrite in a standard[¶] via light absorbance, the standard would be mixed with a colour-developing reagent that is selective to nitrite. The selectivity of the reagent ensures that other potential species in the standard do not produce colour as well. In principle, the reagent will react with each molecule in the sample under investigation to produce dye. The resultant mixture, referred to as the sample[‖] from here, will develop colour as the reaction progresses and plateau when the reaction completes and each nutrient molecule is converted to dye. The more dye present in the the fluid, the more the sample will absorb.

Before measuring fluids of unknown nutrient concentrations, the light absorbance of a number of standards with known concentrations is typically measured: this produces what is referred to as a calibration curve. When measuring sufficiently dilute samples (*i.e.* samples that produce absorbance values less than 1), the calibration curve is typically a linear relationship with slope M. The calibration curve is then used to determine the concentration c of any unknown fluid by measuring its light absorbance A and solving $c = A/M$.

2.3.1 Nitrite: Griess Reaction

Light-absorbance measurements of nitrite samples reacted with the "Griess" reagent is considered a gold-standard approach and has been described in great detail elsewhere [32, 33]. Under acidic conditions, a purple azo dye with peak absorbance near 540 nm will form in the presence of nitrite. Using a monochromatic light source centered near the peak of the azo dye absorbance spectra, nitrite has been measured to an

[¶]Standard refers to a homogeneous fluid of a set concentration of nutrient(s)
[‖]Sample = standard + reagent

LOD in the nanomolar range [13, 14]. The Griess reaction is typically performed by mixing a *standard* that contains an unknown concentration of nitrite with an equal volume of Griess reagent. The reagent is prepared in excess such that each molecule of nitrite is converted into a molecule of azo dye. The concentration of azo dye in this mixed *sample* is then measured using light absorbance. The concentration of nitrite that was present in the initial sample before mixing is then equal to twice the concentration of azo dye, since both fluids were mixed in a 1:1 volumetric ratio.

2.3.2 Nitrate: Reduction

Nitrate is orders-of-magnitude more abundant than nitrite in most marine environments and plays a more significant role in the aquatic ecosystem. Nitrate concentrations may vary: for example, 0.1 – 7 μM in the Bedford Basin in Nova Scotia, Canada. Unlike nitrite, nitrate lacks a good colour-developing reagent for light absorbance measurements. The conventional approach to measuring nitrate is a two-step method. First, in the reduction step, all nitrate molecules in the sample are reduced to nitrite molecules using a reduction-oxidation reaction and an appropriate reducing agent. Second, in the colour-development step, the resultant molecules of nitrite are converted to azo dye and measured using the Griess reaction and light absorbance.

Typically, an environmental sample will contain both nitrate and nitrite. Since the described method measures nitrate by reduction to nitrite, the initial concentration of nitrite in the sample will offset the nitrate measurement. If the concentrations of both nitrate and nitrite are desired individually, two measurements may be made. First, the initial concentration of nitrite in the sample is measured using the Griess reaction. Next, the nitrate molecules in that same sample are reduced to nitrite and the Griess reaction is used again. This gives the total nitrite concentration (reduced

nitrate and original nitrite). The concentration of nitrate that was present in the sample is then calculated such that:

$$[NO_3{}^-] = \Delta[NO_2{}^-] = [NO_2{}^-]_f - [NO_2{}^-]_i. \tag{2.2}$$

When a sample contains only nitrate, equation (2.2) simplifies to $[NO_3{}^-] = [NO_2{}^-]$ and only one measurement is needed.

Reduction of nitrate to nitrite is required for most spectrophotometric detection methods, with the use of cadmium as reducing agent being the gold-standard approach for its high reduction efficiencies and short procedures [13]. The use of cadmium, however, brings associated health risks (toxicity; carcinogenic e.g. see [34]). Likewise, its reduction efficiency varies with time based on the amount and type of samples [35] and other factors like flow rate and sample pH, salinity, and temperature levels [13].

An alternative approach is the use of hydrazine in the presence of copper ions as a catalyst for reduction. Mullin and Riley studied reduction of nitrate via several different reducing agents and found hydrazine to produce efficient reduction rates in alkaline solutions near 85 % [35]. This reduction requires reaction catalyzation by sufficient concentrations of copper ions, beyond that which is found naturally in sea water [35]. Henricksen outlines that this method is advantageous due to high detection sensitivity and stability, but explains the strict adherence needed to set pH and temperature levels for at least 20 hours of reduction time when analyzing sea water [36].

Miranda et al. in 2001 [37] first presented a method for simultaneous nitrate and nitrite measurement, using vanadium (III) chloride as the reducing agent and the Griess method to quantify the resultant nitrite. The work of García-Robledo, Corzo, and Papaspyrou [3] details improved methods for reduction via vanadium (III) chlo-

ride, including higher reduction efficiencies and corrections of reaction impacting factors. Reduction results are compared against the cadmium-column reduction method, showing a high level of agreement between the two for samples collected from a variety of water sources with < 30 µM NO_3^- + NO_2^- concentrations. The use of vanadium (III) chloride as the reducing agent has gained traction in recent times for these reasons: combining performance and safety.

While the nitrite to dye conversion of the Griess reaction is rapid (1 – 5 minutes, [14]), the reduction step using vanadium (III) chloride may take several hours at room temperature (RT). However, García-Robledo, Corzo, and Papaspyrou [3] among others have accelerated the reduction step using heat. They found that temperatures near 30 – 50 °C have been optimal to accelerate the process, with analysis times dropping from hours to minutes.

2.3.3 Phosphate: "Yellow Method"

One of the mainstay techniques of phosphate detection is through combination with an acidic ammonium molybdate / metavanadate based reagent, hereby referred to as yellow phosphate reagent, which forms a yellow complex proportional to phosphate concentration with maximum absorbance in the UV region [38] at 375 nm [39]. As with the Griess reaction, a molecule of dye is formed for every molecule of phosphate present in the sample (assuming the reaction kinetics are satisfied, 1-5 min for complete reaction [39]). Phosphate concentration can be quantified using light absorbance measurements of the resultant dye. This method has been an attractive candidate for *in situ* phosphate sensors due to the stability of the reagent: reported to be over a year [39]. The use of UV light for excitation, however, may make aligning optics difficult for these sensors. UV light is not within the visible spectrum: thus, alignment

is difficult without a light detector measuring in this region. Likewise, high-intensity UV light sources are dangerous to work with.

2.3.4 Phosphate: "Blue Method"

A second method of phosphate detection, referred to in the literature as the molybdenum blue method, was first described in 1962 by Murphy and Riley [40]. Their original manuscript has accumulated tens of thousands of citations (ScienceDirect, Mendeley) as evidence of the widespread use of this method. Again, a reagent is mixed with a sample containing phosphate and a dye is formed with an absorbance peak near $\lambda = 882$ nm. A second slightly lower peak exists near $\lambda = 700$ nm. This method has been implemented by several groups on their microfluidic sensors for applications ranging from benchtop testing [19] to multi-week/month long deployments [4, 41]. Using this method, an LOD of 40 nM was reported by [41] through excitation by a light source centered at 700 nm.

2.4 Fluorescence

As with absorbance spectroscopy, fluorescence involves excitation of a species with an incident light source. A portion of the incident light may be absorbed by the species depending on its absorption spectra and the range of wavelengths contained within the beam. Upon excitation, a portion of the energy transferred to the molecule may be released as light while the rest of the energy is released via other forms: vibrational and rotational translations [30]. For every photon initially absorbed, the energy of the photon is equal to $E_i = hc/\lambda_i$, where E is energy, h is the Planck constant, c is the speed of light (in vacuum), and λ_i is the wavelength of the absorbed photon. The energy re-emitted as fluorescence is less than the incident energy due to the described

vibrational and rotational losses: thus $E_i > E_f$. From this, it can be seen that the wavelength of the emitted light must be greater than that of the incident light:

$$\begin{aligned} E_i &> E_f \\ \frac{hc}{\lambda_i} &> \frac{hc}{\lambda_f} \\ \frac{1}{\lambda_i} &> \frac{1}{\lambda_f} \\ \therefore \lambda_f &> \lambda_i \end{aligned}$$

From this, it follows that the fluorescence and absorption spectra of a sample are not the same. For every photon absorbed, a photon of a longer wavelength is re-emitted. When the absorption and fluorescence spectra of a species are known, they can be a used to determine the presence of that species in a sample. The sample is interrogated using one or more light sources depending on the absorption spectra of the species to be measured. In each case, the amount of light that is absorbed can be measured as described in Section 2.3. Simultaneously, the amount of light re-emitted by fluorescence at a different wavelength to the incident light can be measured. If the absorption and fluorescence spectra of the sample contain peaks that agree with the known spectra of the species in question, that suggests the presence of the species in the sample.

When a species emits fluorescence, it does so uniformly in every direction. As such, fluorescence is typically measured in a direction perpendicular to the incident light beam to most effectively avoid detection of the incident beam itself. This is significant to the design of a fluorescence sensor. For example, if the light detector used cannot differentiate between wavelengths, as is the case with a simple light-to-voltage converter, the incident beam and the fluorescence can not be distinguished from one-another. If a more sophisticated detector is used, *i.e.* a spectrometer that uses a

diffraction grating to measure light at different wavelengths, the incident beam may still interfere with measurements by saturating the detector. A sensor that measures fluorescence at an angle orthogonal to the incident beam best avoids these issues.

Significantly, fluorescent pigments like chlorophyll a (Chl a) and c-phycocyanin (C-PC) may both serve as indicators of cyanobacterial biomass in an aquatic environment. Chl a is found in all microalgae while C-PC is more selective to harmful algae. Both pigments have unique absorption and fluorescence spectra and may be measured simultaneously to identify HAB-susceptible regions. In certain cases, HABs may proliferate to the point that they can be identified from space via satellite [42]. Satellite imagery, however, cannot detect HABs below the surface layer due to the attenuation of electromagnetic waves with depth. Likewise, measurements via satellite are less sensitive than those of an *in situ* sensor. For these reasons, an *in situ* sensor could drastically improve ocean HAB monitoring efforts with higher resolution data acquisition.

2.5 Ocean Variable Monitoring With Profiling Vehicles

Lab-on-chip systems present a unique opportunity for deployment on vehicles with strict restrictions on payload size, weight, and power draw. A lab-on-chip sensor capable of *in situ* sampling and measurement analysis for extended deployment periods may collect and/or transmit data for thousands of individual measurements while still adhering to these payload restrictions.

The Argo program is an example of where these lab-on-chip sensors may be of particular value. Thousands of profiling floats are deployed around the world to provide near real-time measurements of key ocean variables at set depth intervals [43]. Data are typically acquired via transmission to satellite each time the profiling float as-

cends to the surface. These floats have historically profiled depths of at least 2000 m per cycle. At typical profiling speeds, to acquire data with a resolution of 1 m would demand a measurement throughput of once every 10.8 seconds [44]. Over a 1 year deployment span with 40 profiles a year and one measurement per meter, 80000 measurements would be needed. According to [45], ARGO floats on average have a length of 3.5 feet and a diameter of 8 inches. Approximating the float as a cylinder, this equates to a volume of 34.6 L. For such a deployment, a sensor on an Argo float must remain small enough in terms of physical size and weight after as many as 80000 measurements to not overburden the Argo: a challenge for conventional sensors that may need to store several millilitres of fluid per measurement. However, a lab-on-chip system that consumes for example 10 μL per measurement would add only 800 mL of waste: approximately 2 – 3 % of the Argo's initial weight. For this reason, these LOC sensors may be unique in their compatibility with these small vehicles without compromising measurement performance.

Chapter 3

Light Absorbance via Inlaid Microfluidics

This chapter is partially based on the published manuscript "Inlaid microfluidic optics: absorbance cells in clear devices applied to nitrite and phosphate detection" by myself, Sean Morgan, Joshua Creelman, Benjamin Murphy, and our supervisor Vincent Sieben. The invention of the described "inlay" technology was an equal collaboration between myself and Sean Morgan. Likewise, the system integration section was a group effort between Joshua Creelman, Benjamin Murphy, and I. All other work in this chapter is entirely my own.

3.1 Introduction

The manufacturing challenges discussed in Chapter 2 to realize optical cells in lab-on-chip devices are addressed here with a novel microfluidic optical cell applied to light absorbance measurements. This optical cell is created by inlaying[†] one material into another and has thus been named an "inlaid optical cell". An advantage of this optical cell is that it does not rely on epoxies to align or hold the source and detector. The inlaid optical cell is comprised of sections of opaque and transparent material to achieve light transmission through a microfluidic channel that is almost entirely isolated from background light interference. Thus far, the choice of material to realize these inlaid optical cells has been poly(methyl methacrylate); in theory, however, the approach should extend to most materials used to create microfluidic

[†]Inlaying: to embed one material into another flush with its surface

chips. Black/opaque PMMA is inlaid into clear/transparent PMMA to realize the optical cell. A concept computer-aided-design (CAD) of this optical cell is shown in Figure 3.1 and Figure 3.2. A z-shape microchannel structure crosses a clear-black interface at both ends of the absorbance cell, thereby creating integral optical windows (labelled in Figure 3.1) that permit light coupling into a microchannel completely embedded in black PMMA. Black material surrounds the fluid sensing channel to ensure that light is transmitted from one side to the other exclusively through the channel. The design uses v-groove prisms, like Grumann *et al.* [46], to couple light into and out of the channel from an external light source to a detector. Instead of the large channel cross-section described in Grumann *et al.* (1 mm deep × 10 mm wide × 10 mm long, 100 μl cell volume), the black/inlaid PMMA enables small channel cross-sections, hence, a small volume absorbance cell (0.6 mm deep × 0.4 mm wide × 10.4 mm long, 2.5 μl cell volume). Described here is a complete fabrication process

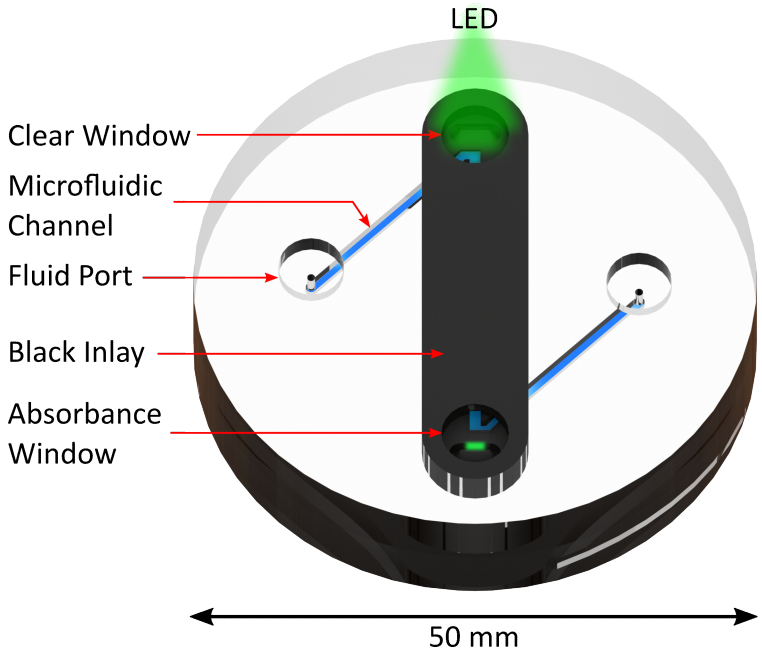

Figure 3.1: Inlaid light absorbance cell concept – top view

to realize microfluidic chips based on this inlaid approach and the CAD of Figure

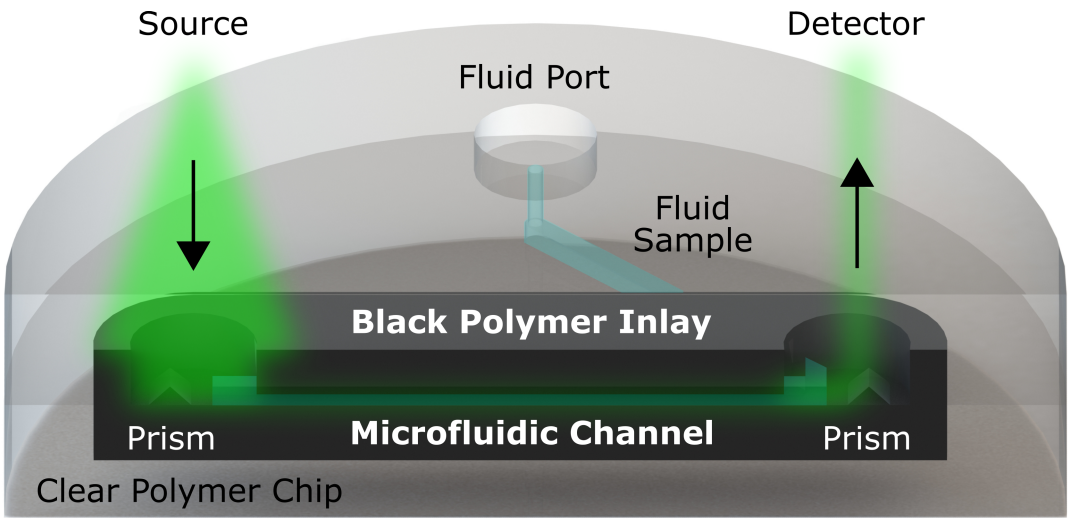

Figure 3.2: Inlaid microfluidic light absorbance cell concept – cross section view

3.2. In Figure 3.3(a), a photograph of a microfluidic chip is shown containing three separate inlaid optical cells. The smallest optical cell, 10 mm long, uses 40 times less volume than the described works by Grumann *et al.*; however, smaller designs can be achieved if desired with further process optimization, *i.e.*, better light collection efficiencies. Shown in Figure 3.3(a) is the activation of the 25 mm long optical cell. An LED light source is held above the first prism which directs light into the channel using total-internal-reflection (TIR). A photodiode detector is held above the second prism, which directs light from the inlaid microchannel to the detector (not shown for the purposes of the picture). The opaque PMMA surrounding the optical cell is critical to prevent light-scattering throughout the rest of the chip. In Figure 3.3(b), an optical cell with the same path length but fabricated without the inlay is shown. A beam can be seen at the second prism, but a portion of the beam is comprised of light that has scattered throughout the chip (and has not passed through the sample). A large amount of light scattering can be seen throughout the chip. In Section 3.2.2, the negative influence of light-scattering on light absorbance measurements will be discussed. The inlay design permits long path lengths on the order of 1 – 10 cm,

while maintaining low sample volumes; e.g. a 50.4 mm cell has a volume of 12.1 μl. Before fabrication, the efficacy of the inlaid design in Figure 3.2 was evaluated

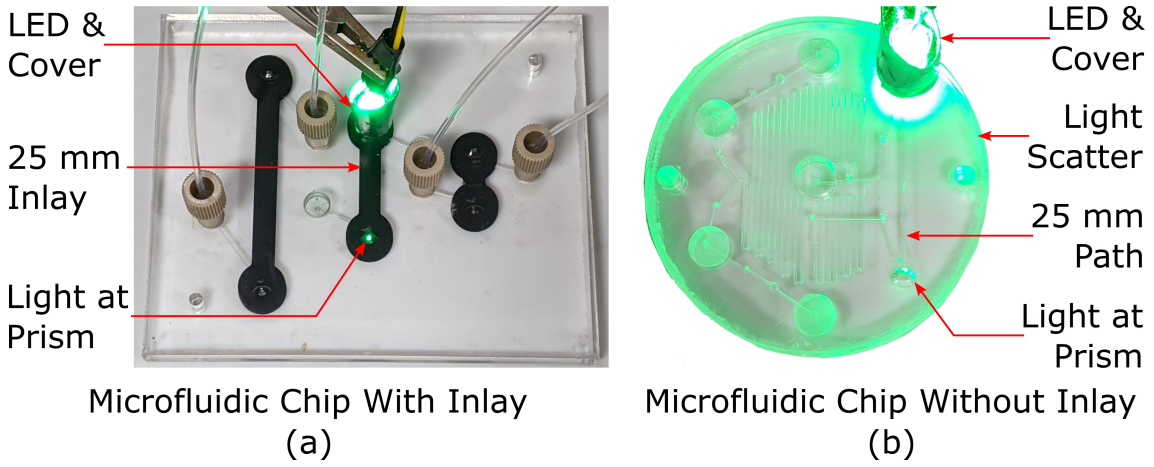

Figure 3.3: Inlay vs. non-inlay comparison (photographs). Light scattering is minimal in (a) and severe in (b).

with ray-tracing software (Zemax, Washington, USA) as shown in Figure 3.4(a)-(b). The first graph depicts the measured amount of light sourced from an uncollimated LED that passes through the input optical window and is directed towards the first prism. The second graph depicts the amount of light that is measured from the second prism after passing through a 25 mm inlaid microfluidic cell. Each graph provides the luminous flux per unit area in Lumens/cm^2 with origin at the center of the prism. Observed by the detector (Figure 3.4(b)) is a focused beam with a narrower spatial distribution and $<$ 10 % of the intensity of the incident light. Collimating optics or fibers are unnecessary to saturate a simple light detector through even a 25 mm long path as simulated here. As an alternative, light could also be coupled directly through the channel from the side of the chip, as is done with the tinted-approach [13, 14]. The prisms, while not necessary, were implemented for the benefit of applying and detecting light from the topside of the chip. Interfacing the optical elements through the topside permits the light source and detector to be soldered components on a printed circuit board (PCB). The PCB can be held directly above the chip for

rapid signal processing without any external wiring/connectors. This design is highly manufacturable, as repeatable and robust optical alignment can be achieved through standard manufacturing practices of component placement on PCBs. Furthermore, the inlaid approach makes it simple to change the LED and photodiode combination for different chemistries on the same chip design without detaching the optics/epoxy fixatives that would risk damaging the microfluidic chip. Therefore, the cell could be configured quickly for a variety of chemistries without risk of compromising the optical quality of the optical cell.

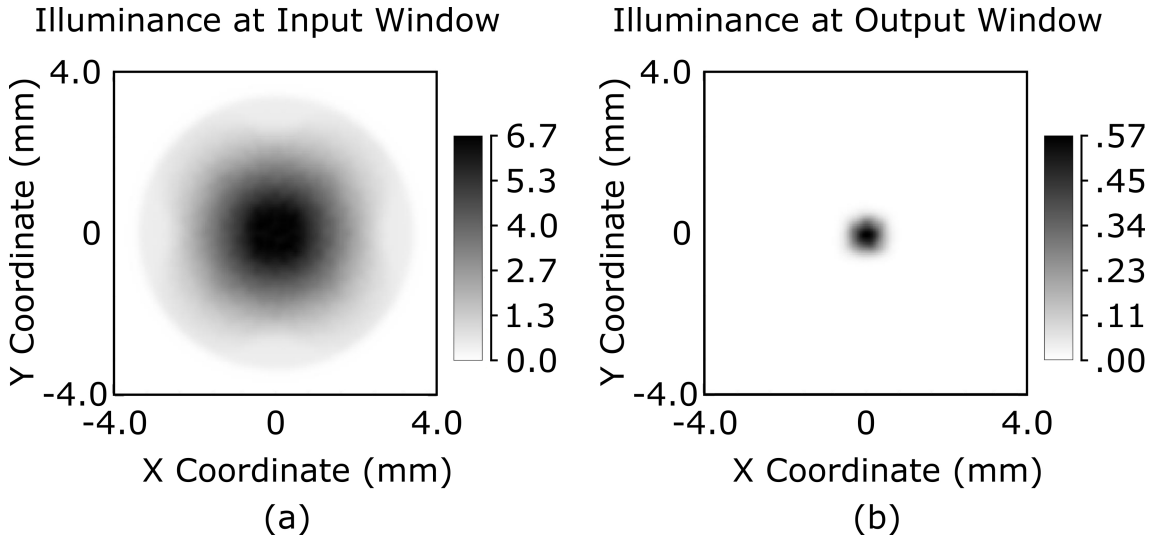

Figure 3.4: Zemax ray-tracing simulations. The luminous flux per unit area (Lumens/cm^2) is plotted at both the (a) input and (b) output windows of a 25 mm long inlaid optical cell.

3.1.1 Application to nutrient detection

To validate the novel optical cell, three nutrients fundamental to aquatic ecosystems were measured: nitrite, nitrate, and phosphate. Nitrite samples were measured using light absorbance and the Griess reagent as described in Chapter 2 Section 2.3.1. Nitrate samples were measured using nitrate reduction and the Griess reaction as

described in Chapter 2 Section 2.3.2. Phosphate samples were measured using both the "yellow" and "blue" methods described in Chapter 2 Section 2.3.3 and Section 2.3.4. Each chemistry is measured using at least one of the following optical path lengths: 10.4, 25.4, and 50.4 mm. It is shown that the inlaid microfluidic absorbance cell produced results in agreement with the literature for every tested optical cell.

Following validation of the optical cell as an isolated system, a custom lab-on-chip nitrite sensor was successfully built with Joshua Creelman, Benjamin Murphy, and Sean Morgan to measure nitrite. Both a 10 mm and a 25 mm inlaid optical cell were used, integrated with 4 on-chip check valves to control fluid flow. The added-complexity that arose from the complete system with its influence on the acquired data will be discussed.

3.2 Theory

3.2.1 Snell's Law and Total-Internal-Reflection

In the work presented here, light absorbance measurements are enabled by transmitting light from an LED through various fluids contained in a microfluidic channel to a light-to-voltage converter (photodiode) for detection. To couple light into and out of the channel, prisms are employed. According to Snell's law, light of wavelength λ will TIR at the PMMA-air prism interface, so long as the angle of incidence θ_i exceeds the critical angle θ_c:

$$\theta_c = \sin^{-1}\left(\frac{n_2(\lambda)}{n_1(\lambda)}\right) \tag{3.1}$$

where $n_1(\lambda)$ and $n_1(\lambda)$, the refractive indices of PMMA and air, are functions of the

light wavelength λ. As such, the interface of both prisms are angled 45° relative to the incident beam to satisfy the reflection condition while allowing both source and detector to be held perpendicular to the chip. This design choice allows for simple alignment between optical components and the chip, while also enabling a future design whereby optical components may be soldered to the bottom of a PCB mounted above the chip.

3.2.2 Absorbance Spectroscopy

As discussed in Chapter 2 Section 2.3, absorbance spectroscopy is a tool used to quantify concentration via light absorbance. In this work, a light-to-voltage converter is used to measure light intensities. A voltage is measured from the light-to-voltage converter that is proportional to the intensity measured; equation (2.1) can therefore be rewritten in terms of voltage instead of intensity:

$$A = -\log_{10}\left(\frac{V}{V_0}\right) = \epsilon l c, \tag{3.2}$$

where V and V_0 are the voltage readings produced by the light-to-voltage converter in response to I and I_0 respectively. These equations, however, assume that all measured light has reached the detector having passed fully through the optical cell and does not account for the detection of any background sources of light (i.e. ambient room light, light directly from the light source). Interference from background light must be quantified or otherwise minimized. Equation (3.2) may be modified to eliminate

these external influences and is expressed in the following equivalent forms:

$$A_{corr} = -\log_{10}\left(\frac{V_{P,S} - V_{bg}}{V_{P,B} - V_{bg}}\right) \tag{3.3a}$$

$$= A + \log_{10}\left(\frac{1 - V_{bg}/V_{P,B}}{1 - V_{bg}/V_{P,S}}\right) \tag{3.3b}$$

$$= A + \delta, \qquad (\delta \geq 0) \tag{3.3c}$$

where $V_{P,S}$ $V_{P,S}$ and $V_{P,B}$ are the photodiode voltage readings when measuring a sample or blank, respectively, and V_{bg} is the voltage measurement of the detector when measuring only the background light. In equation (3.3c), the corrected absorbance measurement A_{corr} is expressed in terms of the uncorrected absorbance measurement A plus a correction term δ. In practice, δ is always greater than zero when background light is detected; thus, the corrected absorbance measurement is always larger than the uncorrected absorbance measurement. This effect scales with the magnitude of A such that more absorbent samples are more susceptible to the same magnitude of background light than dilute samples. Elaboration on these points, including the derivation of equation (3.3c), may be found in Appendix A with further discussion in the supplemental material of [1].

Equation (3.3c) requires that, when measuring the light absorbance of a sample, the amount of background light observed by the detector must be quantified. Measuring the light observed by the detector with the light source turned off provides a good approximation of V_{bg} for use with equation (3.3c), so long as this value remains relatively constant over time. If the amount of background fluctuates with time, the background light must be reassessed for each absorbance measurement. An important consideration of any optical cell, therefore, is to both diminish and minimize fluctuations in the detection of background light.

3.3 Materials and Methods

3.3.1 Fabrication

The complete fabrication process to create inlaid microfluidic devices is described and is the shared result of myself and Sean Morgan. A CAD of the chip fabricated in this section is shown in Figure 3.5 and contains three separate inlaid optical cells of varying path lengths. First, from a sheet of opaque or black extruded PMMA (9M001, Acrylite, USA), two pieces were cut out to form a top and a bottom "insert" that are the basis of the inlaid optical channel. The black PMMA inserts were shaped like a dumbbell. The top insert had a straight thin section bounded on either side by rounded ends, $d_{out} = 11$ mm. The top insert also had inner concentric cylindrical cuts, $d_{in} = 5$ mm, to allow for light coupling to the prisms. The bottom insert was identical but without the cylindrical cuts to block/absorb light not reflected off the prisms. The length of each insert depended on the desired length of the optical channel; for example, a 50.4 mm channel insert would measure 50.4 mm between the center of each rounded end. Second, the associated cavities for each insert were machined into a separate sheet of clear extruded PMMA (0A000, Acrylite, USA) for each insert to be pressed into. These cavities were of matching dimensions to their corresponding insert except with an added tolerance of 25 μm on all sides – necessary to compensate for microscopic deformities and imprecise milling – so that the inserts fit tightly within the cavities. Next, the inserts and cavities were fused with a solvent, thermal, and pressure process. The alignment of the inserts and the cavities is shown in Figure 3.6. It was important to achieve a fluid-tight seal between the cavity and the insert such that there were no gaps of empty space upon inlaying. This would ensure uncompromised fluid handling across clear and black sections of the substrate. To achieve a seamless bond between the two plastics, we explored solvent

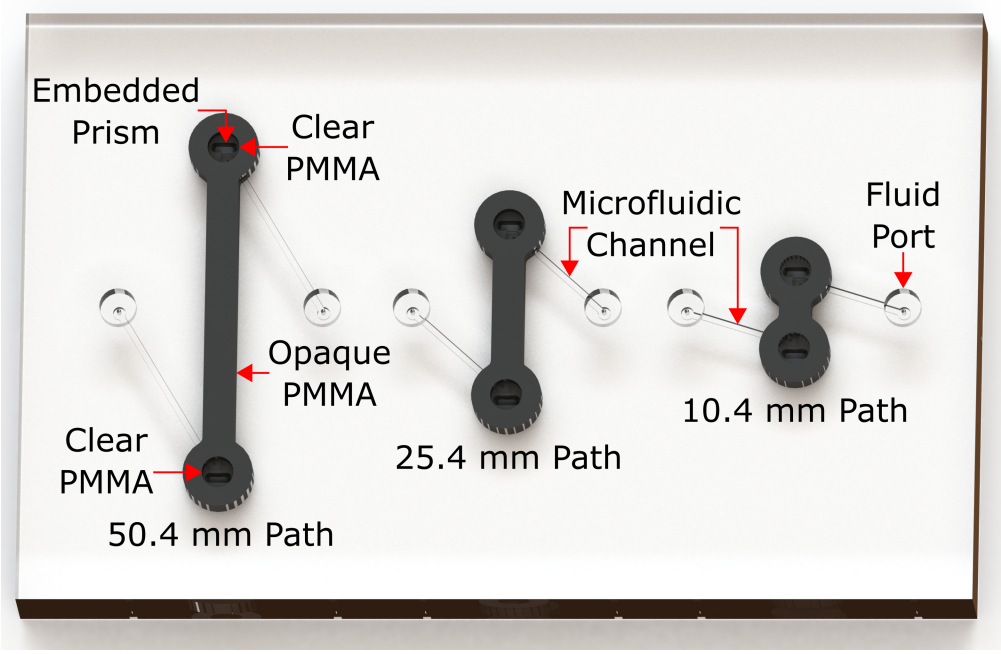

Figure 3.5: Triple inlay chip CAD with labelled features

depolymerization then repolymerization at the interface with heat and pressure. With the 25 μm machined tolerance, the bonding method described in Ogilvie *et al.* [47] was successfully modified. However, we altered the solvent exposure times as our PMMA was extruded instead of cast. Other approaches to solvent/thermal/pressure bonding of PMMA with absolute ethanol [48], isopropyl alcohol (IPA) [49], or combinations could be employed. Prior to bonding, a pre-treatment was required for each surface. Pre-treatment included sanding rough edges with a fine-grit paper and light scrubbing with a scotch pad sponge with water and detergent. A toothbrush was used to scrub inside the cavities. Milli-Q (highly filtered water obtained from the Clean Water Laboratory at Dalhousie University) rinsing followed, and surfaces were dried with blasts of compressed air and IPA. After pretreatment, substrates were ready for bonding. Chloroform (C607-4) was preheated to 30 °C in a sealed container or petri dish. Chloroform-vapor exposure was achieved by suspending each substrate 2 mm above the chloroform liquid line, face down for 45 s. After chloroform exposure,

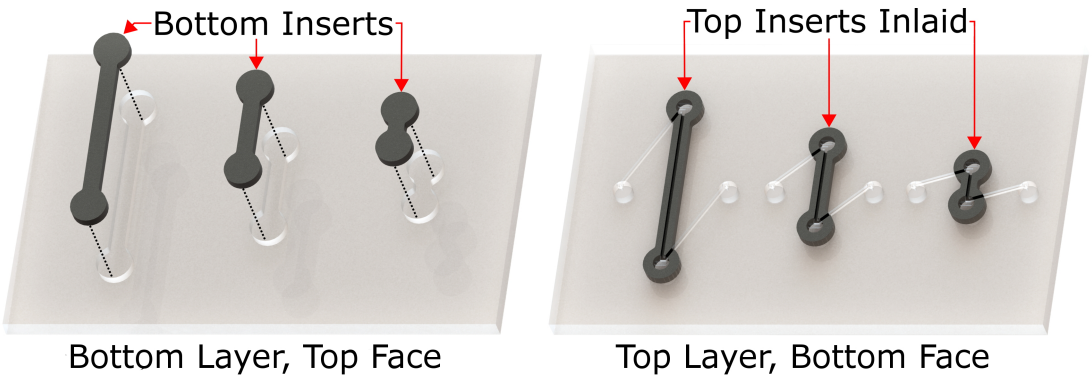

Figure 3.6: Triple inlay chip CAD interior view. An exploded view of the bottom layer is shown (left) where opaque inserts are aligned to cavities in the clear PMMA sheet. The seamless inlaying of the inserts into the sheet is shown (right) on the bottom of the top layer.

the inserts were quickly slotted into the cavities by hand and manually pressed for approximately half a minute. Next, the clear sheet with the inlay ensemble was pressed for 2.5 hours in an LPKF Multipress II set to a pressure of 625 N/cm^2 and a temperature of 115 °C to approach the glass transition temperature of PMMA as described by Becker and Gärtner in 2000 [50]. After pressing, it was common to observe minor protrusion of the opaque inserts from the sheet. The area that would encompass the entire chip design was milled down by a small amount, approximately 0.3 mm, to restore uniformity. It was found that this step was necessary to prevent delamination when bonding the top and bottom layers together.

Next, alignment holes, fluid channels, vias, syringe ports, and prisms were milled into the appropriate spots within the inlaid sheet to realize our microfluidic design. Channels were 400 μm wide and 600 μm deep and were milled into the top layer using a 400 μm mill bit. Each prism was created by cutting into the top layer using a 45-degree end-mill to a depth of 0.8 mm. After bonding the top and bottom layers together, these cuts would create a PMMA-air interface on either end of each optical channel to enable TIR at angles of incidence that exceed θ_c given by equation (3.1).

When milling was complete, two rectangular cuts were made to remove the top and bottom layers from the sheet. Both layers – shown in Figure 3.7 – were left overnight on a hot plate set to 85 °C to release residual stress and/or solvent vapor trapped within the inlay. The top and bottom layers were then bound together using the same bonding and pressing parameters as above with 45 s chloroform-vapor exposure time; however, at 85 °C instead of 115 °C. Corresponding holes in both layers were used for alignment with cylindrical metal dowels of length greater than the thickness of one layer but less than the combined thicknesses of both. Assembly of inlay chip was complete after this point. A photograph if this chip was shown previously in Figure 3.3(a) above: this chip was used to for validation testing to evaluate the performance of the optical cell design.

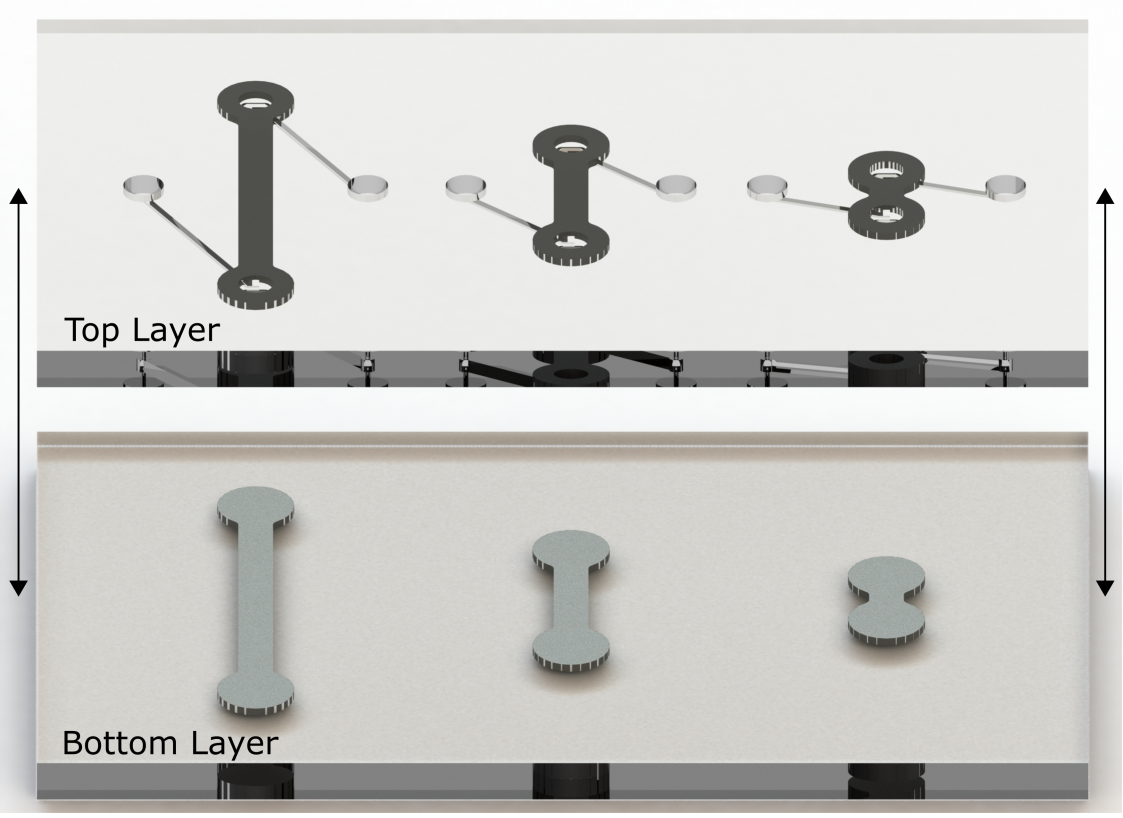

Figure 3.7: Top and bottom layers of the triple inlay microfluidic chip. Black arrows indicate assembly.

3.3.2 Chemistry

A mix of off-the-shelf (OTS) and custom components were used in this project and will be indicated. Likewise, a number of chemicals were used as well: these were all of analytical grade and supplied by Fisher Chemical (Springfield Township, NJ, USA) unless otherwise stated. All Milli-Q was obtained locally from a water purification lab on the Sexton campus at Dalhousie University.

Before any nutrient testing, performance of the absorbance cell was first characterized with two different colours of food dye that had peak absorbances near those of reacted nitrite and phosphate (yellow method). Red food dye standards were prepared by two-fold serial dilutions of a 0.1 % stock, made from dilution of 0.1 mL red food dye (commercial food colouring, Club House Canada) to 100.0 mL with Milli-Q water. Yellow food dye standards were similarly made from diluting a 0.1 % stock, made in the same way (commercial food colouring, Club House Canada). Following dye calibration, nutrients were measured using the inlaid microfluidic chip. For each nutrient chemistry method, standards were stored in darkness near room temperature between use. Likewise, for each chemistry, the reagents were prepared so that reagent molecules were in excess of expected nutrient ions to ensure colour development is proportional to concentration.

Nitrite was measured using the Griess reaction. Nitrite standards were prepared via stepwise dilution of a 1000 μM stock, mixed from 0.069 g of sodium nitrite ($NaNO_2$, CAS-No: 7632–00-0, EMD Millipore, Germany) and Milli-Q to a total volume of 1 L. The Griess reagent was prepared by combining 0.5 g of sulfanilamide, 5 mL of concentrated HCl, and 0.05 g of NEDD (N- (1-Naphthyl)ethylenediamine dihydrochloride), mixed with Milli-Q to a final volume of 500 mL. The completed reagent was stored near 4 °C in a dark environment between use.

Nitrate was measured using the modified Griess reaction. Nitrate standards were prepared from a 7.139 mM nitrate nitrogen solution (NO_3^-, CAT 5457-16 LOT 4002G46). A 1000 μM NO_3^- stock was prepared by mixing 14 mL of this solution with Milli-Q to 100 mL in a volumetric flask. Each standard was made through serial dilution beginning with this stock. The highest concentration standard, 50 μM, was made by diluting the 1000 μM stock solution. The next highest concentration, 25 μM, was prepared from the 50 μM standard. This method of serial dilution was repeated until the final standard, 0.25 μM, for a complete set of eight standards ranging from 0.25 – 50 μM. A single set of standards were made for this project and stored in darkness to minimize degradation from light exposure. A single reagent – a modification on the Griess reagent – was used to simultaneously reduce nitrate to nitrite and develop colour. The modified Griess reagent was made according to Nightingale *et al.* [51] such that 5.0002 g of vanadium (III) chloride (VCl_3, 97 %, CAS 7718-98-1 LOT MKCM2156, Sigma-Aldrich), the reducing agent, was added to a 500 mL volumetric flask and mixed with 100 mL of pure water (Milli-Q). 30 mL of concentrated hydrochloric acid was added slowly, and the resulting mixture was allowed to cool to room temperature following the exothermic reaction between acid and water. Finally, 0.2503 g of NEDD (N-(1-Naphthyl)ethylenediamine dihydrochloride) and 2.5000 g of sulfanilamide were added and mixed to complete dissociation, followed by Milli-Q water to volume (500 mL). The reagent had an inherent deep-blue colour and was diluted in a 1:1 volumetric ratio with Milli-Q to minimize its potency: a final volume of 1 litre. The reagent has a lifetime of at least a month when stored in the dark at 4 °C [3] as was done here.

Phosphate was measured using both the yellow and blue methods. Phosphate standards were prepared similarly from a 1000 μM stock, produced by diluting 0.1361 g of potassium phosphate monobasic (KH_2PO_4, BP362-500 LOT 184 646, Fisher Sci-

entific) to 1 L with Milli-Q. Yellow method phosphate reagent was prepared similar to Legiret *et al.* [39] such that 0.3601 g of ammonium metavanadate and 7.2 g of ammonium molybdate were mixed with 95 mL of concentrated HCl, and brought to a final volume of 1 L with Milli-Q. Constant stirring ensured proper mixing and dissociation of any precipitates formed, and the reagent was allowed to cool to room temperature after the exothermic reaction upon addition of HCl. The completed reagent was stored near 4 °C in a dark environment between use.

The composition of the blue method phosphate reagent was derived from the original method by Murphy and Riley detailed in 1962 [40] and modified by Chris Algar's lab in Dalhousie University's department of Oceanography. Phosphate standards were prepared as described above. The colour-developing reagent used for this method was prepared in three steps. Firstly, in a 100 mL volumetric flask, 100 mL of a "stock antimony potassium tartrate" solution was prepared by dissolving 2.3 g of potassium antimony (III) tartrate hydrate ($\geq$ 99 %, CAS 331753-56-1, BATCH 0000085596, Sigma-Aldrich) in approximately 80 mL of Milli-Q. The flask was then filled to volume with Milli-Q and shaken vigorously to ensure proper mixing of any remaining solids. Secondly, in a 1 L volumetric flask, 1 L of an "ammonium molybdate" solution was prepared by adding 64 mL of concentrated sulfuric acid (H_2SO_4, CAS 7664-93-9, EMD Millipore, Germany) to about 500 mL of Milli-Q. The flask was allowed to cool – accelerated by running cold water over the outside – and 6 g of ammonium molybdate (VI) tetrahydrate (99 %, CAS 12054-85-2, Acros-Organics) was then added and mixed with the fluid to dissolve. 22 mL of the previously described stock antimony potassium tartrate solution was then added, and the flask was finally filled to volume with Milli-Q and shaken to mix. Thirdly and finally, in a 1 L volumetric flask, 1 L of an "ascorbic acid" solution was prepared by dissolving 8 g of L-ascorbic acid ($\geq$99 %, CAS 50-81-7, LOT MKCK8982, Sigma-Aldrich) in about 600 mL of Milli-Q and

then filling to volume with Milli-Q and shaking to mix.

The completed "blue" reagent was then formed by mixing the ammonium molybdate and ascorbic acid solutions in an equal volumetric ratio. Reagent was mixed only when needed: for example, if 200 mL of reagent was needed for a test, 100 mL of each would be mixed together immediately prior to the test. Excess of the two solutions were stored in two separate dark places to prevent photodegradation [4]. The ammonium molybdate solution was stored in darkness at room temperature while the ascorbic acid solution was stored in darkness in the fridge at near 4 °C to help preserve its shelf-life. Both the stock antimony potassium tartrate and the ammonium molybdate solutions were made fresh after 1 month while the ascorbic acid solution was made fresh weekly. When mixed, the reagent remains potent for at least one week when stored in the fridge between use. The phosphate standards measured were prepared in the same manner as the yellow method tests.

3.3.3 Optical Cell Testing Apparatus

An LED centered at $\lambda = 527$ nm (Cree C503B-GANCB0F0791-ND, FWHM = 15 nm) was used to perform absorbance spectroscopy on red food dye, reacted nitrite, and reacted nitrate. An LED centered at $\lambda = 380$ nm (Superbrightleds RL5-UV0315-380, FWHM = 12 nm) was used to perform absorbance spectroscopy on yellow food dye and reacted phosphate samples (yellow method). Phosphate samples measured using the blue method were inspected using a total of four different LEDs: chosen to excite either of the two absorption peaks detailed in Chapter 2 Section 2.3.4. First, an LED centered at $\lambda = 700$ nm (Roithner LaserTechnik LED700-02AU, FWHM = 21 nm) was used to perform absorbance spectroscopy on reacted phosphate samples. These results were then compared to three other similar experiments performed using LEDs

centered at $\lambda = 880$ nm to find the optimal light source. The first LED (Marktech Optoelectronics MTE8800N, FWHM = 60 nm) had the highest power output and the widest beam angle. The second LED (Marktech Optoelectronics MTE8800NK2, FWHM = 60 nm) had the lowest power output and beam angle. The third LED (Marktech Optoelectronics MTE8800NN, FWHM = 60 nm) had a power output and beam angle between those of the other two LEDs. Table 3.1 summarizes each measured species and colour-development method. The wavelengths used for each method are also shown, along with the concentration range of the measured standards. Similarly, Table 3.2 summarizes relevant data sheet specifications for each LED. At

Table 3.1: Species matrix with colour-development methods

Species	**Colour Development**	**LED Wavelength (nm)**	**Conc. Range of Standards Tested**
Red Dye	Inherent	527	0.0016 % – 0.05 %
Nitrite	Griess Reaction	527	0.1 – 100 μM
Nitrate	Mod. Griess Reaction	527	0.25 – 50 μM
Yellow Dye	Inherent	380	0.0063 % – 0.1 %
Phosphate	Yellow Method	380	0.1 – 50 μM
Phosphate	Blue Method	700 and 880	0.25 – 50 μM

the bottom of Table 3.2, the alignment difficulty each LED is stated. This rating is an informal assessment of my experimental findings on the tolerance of each LED to physical offsets. LEDs assigned a rating of "difficult" were most sensitive to minor alignment offsets.

Light detection was enabled using a Digikey TSL257 High-Sensitivity Light-to-Voltage Converter (photodiode). The photodiode was mechanically held face-down at the output clear window with opaque tape – also used to minimize detection of ambient background light. A voltage is produced by the photodiode proportional to the intensity of light measured by the photodiode; thus, these voltages measurements can be used with equation (3.3c) to calculate light absorbance. A custom-built LED

Table 3.2: Light source LEDs data sheet specifications. FWHM refers to the full width at half maximum of the LED. Beam angle refers to the half intensity beam angle.

LED Name	**Center / FWHM (nm)**	**Power Output (mW)**	**Driving Current (mA)**	**Beam Angle (°)**	**Align -ment**
Cree-	527 / 15	N/A	20	15	Easy
RL5-	380 / 12	30	30	15	Difficult
LED700-	700 / 21	5.5	20	16	Difficult
-8800N	880 / 60	6.0	50	12	Difficult
-8800NK2	880 / 60	4.0	50	8	Easy
-8800NN	880 / 60	5.0	50	10	Difficult

driver allowed adjustment of LED intensity while maintaining constant current. The voltage output of the photodiode was connected to a B&K Precision 5491B bench multimeter with 10^{-7} V precision. The sampling rate was set to its maximum, and each measurement along with their date and time was recorded on a personal laptop connected to the multimeter via USB.

LED intensity was adjusted with Milli-Q in the channel to maximize light detection without saturating the photodiode. Since sources and detectors were held externally to the chip, a single set of optical components (LED and photodiode) were used for all three path lengths and the entire testing process. To inspect a sample using one of the three optical cells, the relevant LED was held in place directly above a prism using a metal clamp and a photodiode was held face-down above the prism on the other end. Swapping between each of the three optical cells or changing LEDs between test series was simple due to the decoupled components: a useful advantage of this optical system. A custom opaque enclosure was placed over the entire testing apparatus to minimize background light reception.

In early tests, fluids were injected into the microfluidic chip manually via syringes. In later tests, automation was introduced and fluid injection was performed using

automated syringe pumps. Fluid injection for the red food dye and nitrite tests was performed manually with syringes. Tubing was used to interface between the syringe and the inlet of the microfluidic chip. Immediately before each nitrite measurement, 3 mL of the measured standard was mixed by hand with 3 mL of reagent to produce 6 mL of sample. This was done by pipetting each into a vial, capping the vial, and shaking it. The reacting sample would then be injected into the chip as quickly as possible. The sampling procedure for these tests is shown in Figure 3.8(a). Fluid injection for nitrate, yellow food dye, and phosphate tests was completely automated using an off-the-shelf Cavro XC syringe pump (PN 20 740 556-C, Tecan Systems, San Jose, CA) and a Vici Cheminert C65Z 10-port selector valve (Model No. C65-3710IA, Valco Instruments Co. Inc. Houston TX). Automation produced more consistent and repeatable flow rates. Both dyes, nitrite, and yellow method phosphate samples were analyzed using all three optical channels a total of three times each. Nitrate and blue method phosphate samples were also inspected in triplicate but using only one optical channel for each method. The sampling procedure for nitrate, yellow phosphate and blue phosphate is shown in Figure 3.8(b)-(d).

At the start, end, and between each sample, Milli-Q was pumped through the channel to flush the system and reduce sample–sample crosstalk. A blank measurement was acquired before each sample measurement for each test series. The Milli-Q flush was used as the blank measurement for nitrite and food dye testing. Otherwise, a 1:1 volumetric mix of Milli-Q and reagent was used instead as the blank for nitrate and phosphate testing to correct for the inherent colour of the reagent itself (the nitrite reagent is colourless). Samples and blanks were typically analyzed for a period of five minutes unless otherwise states; the average voltage over the final minute was used to determine absorbance using equation (3.3c). Nitrite, nitrate, and blue phosphate samples were analyzed immediately following reaction with the reagent whereas yellow

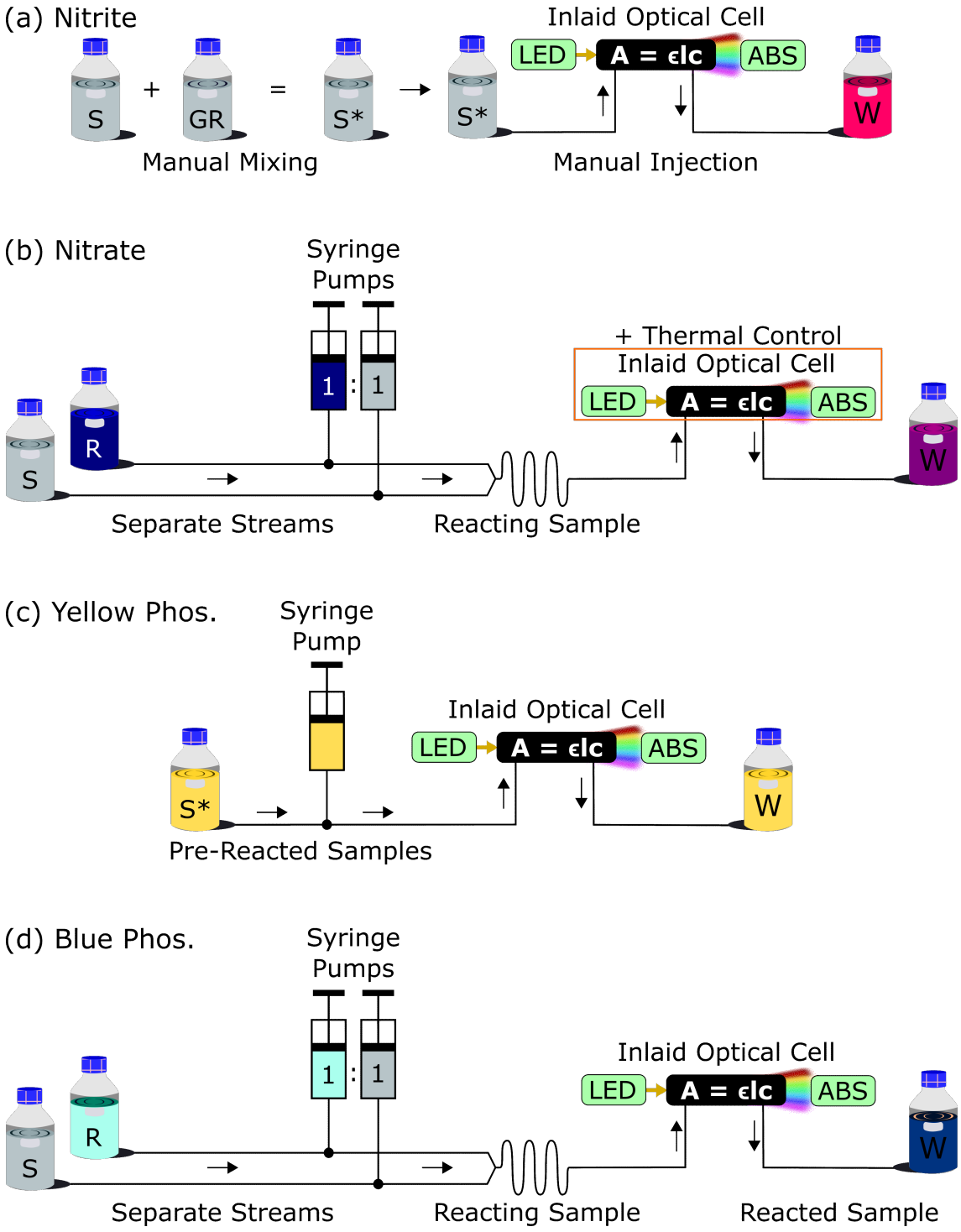

Figure 3.8: Measurement procedure for (a) nitrite, (b) nitrate, (c) pre-mixed yellow phosphate and (d) blue phosphate. S = sample intake, GR = Griess Reagent, S* = mixed sample and reagent, R = reagent, W = waste. In (b)-(d), an OTS selector valve is used to cycle between samples and blanks at the sample intake S – not shown.

phosphate samples were premixed several hours before analysis permitting complete reaction. Finally, at the beginning and end of every test, a measurement of the background light was taken over a minute interval. These values were very small relative to the blank reading and were averaged together for use with equation (3.3c) to account for background light for each light absorbance measurement taken through the test. Background light interference was minimized by placing the measurement chip within a custom opaque enclosure. The amount of background light remained relatively constant, fluctuating less than 1 mV throughout a multi-hour test.

Testing that required elevated reaction temperatures was done using a hot plate. A hot plate was placed under the chip and a digital thermometer was used to monitor chip temperature. The thermometer was fixed in a milled hole in close proximity to the optical channel. Thermal paste was also used to provide better coupling. The temperature of the chip was monitored at a rate of roughly once per second. This was only necessary for a portion of nitrate testing.

3.4 Results and Discussion

3.4.1 Nitrite Detection

The emission spectrum of a Cree C503B-GANCB0F0791-ND LED was first measured using an off-the-shelf spectrometer (Flame, Ocean Optics). Figure 3.9 shows the measured emission spectrum of the LED and reference literature data of the absorption spectrum of nitrite reacted with the Griess reagent. The sensitivity of absorbance measurements depends on the spectral overlapping of the excitation light source and the absorbing fluid. The figure shows good agreement between the emission of the LED and the absorption peak of the reacted nitrite sample. This indicates that the

Cree- LED is a good choice of excitation light source for light absorbance measurement of nitrite samples reacted with the Griess reagent.

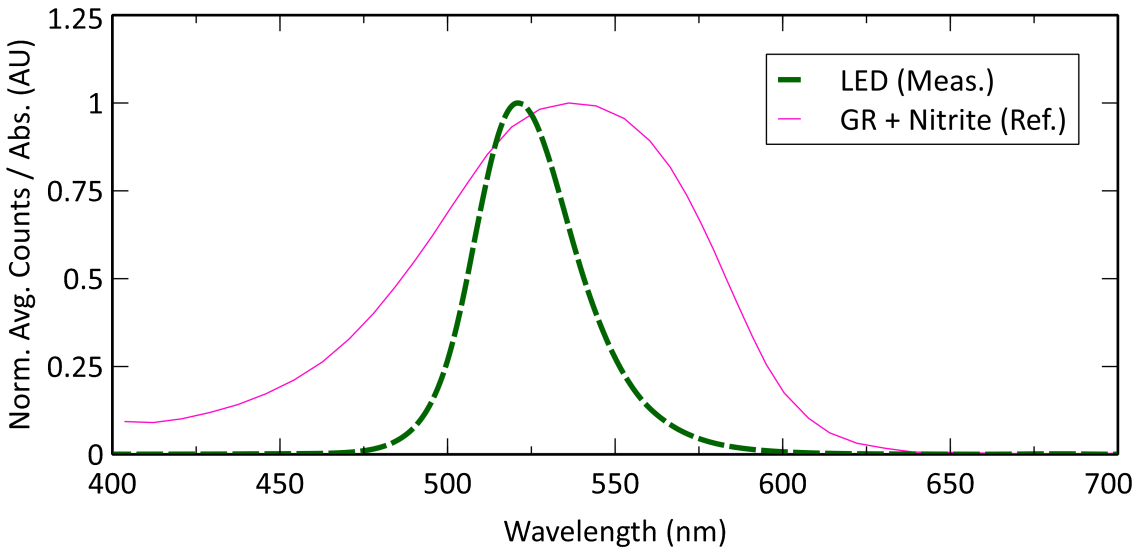

Figure 3.9: (Green) Measured emission spectrum of a C503B-GANCB0F0791-ND LED. (Pink) Reference absorption curve of nitrite reacted with Griess reagent – modified from [52].

The plots in Figure 3.10 depict the raw data produced by light absorbance experiments of red food dye and nitrite through a 10.4 mm inlaid cell. The performance of the inlaid optical cell design was first evaluated with stable food dyes before analyzing nutrient samples. Food dye calibration tests are a standard benchmark towards proving robust, accurate, and reliable light absorbance measurements of an optical cell [53]. There are several external factors that may influence the light absorbance of a reacted nutrient sample with reagent. These include sample degradation, reagent degradation, incorrect sample or reagent make-up, and the kinetics of the reaction between nutrient and reagent. In the case where samples do not produce the expected results, *i.e.* conforming to the Beer-Lambert law given by equation (2.1), it is difficult to determine if the design of the optical cell is at fault or the analyzed samples themselves. Red dye was chosen to mimic reacted nitrite due to its absorbance

spectrum with a strong absorbance peak in the same 540 nm region. Using the Cree-LED, light absorbance measurements were taken through red dye samples ranging from 0.0016 % to 0.05 % (v/v). After successful food dye experiments, nitrite samples were reacted with the Griess reagent and analyzed. Nitrite standards ranged in concentration from 0.1 μM to 100 μM and were measured using the 527 nm LED, after mixing in a 1:1 volumetric ratio with reagent. Therefore, the final concentration of each analyzed sample was half that of the standard. At the start/end of each trial, a measurement was taken to quantify the background light by turning off the LED light source. When shown, this is labelled as "Dark Ref." on the voltage vs. time plot of a trial. The dark measurement was consistently 7 mV $\pm$ 1 mV throughout experiments in this chapter, highlighting the effectiveness of the design in minimizing background light contributions.

Figure 3.10(a) depicts the results of a red food dye experiment performed using 6 dye concentrations with Milli-Q blanks between them. The concentrations of each sample are labelled on each plateau. As expected, the voltage measurement of each blank and sample remains quite constant over the measurement period. During the red food dye tests, the data from each blank and sample measurement was saved in a non-continuous way. For each measurement, data was only recorded after the sample/blank was injected into the absorbance cell until right before it was removed. This is why gaps in the data between measurements can be seen in Figure 3.10(a). In some cases, as with the second measurement of each sample in the triplicate, the data recording process began right before the new sample/blank was injected: this is why the gaps appear in a different place for these measurements. The data logging process was changed for all future tests so that data was continuously logged from test start to finish.

Figure 3.10(b) depicts the results of a nitrite experiment performed using 12 standards

with Milli-Q blanks between them and with concentrations labelled on each plateau. Nitrite samples were analyzed immediately after mixing with the Griess reagent. The reaction kinetics can be observed by the colour-development of each reacting sample; *i.e.* voltage over time. Initially, there was a rapid drop in voltage at the beginning of each reaction followed by a gradual decrease until a plateau was reached. The lower-concentration nitrite samples, less than 5 μM, appear to have completely reacted almost immediately, attaining 95 % of the plateau value within 15 s. The higher-concentration nitrite samples, near 50 μM, took longer to react and required 44 s to attain 95 % of the plateau value. Figures 3.11 (a)-(b) depict the expected linear relationships between sample concentration and absorbance for red food dye and reacted nitrite samples. Light absorbance of each species was characterized using three inlaid microfluidic cells with optical path lengths of 10.4 mm, 25.4 mm, and 50.4 mm, labelled as 10 mm, 25 mm, and 50 mm in the legend, respectively. In practice, shorter optical channels are used to detect highly concentrated samples, but they are less sensitive (smaller slope in Beer-Lambert law). Longer channels are used for detecting small variations and low concentrations but are also more susceptible to noise from bubbles and particulates. Each calibration curve depicted in Figure 3.11 represents the average of three independent experiments, except the 10.4 mm nitrite series where only two trials were performed. Equation (3.3c) was used to calculate the absorbance of each sample from their associated photodiode readings, referenced to the voltage of the prior blank and the voltage produced from background light. Linear trendlines with forced-zero intercepts were fit to each series with strong agreement to

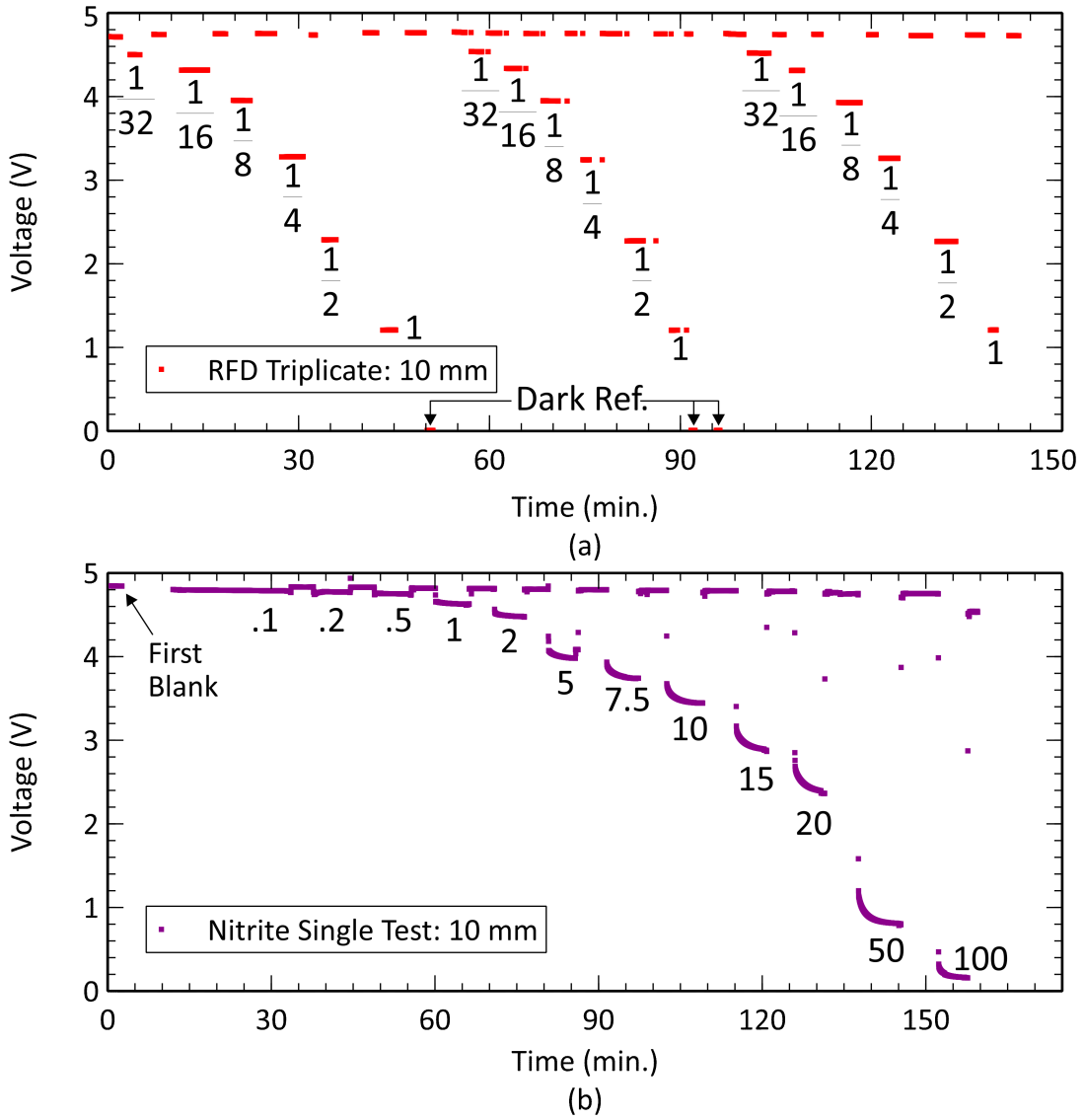

Figure 3.10: Photodiode voltage vs. time for (a) red food dye (triplicate) and (b) reacted nitrite (single test). l = 10 mm.

the data. The equations of each red food dye fit are listed below:

10.4 mm: $A_{\mathrm{RFD}} = 1215[\mathrm{Dye}]; \qquad R^2 = 0.9978, \tag{3.4a}$

25.4 mm: $A_{\mathrm{RFD}} = 2712[\mathrm{Dye}]; \qquad R^2 = 0.9971, \tag{3.4b}$

50.4 mm: $A_{\mathrm{RFD}} = 5449[\mathrm{Dye}]; \qquad R^2 = 0.9952, \tag{3.4c}$

and the equations of each nitrite fit are listed below:

$$\textbf{10.4 mm:} \qquad A_{NO_2^-} = 0.0285[NO_2^-]; \qquad R^2 = 0.9998, \tag{3.5a}$$

$$\textbf{25.4 mm:} \qquad A_{NO_2^-} = 0.0671[NO_2^-]; \qquad R^2 = 0.9996, \tag{3.5b}$$

$$\textbf{50.4 mm:} \qquad A_{NO_2^-} = 0.135[NO_2^-]; \qquad R^2 = 0.9991, \tag{3.5c}$$

where each dye equation has a unitless slope and each nitrite equation has a slope with units $(\mu\text{M})^{-1}$. In Figure 3.11(a), each optical cell (10.4, 25.4, and 50.4 mm) was evaluated with four to six different concentrations depending on the path length. The 10 mm path length was evaluated with six samples and maintained linear results consistent with equation (2.1), even for the most concentrated samples. The 25 mm path length cell showed a linear relationship for the first five samples. The 50 mm path length showed a linear relationship for the first four samples. Figure 3.11(b) depicts the absorbance of various concentrations of reacted nitrite samples. The final concentration of nitrite after mixing with reagent is used to reflect the true concentration in the absorbance cell. All twelve standards were analyzed using the 10 mm cell; whereas, the least-concentrated ten and nine standards were analyzed with the 25 mm and 50 mm cells, respectively. For the concentrations tested, we conclude that our inlaid optical absorbance cells showed excellent linear relationships. Table (3.3) shows experimentally determined attenuation coefficients for red food dye and nitrite for all three path lengths tested. Each attenuation coefficient is determined using equation (2.1) and the applied linear fit for each path length. For example, to determine the attenuation coefficient for nitrite using the 10 mm data, equation (2.1) is used with the fit shown in equation (3.5a):

$$A = \epsilon(10.4)c = (0.0285)c \iff \epsilon = \frac{0.0285}{10.4} = 0.00273(\mu\text{M} \cdot \text{mm})^{-1}.$$

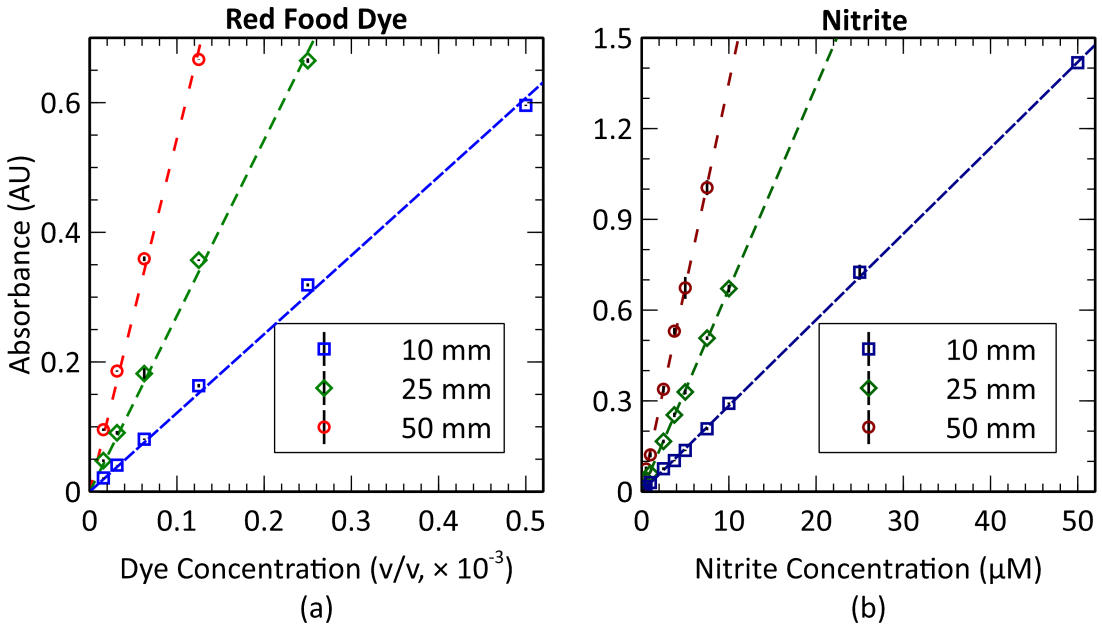

Figure 3.11: Absorbance vs. concentration calibration curves for (a) red food dye and (b) reacted nitrite

Attenuation coefficients are specific to the inspection light wavelength, *i.e.* 527 nm for red food dye and reacted nitrite. An average attenuation coefficient for nitrite was found to be $\epsilon_{NO_2^-} = 0.0269(\mu M \cdot cm)^{-1}$. The value is in agreement with the literature where a range of values between $0.014 - 0.039\ (\mu M \cdot cm)^{-1}$ have been found [13, 14, 54, 55]. These values are specific for nitrite reacted with Griess reagent and inspected with light centered near 525 nm. For all three path lengths, the attenuation coefficients determined for nitrite using this colour-developing technique agree with the literature which further supports the performance of this novel optical cell.

3.4.2 Nitrate Detection

The same Cree C503B-GANCB0F0791-ND LED was used to obtain light absorbance measurements of reacted nitrate samples. As discussed, nitrate samples are reacted using a two-step variation on the Griess reaction. The extra reduction step of the

Table 3.3: Experimentally obtained attenuation coefficients ϵ for red food dye and nitrite for each optical path length. $\bar{\epsilon}$ is the average attenuation coefficient with error (standard deviation). σ_{dye} is volume concentration such that $\sigma_{dye} = v_{dye}/v_{solution}$. Data are shown with precision relative to their error (standard deviation of all repeated trials).

	Red Food Dye		**Nitrite**	
l (mm)	ϵ_{RFD} $(\sigma_{dye} \cdot cm)^{-1}$	$\bar{\epsilon}$	$\epsilon_{NO_2^-}$ $(\mu M \cdot cm)^{-1}$	$\bar{\epsilon}_{NO_2^-}$ $(\mu M \cdot cm)^{-1}$
10.4	1168		0.0273	
25.4	1068	1100 ± 50	0.0264	0.0269 ± 0.0005
50.4	1081		0.027	

modified Griess reaction does not significantly change the absorption spectrum from that shown in Section 3.4.1. Nitrate detection was first investigated through reaction between sample and reagent at room temperature. These reactions were then repeated but at a chip temperature of 41 ± 2 °C to accelerate the rate of colour-development. The consequences of either approach will be explored. Unless otherwise stated, all of the following nitrate tests were done using the 25 mm optical cell of the previously-described triple-inlay chip.

Before analyzing a full set of standards in triplicate, four standards were each analyzed for an extended period of 1.5 hours to determine reaction kinetics. These results are shown in Figure 3.12(a)-(d) for standard concentrations of 5, 10, 20, and 50 μM. Visually, it appears that neither the 20 or 50 μM standards have completed their colour-development at the end of the 1.5 hours. This is determined from their significantly non-zero slopes at this time. For the other two standards, however, it is more difficult to make an accurate assessment of the reaction due to their scale.

As discussed in Chapter 2 Section 2.3.2, the nitrate colour-development process has two steps: reduction and azo dye formation. The reduction step of the reaction can take several hours as reported by [56] unlike the colour-development step (seconds, [51]). For this reason, this process can be approximated as a simple first-order reaction

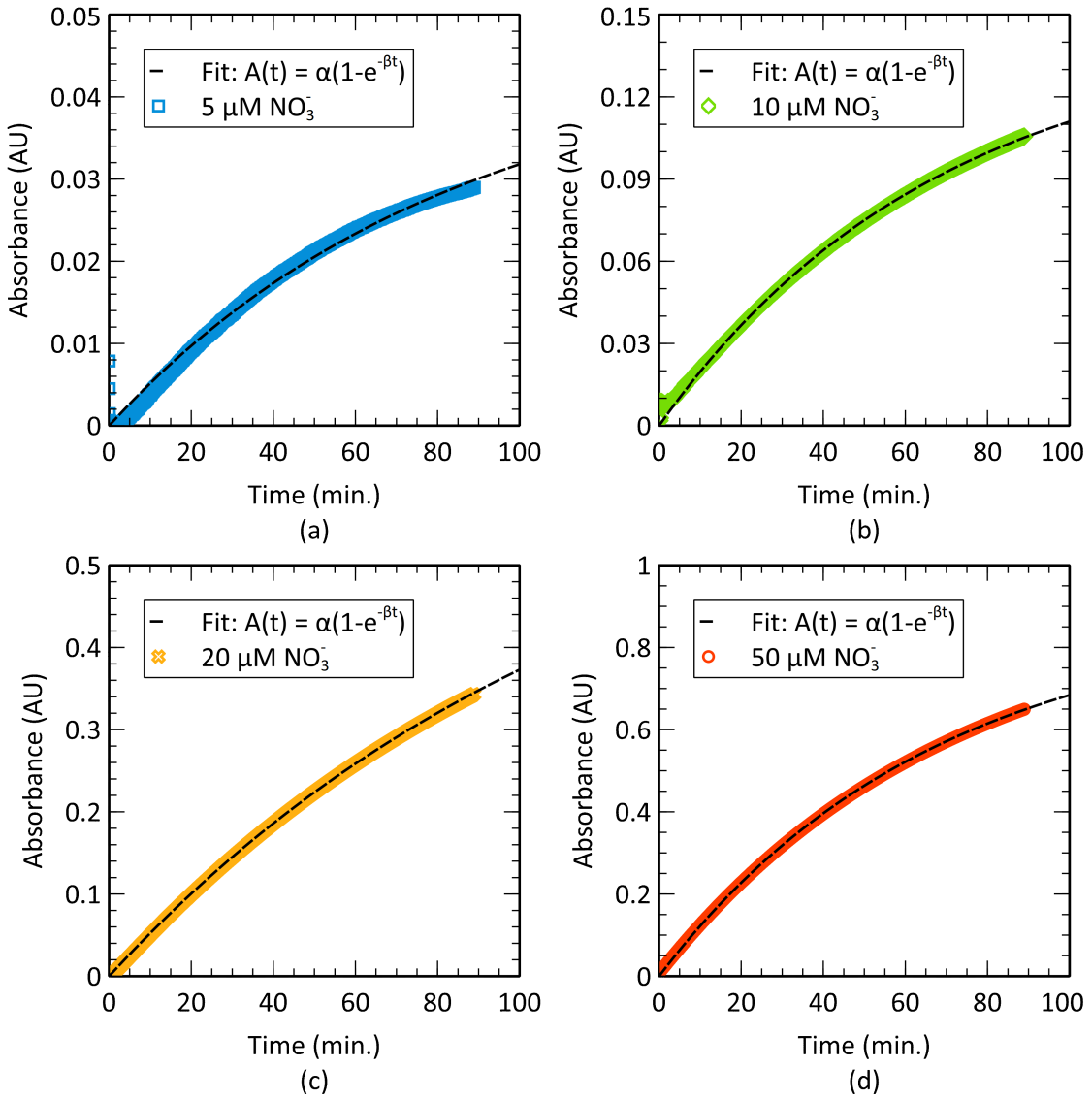

Figure 3.12: Colour development over ∼1.5 hr. for nitrate standard concentrations of (a) 5 μM, (b) 10 μM, (c) 20 μM, and (d) 50 μM upon mixing with modified Griess reagent. Dashed lines indicate an exponential fit applied to each data set as detailed in Table 3.4

.

and modelled using a single-term exponential fit. For each developing sample in Figure 3.12, the absorbance of the sample over time was modelled using the following exponential fit:

$$A(t) = \alpha[1 - e^{-\beta t}], \tag{3.6}$$

where A(t) is absorbance at time t while α and β are fit coefficients and t is the time in seconds. The time constant[‡] of this system is β^{-1} and should remain relatively consistent for any developing nitrate sample.

Initially at time 0, no dye has formed and there is no light absorbance. As time progresses, dye forms and the light absorbance of the sample follows the model in equation (3.6). The dye formation is most rapid at the beginning when the maximum amount of nitrate ions are present and available for conversion. The reagent is prepared in excess so that the nutrient is the only limiting factor on the reaction kinetics. It is expected that the reaction will exhibit asymptotic behavior near completion as all nitrate molecules are converted into dye and the system reaches a steady-state. This is reflected in the model: as time approaches infinity, the light absorbance of the sample plateaus such that:

$$\lim_{t\to\infty} A(t) = \lim_{t\to\infty} \alpha[1 - e^{-\beta t}] = \alpha. \tag{3.7}$$

Equation (3.7) states that the final absorbance value of the completely developed sample is α. Equation (3.6) can be used to predict the time needed to achieve any threshold of reaction completion. For example, 95 % reaction completion is achieved at the time such that $\mathrm{A(t)}/\alpha = 0.95$. The time at which 95 % completion occurs, T_{95}, is determined such that:

$$0.95 = 1 - e^{-\beta T_{95}} \iff -\frac{\ln(0.05)}{\beta} = T_{95}. \tag{3.8}$$

The coefficients α and β for each fit applied to the data in Figure 3.12(a)-(d) are listed in Table 3.4 along with their root mean squared error (RMSE). The times of 50 %, 95

[‡]Time constant: typically used to describe first order processes – the time at which the system achieves $\sim$ 63 % of its steady-state value

%, and 99 % reaction completion are listed, evaluated in the same manner as shown above. Finally, the time constant $(\beta)^{-1}$ is calculated for each standard concentration and compared.

Table 3.4: Fit parameters for Figure 3.12. A(t) is absorbance at time t (in seconds) while α and β are fit coefficients. T_i is the time in hours to achieve i % reaction completion. The calculated time constant $(\beta)^{-1}$ for each concentration is shown along with their average $(\beta)^{-1}_{avg}$.

Fit Model: A(t) = α[1-$e^{-\beta t}$]

Conc. (μ**M**)	α **(AU)**	β **(s^{-1})**	**RMSE (AU)**	T_{50} **(hr)**	T_{95} **(hr)**	T_{99} **(hr)**	$(\beta)^{-1}$ **(hr)**	$(\beta)^{-1}_{avg}$ **(hr)**
5	0.04551	0.000200	0.00068	0.963	4.161	6.397	1.390	1.4 ± 0.4
10	0.1444	0.000244	0.001122	0.790	3.413	5.246	1.139	
20	0.6718	0.000135	0.001023	1.431	6.186	9.509	2.065	
50	0.8835	0.000248	0.001991	0.777	3.361	5.167	1.122	

As shown in Table 3.4, each model predicts a period between 5 – 9 hours to achieve up to 99 % reaction completion. The accuracy of each fit however is confined to the available data: 1.5 hours worth of data – each single trials, not triplicates – to predict the entire reaction to completion. The reaction kinetics should remain relatively consistent and not depend on standard concentration. This can be seen from the average time constant calculated from each concentration: $(\beta)^{-1}_{avg}$ = 1.4 ± 0.4 hr. Three of the four trials had very similar time constants (1.1 – 1.3 hr) while the 20 μM was slightly inconsistent. Omitting the 20 μM trial, the average time constant to describe this system is: $(\beta)^{-1}_{avg}$ = (1.22 ± 0.15) hr.

Assuming that the 20 μM trial may be an outlier, the applied model predicts a period of approximately 3 – 4 hours for 95 % completion and 5 – 6 hours for 99 % reaction completion. With this in mind, a single nitrate standard, 50 μM, was analyzed over a period of nearly 9 hours: these results are shown in Figure 3.13. Before analyzing the sample, a blank was injected into the cell: used to calibrate the optics. The LED intensity was set such that the photodiode measured near saturation through blank:

4.1435 ± 0.0005 V. Calibrating the optics to near saturation through a blank ensured the largest measurement range possible.

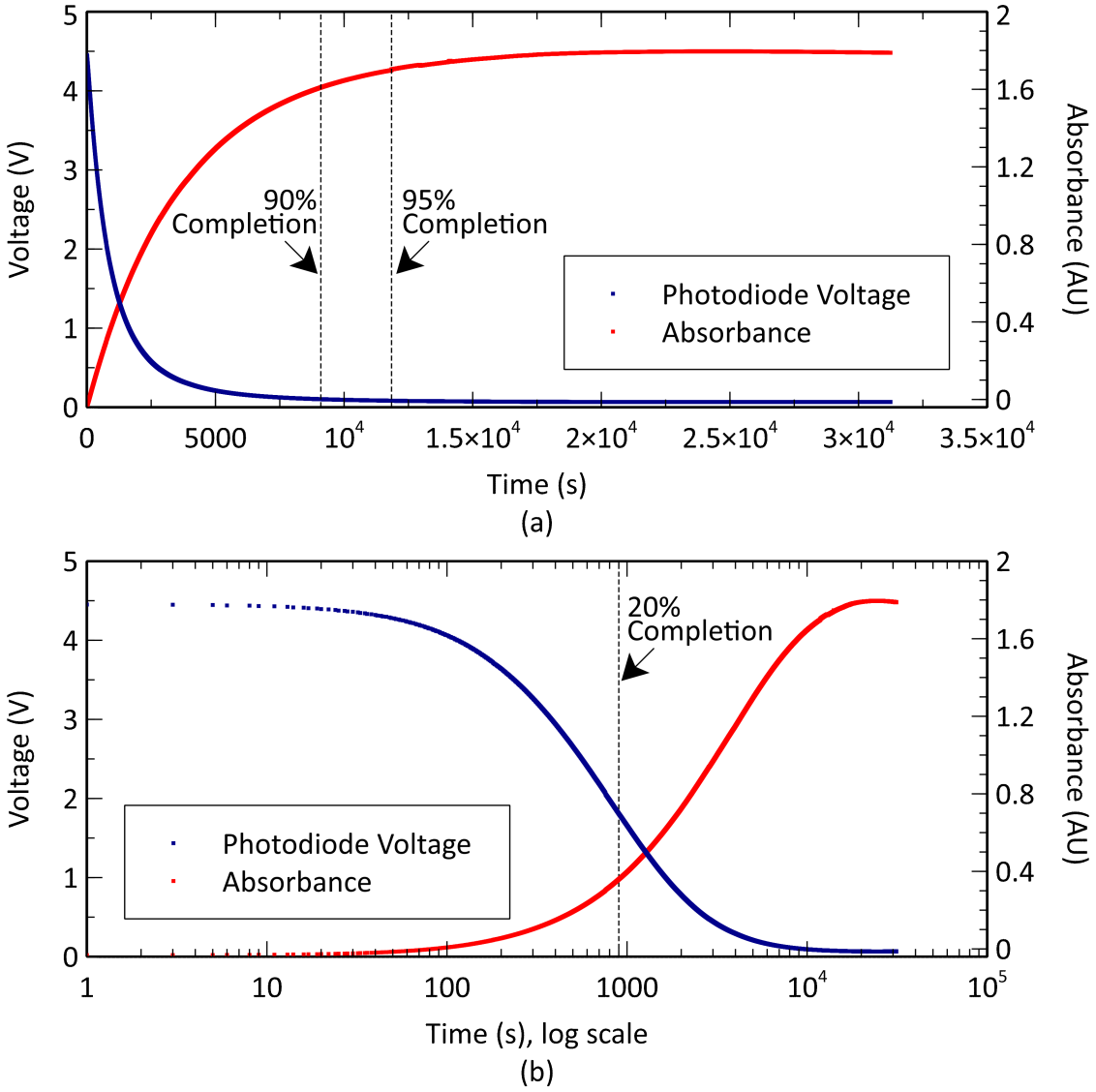

Figure 3.13: Colour development of a 50 μM NO_3^- standard reacting with reagent at RT. The bottom plot has a log scale applied to the time axis to better depict early behavior in the data.

In the first plot of Figure 3.13, photodiode voltage is plotted versus time: this voltage is proportional to the amount of light that passes through the sample. Initially, the photodiode voltage was nearly identical to the blank reading, indicating no colour

development. As colour-development began, the voltage produced by the photodiode dropped as less light transmitted. Observed in the second plot of Figure 3.13 is the same data but with a log scale applied to the time axis: this plot suggests that colour-development began after $\sim$ 30 seconds. When testing nitrite conversion on its own prior to this project, colour-development was observed to begin nearly immediately upon reaction with reagent: this is also confirmed by the literature [14]. Thus, this delay is attributed to the extra step of nitrate to nitrite reduction wherein a period of near 30 seconds is needed for the first nitrate molecules to reduce to nitrite.

Equation (3.3c) was used to convert each voltage measurement to absorbance in reference to the previously-measured blank and a background light measurement recorded at the end of the trial. Towards the end of the trial, the near-zero slope suggests completed colour development. The final voltage/absorbance reading was used to determine the times at which the reaction was 20, 90, and 95 % complete: these are indicated on the plots by dashed lines. The reaction took 3.3 hours to achieve 95 % completion: this confirms the slow reaction kinetics at RT as cited in the literature and is consistent with the model prediction discussed above.

A full set of nitrate standards between 0.25 – 50 μM $\mathbf{NO_3}^-$ was then analyzed as depicted in Figure 3.14 below. Each standard (labelled) was analyzed three times, from highest to lowest concentration, with blanks measured prior. The time to measure each blank or sample was 15 minutes including pumping time. In practice, however, blanks are typically measured for 5 minutes or less: this would equate to a complete sample measurement every 20 minutes or three samples an hour.

In the first plot of Figure 3.14, the voltage produced by the photodiode is plotted against time. As expected, the produced voltage was relatively constant while analyzing blanks (horizontal lines) and otherwise dropped with time during sample

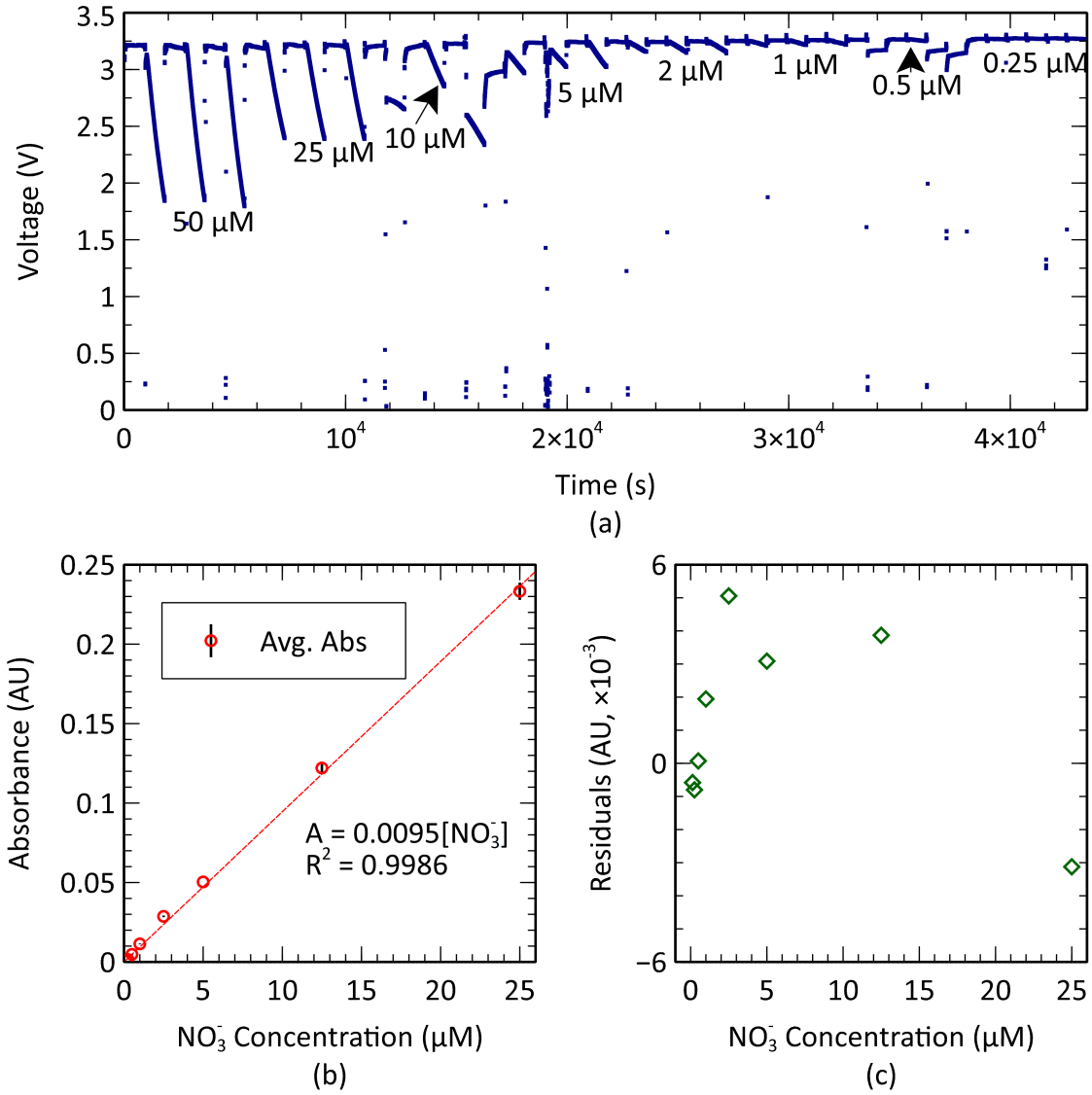

Figure 3.14: Reacting nitrate standards (labelled, a) at RT analyzed in triplicate. (a) Photodiode voltage vs. time. (b) Average absorbance of each sample nitrate concentration with error. (c) Residuals of each sample relative to the applied linear fit. The non-random distribution is indicative of bias.

colour-development. The most concentrated samples produced the most significant voltage drops, and repetitions of the same sample produced consistent voltage behavior except for when bubbles entered the cell (most prominent around the 10 μM standards).

In the second plot of Figure 3.14, photodiode voltages were converted into absorbances using equation (3.3c). The voltage reading of each sample or blank was determined as the average of their final minute of voltage readings. Each sample was analyzed three times in total: the average absorbance reading of that sample was then plotted against the concentration of that sample (half that of the standard due to 1:1 mixing with reagent). In cases where bubbles tampered with readings, *i.e.* two of the 10 μM and 0.5 μM measurements, the outlier values were not included in the average. These bubbles were introduced by the selector valve, as the seal of certain ports had degraded over time with use.

Testing using elevated reaction temperatures was then carried out in order to improve on reaction sensitivity. A preliminary test to de-risk light absorbance testing with heat was performed in which Milli-Q water was injected into the cell at RT and analyzed. After a period of time, the hot plate under the chip was turned on and the chip gradually increased in temperature. It was found that a chip temperature near 50 °C caused dissolved gases within the sample to expand. This produced undesirable light scattering and ruined light transmission through the optical cell. This was confirmed by pumping more sample into the chip and observing segmented fluid in the outlet tube. Since temperatures between 30 – 40 °C are ideal for rapid nitrate reduction [3], a temperature of 41 °C was used (55 °C on the hotplate). This temperature would fluctuate by 1-2 degrees during a trial.

Before analyzing a full set of standards in triplicate, four standards were analyzed – each over a period of 15 minutes – to once again determine reaction kinetics but at this elevated reaction temperature of 41 °C. These results are shown in Figure 3.15(a)-(d) for standard concentrations of 2, 5, 25, and 50 μM. Once again, a single-term exponential fit was applied to each set of data.

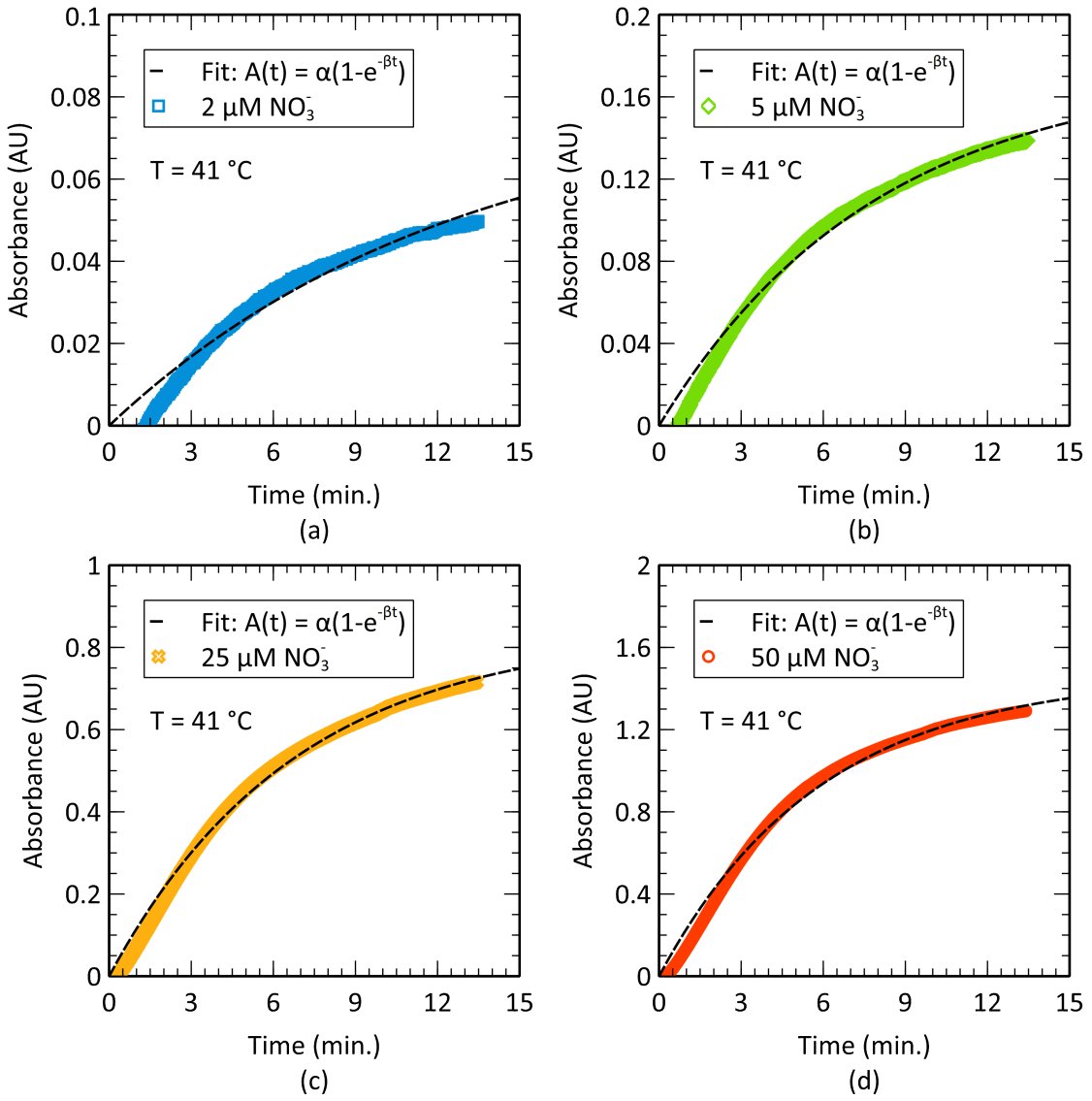

Figure 3.15: Colour development over ∼15 min. for nitrate standard concentrations of (a) 2 μM, (b) 5 μM, (c) 25 μM, and (d) 50 μM upon mixing with modified Griess reagent. Dashed lines indicate an exponential fit applied to each data set as detailed in Table 3.5

.

The coefficients α and β for each fit applied to the data in Figure 3.15(a)-(d) are listed in Table 3.5 along with their root mean squared error (RMSE). The times of 50 %, 95 %, and 99 % reaction completion are listed, evaluated in the same manner as shown previously. Finally, the time constant $(\beta)^{-1}$ is calculated for each standard

concentration and compared. The average time constant measured was $(\beta)^{-1}_{avg} = 8 \pm 3$ min. Recall that the average time constant for the room temperature tests was 1.4 $\pm$ 0.4 hr. (84 $\pm$ 24 min.). The time constant at this elevated reaction temperature is thus approximately 10.5 times smaller than reaction at room temperature.

Table 3.5: Fit parameters for Figure 3.15. A(t) is absorbance at time t (in seconds) while α and β are fit coefficients. T_i is the time in minutes to achieve i % reaction completion. The calculated time constant $(\beta)^{-1}$ for each concentration is shown along with their average $(\beta)^{-1}_{avg}$.

Fit Model: A(t) = α[1-$e^{-\beta t}$]

Conc. (μ**M**)	α **(AU)**	β **(s^{-1})**	**RMSE (AU)**	T_{50} **(min)**	T_{95} **(min)**	T_{99} **(min)**	$(\beta)^{-1}$ **(min)**	$(\beta)^{-1}_{avg}$ **(min)**
2	0.0801	0.00131	0.00547	8.85	38.26	58.81	12.77	
5	0.1737	0.00211	0.00594	5.47	23.65	36.35	7.90	8 $\pm$ 3
25	0.8404	0.00246	0.01789	4.69	20.28	31.17	6.77	
50	1.468	0.00283	0.03841	4.09	17.66	27.14	5.89	

Now that the time constant had been determined to be less than 15 minutes, a full calibration test was performed. Each sample was reacted for a period of 15 minutes. Figure 3.16 shows the results of a nitrate test at 41 °C, processed in the same ways as the RT test. In the RT test, the residuals were low in magnitude, $|R|_{max} \approx$ 0.005 AU, and good linearity was observed over the full concentration range: thus, the upper bound of linear behavior appears to exceed the 25 μM reacted sample. In the heated test, however, the absorbance of the final concentration was visibly non-linear compared to the other concentrations (Figure 3.16(b)). Omission of this concentration from the calculation of the fit improved the residuals considerably, i.e. $|R|_{max} \approx$ 0.092 AU to $|R|_{max} \approx$ 0.025 AU. At high absorbances (A > 1), mismatch between the emission spectrum of the light source and the absorbance spectrum of the fluid, combined with the slightly polychromatic nature of the light source, becomes more significant [14] and can produce results consistent with those observed here (tapering-off at high absorbance). Since the point at which non-linear behavior begins

is unclear, i.e. somewhere between 12.5 and 25 μM, 12.5 μM will be taken as the upper bound. As a result of the above, the linear detection region appears to be between 50 nM to at least 25 μM at RT or between 11 nM to at least 12.5 μM at 41 °C. Either approach is therefore suitable for use in the Bedford Basin where nitrate ranges from 0.1 – 7 μM.

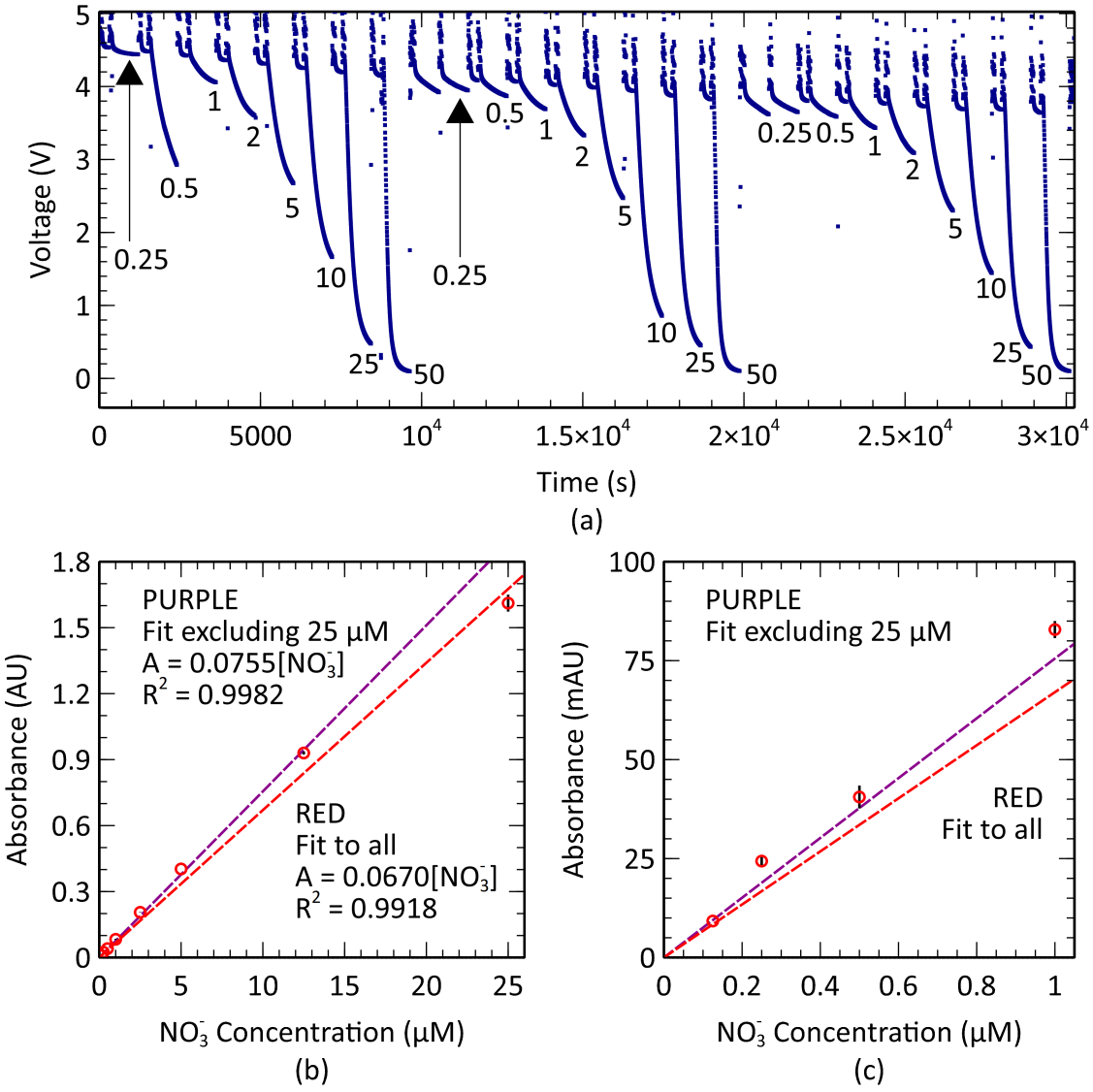

Figure 3.16: Reacting nitrate standards heated to 41 ± 2 °C and analyzed in triplicate. (a) Photodiode voltage vs. time with labelled standard concentrations. (b),(c) Average absorbance with error of each sample plotted against concentration. Two linear fits are shown: one that includes the final concentration and one that does not.

Furthermore, observed in Figure 3.17 is minor crosstalk between successive blank measurements at the beginning of the RT triplicate trial. The blank reading before the first 50 μM standard was relatively constant (blue) whereas the successive blank measurements measured lower and exhibited decay with time (green-red). This suggests incomplete flushing of old-sample from the measurement channel between blank measurements and indicates crosstalk. Blanks measured after less-concentrated samples also exhibited minor crosstalk, but to a lesser degree as expected. Similarly, the crosstalk observed in the heated test was more significant than that observed here: a result of more intense colour-development. This is likely a contributing factor to the higher-magnitude residuals observed in the heated test and may also explain the systematic bias whereby the highest-concentrations are always below their fit due to more severe blank interference. The crosstalk observed highlights the importance of blank measurements and can be reduced by more flushing.

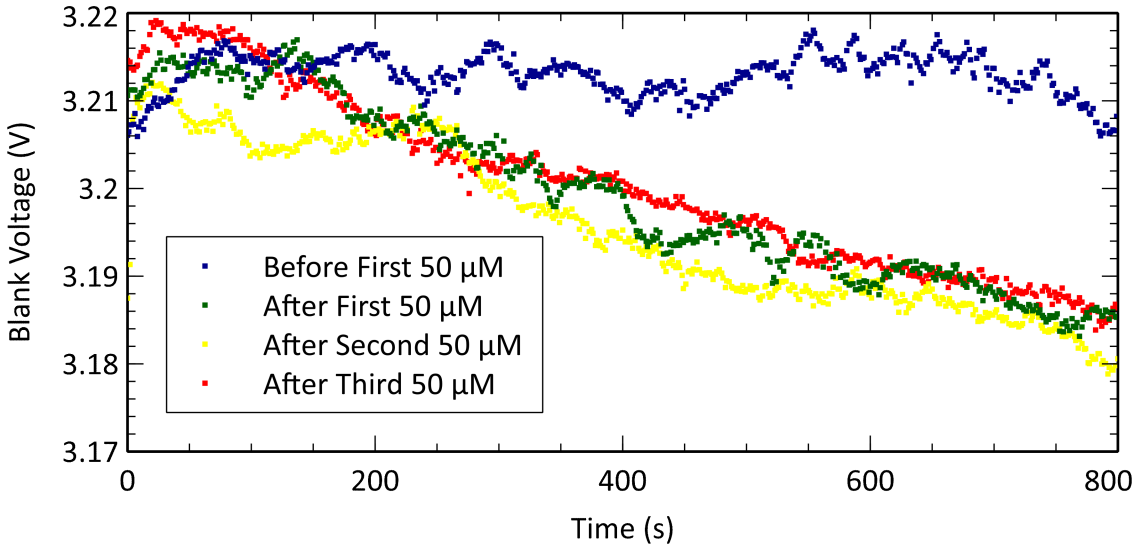

Figure 3.17: Drift analysis: crosstalk between successive blanks

3.4.3 Phosphate Detection – Yellow Method

The emission spectrum of a RL5-UV0315-380 LED was first measured using an off-the-shelf spectrometer (Flame, Ocean Optics). Similarly, the absorption spectrum of a 50 μM phosphate standard reacted using the yellow method was measured using the same spectrometer and a high-power white LED light source. Figure 3.18 shows both measured spectra, indicating good agreement between the emission of the LED and the absorption peak of the reacted phosphate sample.

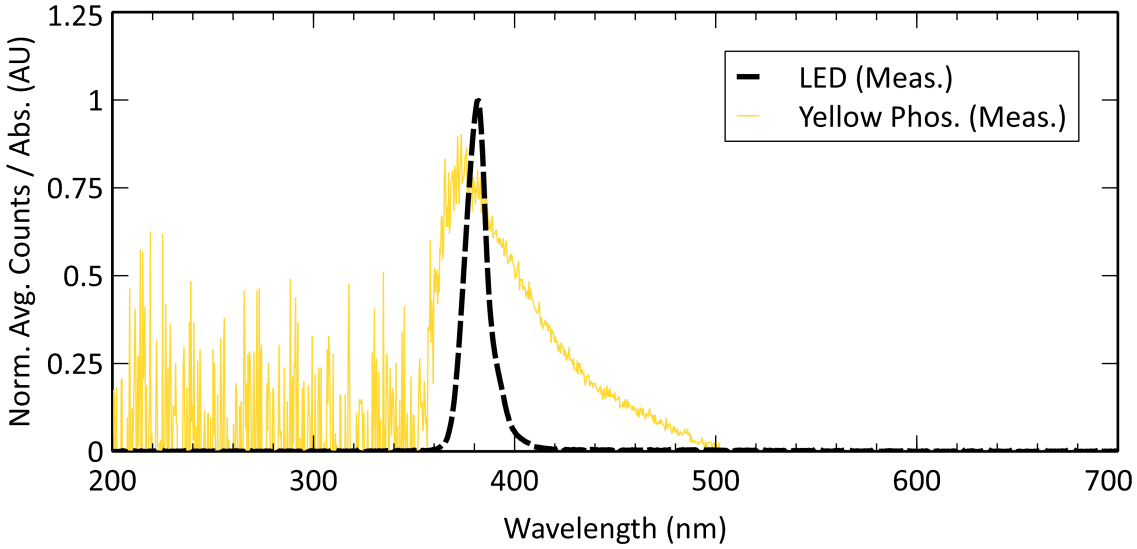

Figure 3.18: (Black) Measured emission spectrum of a RL5-UV0315-380 LED. (Yellow) Measured absorption curve of phosphate reacted using the yellow method.

As with red food dye and nitrite, yellow food dye was chosen to mimic the absorbance spectra of phosphate reacted using the yellow method. Optical measurements were performed using the RL5- 380 nm LED as the excitation light source. A range of yellow dye was tested between 0.0063 % – 0.1 % (v/v). Figure 3.19(a) shows 5 concentrations of yellow food dye analyzed a total of three times through a 10.4 mm long inlaid optical cell; each series produced consistent results. Milli-Q blanks preceded each sample as described in Section 3.3. Near the 67-minute mark, a temporary drop

in voltage can be observed: this was likely the result of an air bubble in the measurement channel during stopped flow. Additional sample was injected into the cell to displace the bubble, which restored the expected voltage reading as seen before and after this drop. Finally, at the end of testing, a measurement was taken to quantify the background light by turning off the LED light source.

Figure 3.19(b) shows the results of a phosphate experiment performed with 8 standards ranging in concentration from 0.1 – 50 μM. Here, the blank was a 1:1 volumetric mix of Milli-Q and phosphate reagent – chosen due to the inherent colour of the reagent itself – which was injected between standards. The sequence of injection was blank, sample and then pure Milli-Q water. The Milli-Q water flush was used as a precaution to minimize crosstalk between standards. The Milli-Q flush can be observed in Figure 3.19(b) as sudden voltage spikes which saturate the photodiode since the pure Milli-Q is colourless compared to the blank (LED intensity is set based on blank). Also highlighted in the figure is an instance where air bubbles momentarily entered the measurement channel: this was remedied with further pumping but produced a minor offset to further voltage data (corrected-for in each absorbance measurement by the blank). For the phosphate experiments, samples were fully reacted prior to injection into the optical cell. As stated in Chapter 2 Section 2.3.3, the yellow method has a reaction time of 1 – 5 min. I chose to pre-react the phosphate samples to benchmark stable nutrient samples; hence, the relatively constant voltage plateaus. In Figure 3.19(b), there is a minor drift of the blank voltage, decreasing 100 mV over the 100 min duration of the experiment, which was less than a 2 % drop over 1.5 hours. It is interesting to note that the yellow dye experiment in Figure 3.19(a) also drifted down, 70 mV over 6000 s, but this is less visible because of the y-axis scale. The drift was repeatably observed for the phosphate and yellow dye measurements, indicating it is not the phosphate chemistry. The gradual voltage decrease

between blanks is most likely due to UV-fluid interaction or ageing of the PMMA plastic through prolonged intense UV-exposure. This is a strong justification for choosing an alternative method of phosphate quantification. Figures 3.20(a-b) plot

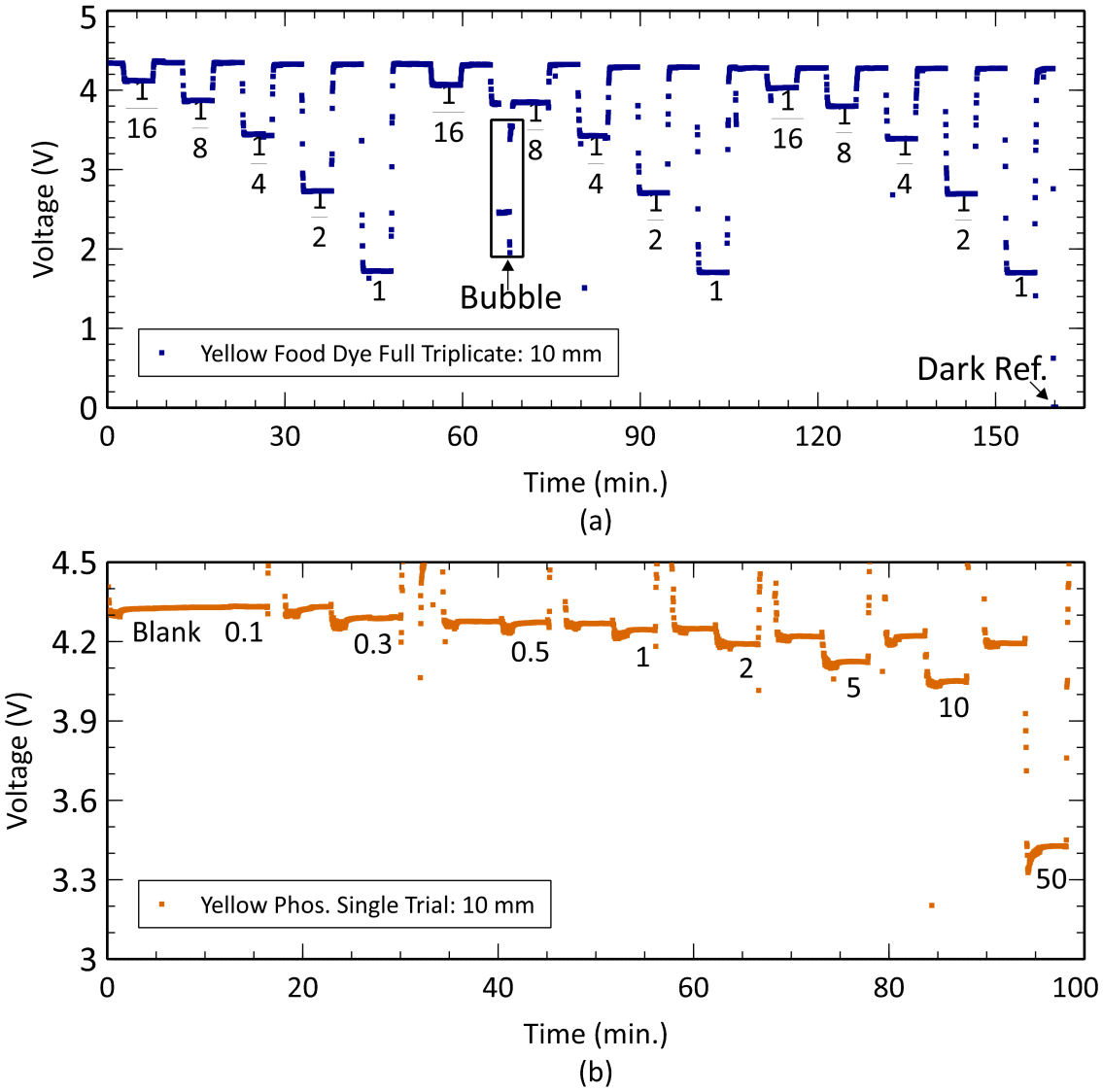

Figure 3.19: Photodiode voltage vs. time (l = 10 mm) for (a) a yellow food dye triplicate test and (b) for a yellow phosphate single test.

absorbance versus concentration for yellow food dye and reacted phosphate samples. Figure 3.20(a) depicts five yellow food dye samples analyzed with the 10 mm and 25 mm optical path lengths, and four samples analyzed on the 50 mm optical path

length. All three data sets showed excellent linear fits for their entire concentration range. Similarly, in Figure 3.20(b), the absorbance for all eight phosphate standards show the expected linear relationships.

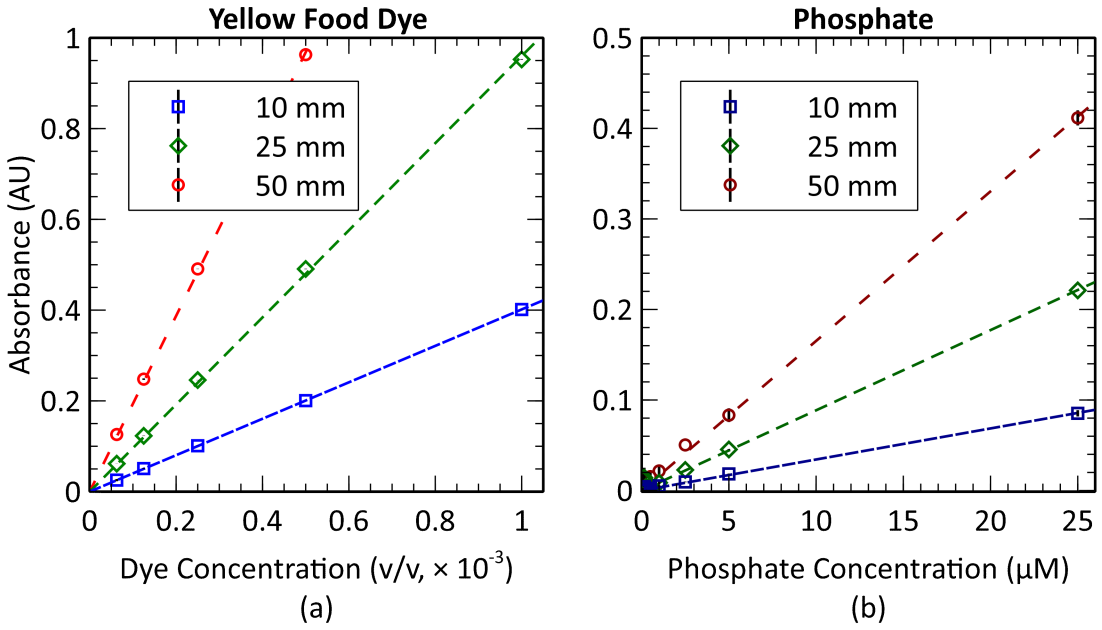

Figure 3.20: Absorbance vs. concentration calibration curves for (a) yellow food dye and (b) reacted phosphate

The equation of each fit applied to the data in Figure 3.20(a) is listed below along with their R^2 values:

10.4 mm: $A_{\mathrm{YFD}} = 401.5[\mathrm{Dye}]; \quad R^2 = 1.0000, \quad (3.9a)$

25.4 mm: $A_{\mathrm{YFD}} = 959.8[\mathrm{Dye}]; \quad R^2 = 0.9996, \quad (3.9b)$

50.4 mm: $A_{\mathrm{YFD}} = 1936.6[\mathrm{Dye}]; \quad R^2 = 0.9997, \quad (3.9c)$

and with those applied to Figure 3.20(b):

$$\textbf{10.4 mm:} \qquad A_{\mathrm{PO_4}^{3-}} = 0.00343[\mathrm{PO_4}^{3-}]; \qquad R^2 = 0.9962, \tag{3.10a}$$

$$\textbf{25.4 mm:} \qquad A_{\mathrm{PO_4}^{3-}} = 0.00886[\mathrm{PO_4}^{3-}]; \qquad R^2 = 0.9913, \tag{3.10b}$$

$$\textbf{50.4 mm:} \qquad A_{\mathrm{PO_4}^{3-}} = 0.01652[\mathrm{PO_4}^{3-}]; \qquad R^2 = 0.9983. \tag{3.10c}$$

These fits were used to find each attenuation coefficient as explained in Section 3.4.1. Table 3.6 shows experimentally determined attenuation coefficients for yellow food dye and phosphate for all three path lengths tested. These quantities are specific to the inspection light wavelengths, *i.e.* 380 nm for yellow food dye and reacted phosphate (yellow method). An average attenuation coefficient for phosphate was found to be $\epsilon_{PO_4^{3-}} = 0.00335(\mu M \cdot cm)^{-1}$. This value is also in agreement with literature values that range between 0.0036 – 0.00503 $(\mu M \cdot cm)^{-1}$ [38, 39, 57] for the yellow method using light centered near 380 nm. For all three path lengths, the attenuation coefficients determined for phosphate using this colour-developing technique agree with the literature which further supports the performance of this novel optical cell.

Table 3.6: Experimentally obtained attenuation coefficients ϵ for yellow food dye and phosphate (yellow method) for each optical path length. $\bar{\epsilon}$ is the average with standard deviation. σ_{dye} is volume concentration such that $\sigma_{dye} = v_{dye}/v_{solution}$. Data are shown with precision relative to their error (standard deviation of all repeated trials).

	Yellow Food Dye		**Phosphate**	
l (mm)	$\epsilon_{YFD}\ (\sigma_{dye} \cdot cm)^{-1}$	$\bar{\epsilon}$	$\epsilon_{\mathrm{PO_4}^{3-}}\ (\mu M \cdot cm)^{-1}$	$\bar{\epsilon}_{\mathrm{PO_4}^{3-}}\ (\mu M \cdot cm)^{-1}$
10.4	386.1		0.00330	
25.4	377.9	383 ± 4	0.00349	0.00335 ± 0.00012
50.4	384.24		0.00328	

3.4.4 Phosphate Detection – Blue Method

Phosphate standards were once again measured but using the blue method of colour development. This second approach was investigated to produce phosphate measurements using a less toxic reagent than that of the yellow method while also seeking greater measurement sensitivity. Similarly, the optics associated with this approach were easier to align than their UV counterpart needed for the yellow method. A total of four excitation light sources were used as described in Section 3.3.3. The emission spectrum of each LED and the absorption spectra of a 25 μM phosphate standard reacted using the blue method was measured in the same way as in previous sections and shown in Figure 3.21. The measured absorbance spectrum confirms the discussion in Chapter 2 Section 2.3.4, *i.e.* the presence of two absorption peaks near 700 and 880 nm. As seen in the figure, the Marktech MTE8800NK2 and MTE8800NN LEDs had nearly identical spectra. The figure confirms that each of the four LEDs are good candidates for testing as each emission spectra is located near an absorbance peak.

First, the 700 nm LED light source was used using the 25.4 mm long inlaid optical cell. Figure 3.22 shows the results of a blue phosphate experiment performed with 8 standards ranging in concentration from 0.1 – 50 μM. The standard concentrations were 0.25, 0.5, 1, 2, 5, 10, 25, and 50 μM. Each standard was measured 5 times in a row with blanks. As in Section 3.4.3, the blank was a 1:1 volumetric mix of Milli-Q and phosphate reagent, which was injected between standards. Other groups have used 5 minutes as their measurement time to observe full colour-development [41] as was done here. It was found that five minutes of measurement time was more than enough to capture the entire reaction to completion. As an example, reaction with a 50 μM standard took 70 seconds to achieve 95 % of its full colour-development, 105

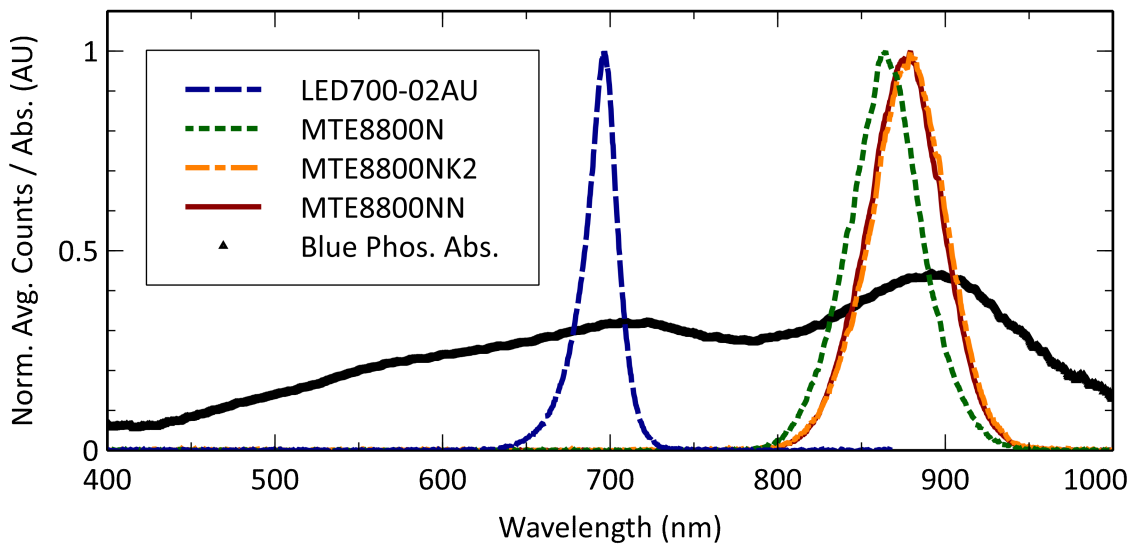

Figure 3.21: Measured emission spectrum of a LED700-02AU (blue dashes), MTE8800N (green dots), MTE8800NK2 (orange dash-dot), and a MTE8800NN (red line) LED. Also shown is the measured absorption curve of a 25 μM phosphate standard reacted using the blue method (black triangles).

seconds to achieve 99 %, and 137 seconds to achieve 99.9 %.

Unlike with the yellow phosphate tests, there was no pure Milli-Q water flush with these tests. The sequence of injection was blank (MQ + reagent), sample (standard + reagent), blank, and sample cycled until each measurement of each standard was done. Figure 3.22(a) shows the photodiode voltage throughout the course of the experiment. Colour-development is observed in areas where there is a steep slope to the data *i.e.* between the plateaus of a blank and a sample. Plateaus indicate minimal/no change in colour and are observed during blanks and after the first ~ 2 minutes of each sample. Throughout the course of the experiment, the blank drifts downward in voltage but in relation to the measured concentration. For example, the blanks associated with the first standard remain relatively constant, but there is a drop between them and the blanks of the second standard. The blanks of the second standard are self-consistent as well, and this pattern continues for all blanks.

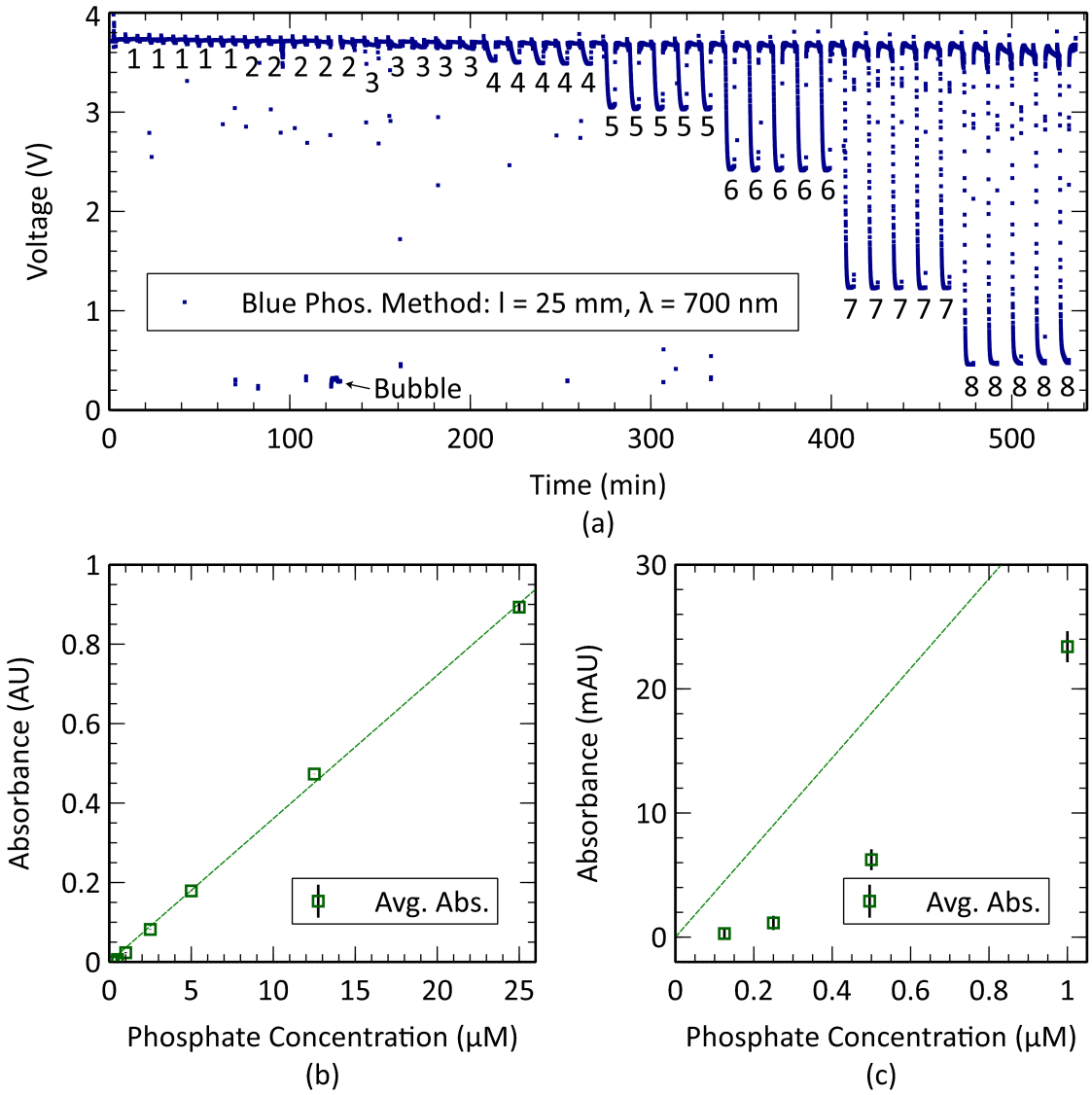

Figure 3.22: Blue phosphate test: $\lambda = 700$ nm, $l = 25$ mm, 8 concentrations (n = 5). (a) Photodiode voltage vs time. Labels 1-8 indicate standard concentrations from 0.25 – 50 μM in increasing order. (b),(c) Average absorbance of each sample concentration with error.

Likewise, the biggest jump occurs between the blanks of the second last and last standards. This suggests that the issue is due to crosstalk between samples and blanks. The influence of this crosstalk, however, is minimal relative to the actual colour-development but could be reduced with optimized injection volumes and/or flow rates.

Figure 3.22(b) and Figure 3.22(c) show the average absorbance at each sample concentration where the latter provides a closer-view of the absorbance of the lowest-concentration samples. Once again, as expected the data points adhere to a linear relationship. The equation of the linear fit applied to the data in Figure 3.22(b) and Figure 3.22(c) is given below:

$$\textbf{25.4 mm:} \qquad A_{PO_4^{3-}} = 0.0361[\mathbf{PO_4}^{3-}]; \qquad R^2 = 0.9990, \tag{3.11a}$$

with an error on the slope of $\pm$ 0.0003 $(\mu\text{M})^{-1}$.

The same range of phosphate standards were then measured using the three 880 nm LEDs described in Section 3.3.3 but this time with the 50.4 mm optical cell. Each LED had its own advantages over the others as outlined in Section 3.3.3. For example, the MTE8800NK2 was the easiest to align and required the least amount of input power to achieve photodiode saturation. Figure 3.23 shows the results of three blue phosphate experiments. Unlike with the 700 nm LED, each standard was measured in triplicate for each experiment. Only one LED was tested at a time, and the entire experiment (8 standards and 8 blanks $\times$ 3 measurements each = 48 measurements per experiment) was completed before switching to the next LED. All other conditions were identical to the 700 nm LED test.

Figure 3.23(a) and Figure 3.23(b) show the average absorbance at each sample concentration. Again, the second plot provides a closer-view of the absorbance of the lowest-concentration samples. The most concentrated standard, 50 μM, absorbed too much light to adhere to the Beer-Lambert law and was therefore omit from inclusion with each applied linear fit. Standards ranging from 0.25 – 25 μM produced the expected linear relationship. The equation of the linear fit applied to the data in both

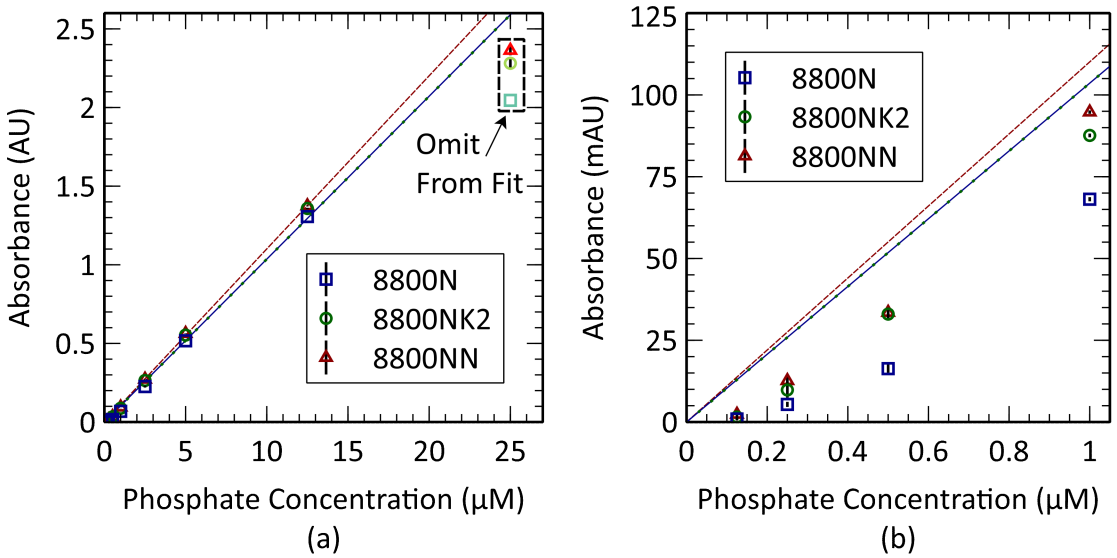

Figure 3.23: (a)-(b) Average absorbance with error of eight reacted blue phosphate samples vs. their phosphate concentration using each 880 nm excitation LED; $l = 50$ mm. A linear fit is applied to each data set.

Figure 3.22(a) and Figure 3.22(b) is given below:

$$\textbf{MTE8800N:} \qquad A_{PO_4^{3-}} = 0.1036[PO_4^{3-}]; \qquad R^2 = 0.9979, \tag{3.12a}$$

$$\textbf{MTE8800NK2:} \qquad A_{PO_4^{3-}} = 0.1086[PO_4^{3-}]; \qquad R^2 = 0.9993, \tag{3.12b}$$

$$\textbf{MTE8800NN:} \qquad A_{PO_4^{3-}} = 0.1101[PO_4^{3-}]; \qquad R^2 = 0.9995, \tag{3.12c}$$

where each path length was 50.4 mm as stated.

These fits were used to find each attenuation coefficient: these are shown in Table 3.7. As discussed previously, these quantities are specific to the inspection light wavelength. Therefore, the results of the 700 nm test and the 880 nm tests must be analyzed separately.

A attenuation coefficient for phosphate was found to be $\epsilon_{PO_4^{3-}} = 0.0142(\mu M \cdot cm)^{-1}$ using the 700 nm light source and $\epsilon_{PO_4^{3-}} = 0.0213(\mu M \cdot cm)^{-1}$ using the 880 nm light sources. In comparison, [41] obtained attenuation coefficients ranging between

Table 3.7: Experimentally obtained attenuation coefficients ϵ for phosphate (blue method). $\bar{\epsilon}$ is the average with standard deviation. The approximate wavelength of each excitation LED is indicated.

Blue Phosphate

l (mm)	λ (nm)	$\epsilon_{PO_4^{3-}}$ $(\mu M \cdot cm)^{-1}$	$\bar{\epsilon}_{PO_4^{3-}}$ $(\mu M \cdot cm)^{-1}$
25.4	~700 nm	0.0142	0.0142
50.4	~880 nm	0.0206	
50.4	~880 nm	0.0215	0.0213 ± 0.0007
50.4	~880 nm	0.0218	

0.0052 – 0.0059 $(\mu M \cdot cm)^{-1}$ upon measuring standards up to 10 μM. Their method used the same 700 nm light source but with a different reagent composition. This indicates that the reagent make-up used here may produce more colour-development and therefore more sensitive readings. The consistent results shown here further supports the performance of this novel optical cell and demonstrate the reliable and sensitive results produced by this colour-development technique.

3.4.5 Detection Limits

The LOD is typically used to describe the lower-bound of a sensor's measurement range. The LOD states the lowest concentration at which a sample can be detected (but not necessarily quantified) [58]. The LOD provides a useful measure of a sensing apparatus' measuring capabilities and is specific to each species measured. The resolution of the system can be quantified by measuring the average noise of n blanks. The LOD for each species was evaluated for each optical path length using the standard triple-sigma literature method [58], which uses three-times the blank baseline noise as a reference. A blank value of 4.80 V – just below photodiode saturation – was chosen to convert each LOD from voltage to absorbance units. The absorbances were then converted to concentrations by dividing by the respective slope for each species at that path length. These results are summarized in Table 3.8 below for nitrite and

both phosphate methods. These detection limits are consistent with those found in the literature; for example, Sieben *et al.* in 2010 had an LOD of 14 nM for nitrite using a 25 mm optical path [14]. Likewise, Legiret *et al.* in 2013 had an LOD of 52 nM using a 25 mm path and the yellow phosphate method [39]. Furthermore, Grand *et al.* in 2017 obtained LODs ranging from 30 – 40 nM using the same 700 nm light source as here (LED700-02AU, Roithner) but over a 98 mm path length and as part of a completely integrated sensor [4]. A notable trend is that, among each path length, the average noise of the nitrite blanks is greater than those of the phosphate blanks: this may be a consequence of the manual sample injection method used for the nitrite samples. A benefit of automated sample injection is more consistent injection flow rates between each sample.

Table 3.8: LODs for each measured species; n represents the number of blanks analyzed. Absorbance units are converted into concentration using the calibration curve for each species and path length combination.

Species	**l (mm)**	**n**	**Avg. Blank Noise (mV)**	**LOD (mAU)**	**LOD (nM)**	**LED**
Nitrite	10.4	23	3 ± 2	0.9 ± 0.6	30 ± 20	Cree
	25.4	31	4 ± 5	1.0 ± 1.3	14 ± 19	Cree
	50.4	22	3 ± 4	0.7 ± 1.0	6 ± 8	Cree
Nitrate	25.4	N/A	LOD related to Time & Temp.			Cree
Y. Phos.	10.4	24	1.3 ± 0.9	0.3 ± 0.3	100 ± 80	RL5-UV0315-380
	25.4	20	2 ± 2	0.6 ± 0.6	60 ± 70	RL5-UV0315-380
	50.4	23	2.7 ± 1.8	0.7 ± 0.5	40 ± 30	RL5-UV0315-380
B. Phos.	25.4	39	1.2 ± 0.8	0.3 ± 0.2	9 ± 6	LED700-02AU
	50.4	19	2 ± 2	0.6 ± 0.5	6 ± 5	MTE8800N
	50.4	24	2 ± 2	0.6 ± 0.7	6 ± 6	MTE8800NK2
	50.4	23	1.9 ± 1.6	0.5 ± 0.4	5 ± 4	MTE8800NN

The detection limit of nitrate is a more complicated issue. Due to the slow colour-development and temperature dependence, it is more difficult to compare trials that were not conducted under these same reaction time and temperature conditions. The set of tests that produced the best LODs (*the lowest*) were the tests that used heat

to accelerate the reduction process. The slope of the more accurate linear fit applied in Figure 3.16 (purple) is almost 8 times that of the fit in Figure 3.14. This indicates roughly 8 times the sensitivity between absorbance and concentration when reacting at 41 °C vs. RT. Improved sensitivity has a positive influence on the LOD of the system. Ideally, an increase in sensitivity by some factor should improve the LOD by the same factor; in practice, however, this is not always the case. Observed in the RT triplicate was an average blank noise of 0.0012 ± 0.0019 V from 24 blanks. Using three times this value, this equates to an LOD of 0.5 ± 0.8 mAU using a typical blank value to convert from voltage to absorbance. Using the slope of the absorbance vs. concentration curve in Figure 3.14, this equates to a concentration of 50 ± 80 nM. In the heated triplicate trial, however, the average blank noise was higher: 0.0029 ± 0.0012 V from 24 blanks. Using the slope of the curve in Figure 3.16, this resulted in an LOD of 0.8 ± 0.3 mAU or 11 ± 5 nM. Despite having 8 times the sensitivity, the LOD improved only by a factor of 5 – this is likely due to crosstalk between samples being more prominent over the longer path length.

Due to the added integration complexity, the limit-of-quantification (LOQ) might be more appropriate as a lower sensing bound when these inlaid flow cells are integrated into marine sensors. The LOQ differs from the LOD in that it describes the lowest sample concentration that can be measured with enough precision and accuracy to be quantified [58]. The LOQ is determined in the same way as the LOD but uses ten times the blank noise. In this case, the LOQ would be 20 nM for nitrite, 36 nM for nitrate at 41 °C, 150 nM for phosphate (yellow), and 16 nM for phosphate (blue). These limits best match the results observed during calibration testing.

Throughout Sections 3.4.1 – 3.4.4, instances of non-linearity between sample measurements and the calibration curve have been observed. Instances of non-linearity have occurred at both the lower and upper bounds of calibration testing in some instances.

An example of non-linearity at the lower end can be seen in Figure 3.23(b) where the data points consistently reside beneath the fit line. This was most apparent in the yellow phosphate 10 mm tests where the lowest-two concentration samples were barely discernible from their blanks. Non-linearity observed for lower-concentration data points occurs due to a combination of fluidic and optical noise and is best described using the LOD/LOQ as detailed above. Similarly, non-linearity can be observed in some instances for heavily concentrated samples. As an example, the 50 μM measurements shown in Figure 3.23(a) for each of the three tests all reside below the otherwise linear curve. For heavily concentrated samples, this non-linear behavior may arise from a combination of factors. Firstly, spectral shift due to dipole-dipole interactions at high sample concentrations will influence measurements. This can be better accounted for by using an excitation light source that is spectrally aligned to the center of the peak of the absorption curve of the sample. Secondly, for high absorbances, the combination of internal photodiode noise and background light noise becomes more influential – this is further discussed in Appendix A.

3.5 Complete System Integration

Together with Sean Morgan, Joshua Creelman, and Benjamin Murphy, a lab-on-chip system containing two inlaid optical cells (l = 10, 25 mm) and 4 microfluidic check-valves was fabricated to validate our approach with more complicated integrations. In a deployment scenario, having a second optical channel with a shorter path length can be beneficial when entering highly concentrated nutrient-rich zones but has lower sensitivity to minor concentration fluctuations. Figure 3.24 depicts the fluidic schematic of the lab-on-chip. Microfluidic flap-based check valves were integrated within the chip to govern the direction of fluid flow while pumping. The sample intake port of

the sensor (SP) was connected via tubing to the output of a 10-port selector valve (not shown). The selector valve was used to sample either one of eight nitrite standards or Milli-Q. The reagent intake tube (GR) was connected to a bag containing freshly-prepared Griess reagent. Both sample and reagent channels joined at a Y-junction after which the two fluids mixed via diffusion in a microfluidic mixing chamber. Two inlaid optical cells with 25 mm and 10 mm path lengths were then used to capture any colour-development via light absorbance. To acquire measurements, flow was stopped for 5 minutes and the voltage for both optical channels was recorded. The last 30 s of each measurement were averaged to acquire the voltage used for absorbance and concentration calculations. After this period, flow resumed, and mixed samples were dispensed from the chip to a waste container. Figure 3.25(a) shows the physical

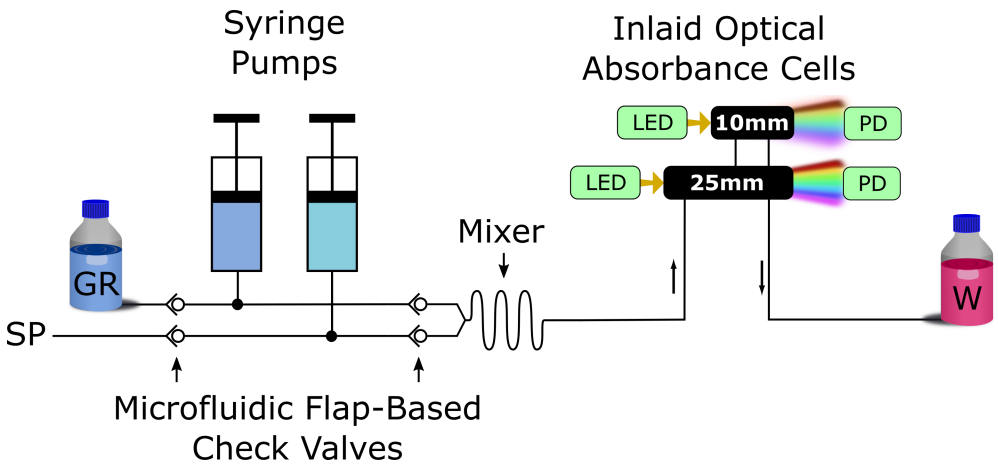

Figure 3.24: Flow schematic for a lab-on-chip nitrite sensor using inlaid optical cells. SP refers to the sample intake port of the chip and GR refers to the Griess reagent intake. Sample and reagent join at a Y-junction and mix via diffusion in a microfluidic mixing chamber. Developing samples are analyzed using two inlaid optical cells before dispensing to a waste container (W in the diagram).

implementation of the system. Two 250 μl syringes – one for sample and one for reagent – were connected to the chip and were responsible for pumping. A single stepper motor was utilized for actuation of both syringes such that both were pulled or pushed simultaneously. The two syringes were screwed into the top of the transfer

plate and O-rings between the chip and plate established a fluidic seal via compression. Optical components were also held in slots machined into the transfer plate to maintain alignment with the chip. A custom PCB integrated the electronics to handle stepper motor control (pumping), hall effect sensing (plate position), analog signal processing, data storage and interfacing to a Raspberry Pi Zero, located at the top of the sensor. Custom firmware was also created to automate the sampling process mentioned above. The final lab-on-chip sensor is shown in Figure 3.25(b). The results of the three lab-on-chip nitrite sensor tests are shown in Figure 3.26. Eight nitrite standards between 0.1 – 20 μM were analyzed from low to high concentration using both optical cells. Blank measurements were taken before each sample, comprised of both Milli-Q and Griess reagent in the same volumetric ratio. One complete test consisted of 8 nitrite and 8 blank measurements for a total of 16 measurements per optical channel. Three of these tests were performed to assess measurement error and to quantify the reliability of the completely integrated lab-on-chip system. The same standards and reagent were used for all three tests, and all three tests were conducted within a two-day period.

Figure 3.26(a) shows a time series of the raw photodiode output voltage produced by the photodiodes measuring each optical channel. Gaps in the data after each blank and sample measurements are during pumping during which measurements of the background light were taken by turning both LEDs off – data not shown. Lower voltages are observed in each 10 mm test – approximately half the normal voltage reading when measuring blanks – due to misalignment between LED and prism. The slot in the transfer plate holding that LED was machined slightly offset to the window of the optical cell which prevented proper light coupling. This can easily be fixed in future designs by modifying the machining of the transfer plate.

The 25 mm long optical cell produced expected and repeatable results for each of the

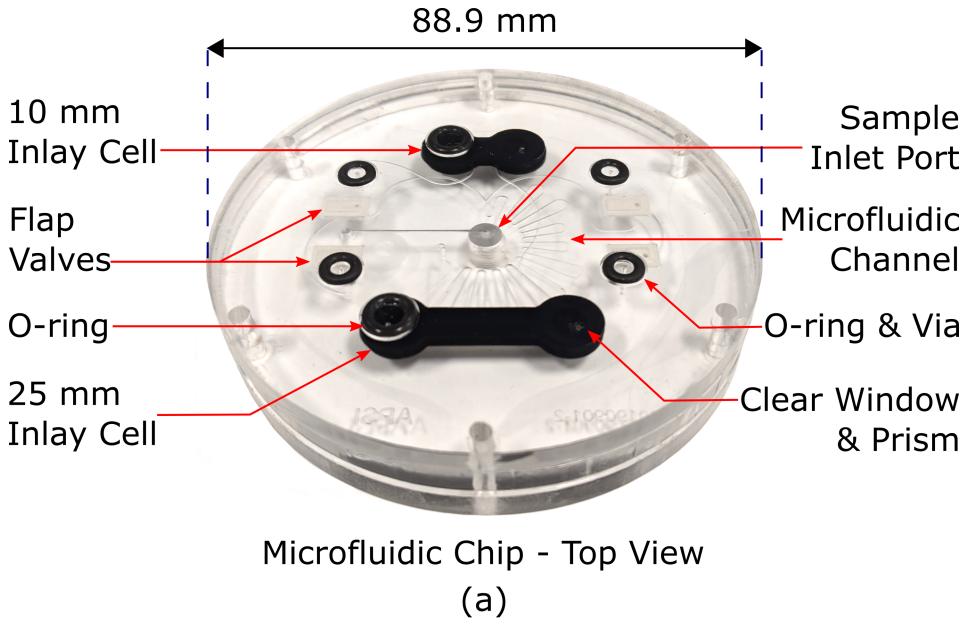

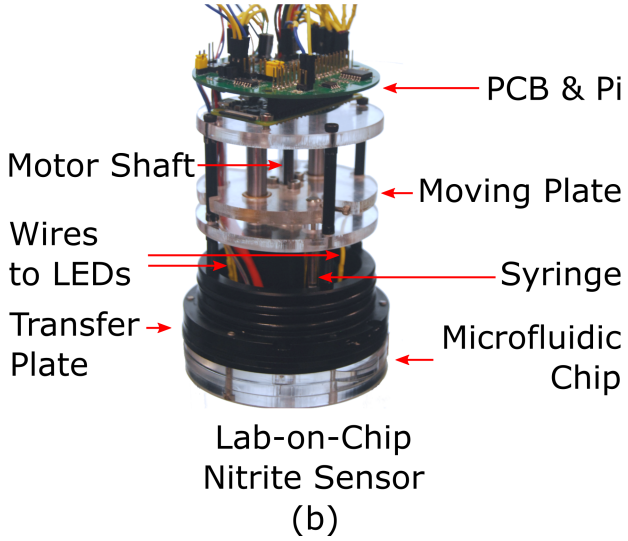

Figure 3.25: (a) Photograph of the microfluidic chip with labelled features. The chip has a diameter of 88.9 mm and a thickness of 16 mm. (b) Lab-on-chip nitrite sensor photograph.

three tests. The dark blue, maroon, and black data points in Figure 3.26(a) depict the voltage time-series of each of the three 25 mm tests and are self-consistent apart from the final blank reading. The drop in the final blank measurement observed in tests two and three is indicative of crosstalk from the previous sample: this could be remedied with more comprehensive flushing between samples. Small vertical er-

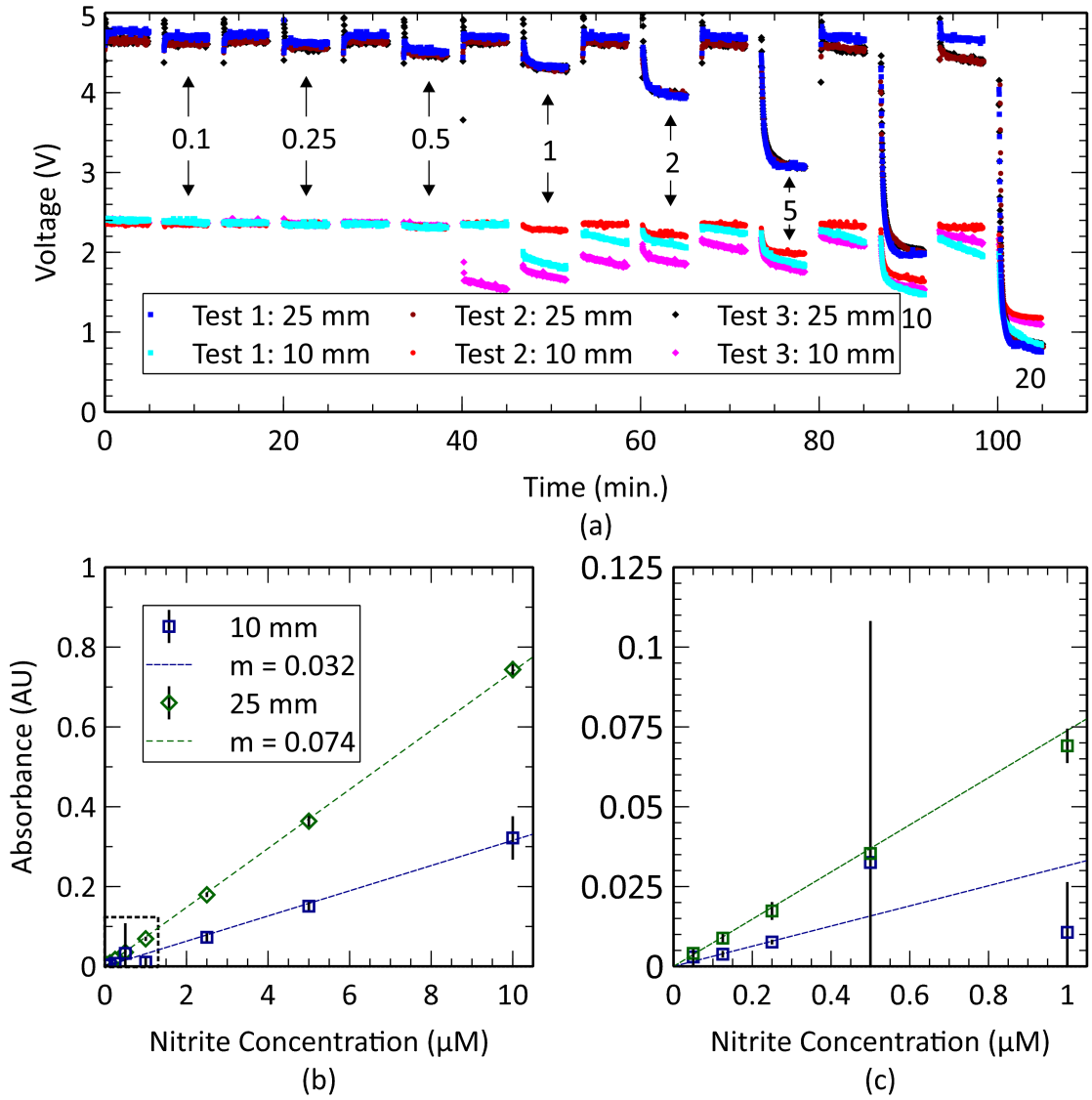

Figure 3.26: Results from a benchtop calibration experiment of the automated lab-on-chip nitrite sensor. (a) Raw photodiode voltage measurements taken during each of the three tests from both photodiodes. Times are determined from the beginning of each test, starting when pumping of the first blank begins. Labels indicate the concentration of the standard injected through the sample port. (b),(c) Light absorbance measurements plotted against sample concentration assuming a 1:1 mixing ratio between standard and reagent. Blue data points are averaged absorbance measurements taken using the 10 mm optical cell and green with the 25 mm cell. Error bars represent standard deviations; the large error bar seen at 0.5 μM corresponds to the reading of the 0.5 μM sample with the 10 mm path.

ror bars in figures 3.26(b) and 3.26(c), calculated as the standard deviation of each repeated measurement, confirm highly consistent results over the whole 0.1 – 20 μM domain. Figure 3.26(c) better represents the data for lower concentrations, showing close conformity between these data points and the overall trendline. The LOD of the 25 mm path was determined following Section 3.4.5 to be 39 $\pm$ 8 nM. The increased measurement noise from the photodiode led to a slightly worse LOD than that observed in the isolation tests where a high precision multimeter was used.

The 10 mm long optical cell produced unexpected results, as shown by the time-series data in Figure 3.26(a). The three tests represented by the cyan, red, and magenta data points were not consistent. Test 2 produced the expected linear relationship over the entire concentration range, with a fit of $A = 0.029[NO_2^-]$ and an R^2 of 0.9995. Tests 1 and 3 produced data in excellent agreement with test 2 for the first three samples of 0.1, 0.25 and 0.5 μM. However, tests 1 and 3 were subject to measurement errors for the next three samples, which included 1, 2 and 5 μM samples. For example, in test 3 there is an unexpected and large drop in the voltage data. The drop in voltage persisted over the next three measurements but trended back toward the expected baseline. This is attributed to a bubble being trapped in the measurement cell that was gradually dislodged. The inlaid optical cell design, like most fluidic systems, is prone to bubble measurement errors; however, less so than wide channel designs. To detect and account for these errors, on-board standards should be carried for autonomous *in situ* deployments. After the bubble was cleared from the short path length cell, the 10 and 20 μM samples measured consistently for all three tests.

The correlation slope of the 25 mm and 10 mm absorbance vs. concentration curve is approximately 10 % higher than those determined in Section 3.4.1, Figure 3.11. This offset is attributed to biased mixing between reagent and sample. Ideally, both sample and reagent were pumping in equal volumes since they both actuated together.

However, the check-valves may have had some degree of backflow, altering the mixing ratio. If a sample-to-reagent volumetric ratio of 55:45 is assumed, then these slopes match those in Section 3.4.1. This indicates the reagent valve had a backflow of approximately 5 %. Future work should focus on improving check-valve performance and to attain an expected 1:1 ratio. However, on-board standards would allow for a correction to the linear relationship, even if the mixing ratio is non-ideal. Overall, it is concluded that over the tested concentrations, the lab-on-chip sensor based on the inlaid optical cell produced highly repeatable and accurate nitrite detection.

3.6 Conclusion and Summary of Results

The fabrication process of a novel optical absorbance cell is presented in which transparent and opaque PMMA are combined to create an isolated absorbance cell within a microfluidic chip. Optical components are decoupled from the chip using integrated v-groove prisms to improve manufacturability. Light absorbance measurements were performed using channels 400 μm wide and 600 μm deep. Optical path lengths were 10.4 mm, 25.4 mm, and 50.4 mm, for total sample volumes ranging between 2.5 and 12 μl. With optimization, we could readily achieve 100–200 μm channels and thus attain nanoliters per measurement. Samples of varying food dye concentration as well as nitrite, nitrate, and phosphate samples were used to verify the measuring capabilities of our novel inlaid approach. Excellent linear relationships were observed between absorbance and concentration for all tested samples. Going forward, the inlaid method of combining multiple types of PMMA will form the basis of many *in situ* marine sensors for high-performance colourimetric measurements. Here, a complete lab-on-chip nitrite sensor was demonstrated that used two inlaid optical cells to measure light absorbance with accurate and reproducible nitrite detection from

50 nM to 10 μM. Beyond absorbance measurements, PMMA of various colors could be utilized to implement filters for optical techniques like fluorescence spectroscopy or viewing ports to capture light from predetermined scattering angles. The "inlaid" approach will find broad applicability for performing optical measurements on lab-on-chip devices.

A more robust version of the prototype nitrite sensor introduced in Section 3.5 has since been professionally engineered – manufactured in collaboration with Dartmouth Ocean Technologies located in Dartmouth, NS. The sensor can be applied to detection of many different nutrients including nitrate, nitrite, and phosphate using the same colourimetric approaches introduced in this Chapter. Table 3.9 below summarizes the performance of this sensor for comparison with the commercial sensors outlined in Table 2.1 of Chapter 2 Section 2.2. Characterization of the performance of the sensor is currently in progress. However, the benchtop data obtained in this Chapter while testing the optical cell in isolation is a good approximation of the predicted performance of the sensor. Therefore, Table 3.9 contains a combination of benchtop (denoted with a B superscript) and sensor data.

The data contained within Table 3.9 are separated by optical path length and reaction temperature (for nitrate). Accuracy was evaluated using the calibration curves obtained in Section 3.4.1, Section 3.4.2, and Section 3.4.4. The accuracy values listed in Table 3.9 are specific to the range of samples tested in that calibration series. For each calibration curve, the maximum residual value (magnitude) of all tested samples from the fit of the calibration curve was used. This value is the most that any of the samples differed from the fit. In other words, this is the maximum error observed between the measured value and the true value for that range of samples. This gives a measure of the inaccuracy of the system. The largest residual of the calibration divided by the slope of the calibration curve yields a maximum error in μM, and this

value was taken to be the accuracy. For example, the largest residual of the blue phosphate 700 nm calibration was 0.022 AU and the calibration curve had a slope of 0.0361 AU/μM. This yields a mismatch of 0.61 μM between what the calibration curve predicts and the true concentration of the sample. This approach was used to calculate each accuracy value in Table 3.9 below. Likewise, the range and LOD values were determined from the calibration data from the same sections.

Table 3.9: Summary of results from Chapter 3. Benchtop optical cell calibration data obtained in isolation from the sensor are denoted with a superscript *B*. Wet chemistry methods are given superscripts 1 – 3 referring to the modified Griess reaction, the Griess reaction, or the blue phosphate method. Data are separated by the optical path length used and reaction temperature (for nitrate).

Sensor	**Dalhousie LOC Sensor**		
Species	NO_3^-	NO_2^-	PO_4^{3-}
Method	WC[1]	WC[2]	WC[3]
[B]**Acc. (μM)**	0.6 (25 mm, RT); 0.3 (25 mm, Heat)	0.5 (10 mm); 0.11 (25 mm); 0.17 (50 mm)	0.6 (25 mm, 700 nm); 0.3 (50 mm, 880 nm)
[B]**Range [Max.] (μM)**	50 (25 mm, RT); 25 (25 mm, Heat)	100 (10 mm); 20 (25 mm); 15 (50 mm)	50 (25 mm, 700 nm); 25 (50 mm, 880 nm)
[B]**LOD [Min.] (nM)**	50 (25 mm, RT); 11 (25 mm, Heat)	30 (10 mm); 14 (25 mm); 6 (50 mm)	9 (25 mm, 700 nm); 5 – 6 (50 mm, 880 nm)
Drift	Requires further study		
Power (W)	∼0.7 (idle), ∼7 – 10 (peak), heater N/A (NO_3^- only)		
Weight (kg)	5.90 kg (air), 3.57 kg (seawater)		
Volume (cm^3)	1519		
Depth (m)	N/A		

The results shown in Table 3.9 compare well with the commercial sensors introduced in Chapter 2 Section 2.2. The accuracy and LOD of our colourimetric nitrate and nitrite detection is superior to those of the SUNA V2 UV, Deep SUNA, and WIZ Probe. While the range of our nitrate and nitrite detection is better than that of the WIZ Probe, the range of the SUNA options, however, is far more extensive than our approach. In this regard, our approach excels at obtaining high-resolution nitrate

data but over a more narrow range of detection. In regards to phosphate detection, the accuracy of the commercial sensors are not known. Our range and LOD, however, are superior to those of the WIZ Probe and HydroCycle PO4. While more testing is needed to determine these metrics from an actual deployment scenario, these results provide an excellent benchmark for future developments.

Chapter 4

Fluorescence via Inlaid Microfluidics

This chapter presents a second optical cell configuration enabled by the "inlaid" method of Chapter 3. The majority of the experimental work in this chapter was done collaboratively with Joshua Creelman. Much of the initial proof-of-concept work and the chip manufacturing was done together with Gabryelle Béland.

4.1 Introduction

A microfluidic chip was fabricated to simultaneously measure the light absorbance and fluorescence of injected fluids. Figure 4.1(a) provides a cross-section perspective of the microfluidic chip to display the optical cell configuration. Similar to the chip designs of Chapter 3, this chip design uses embedded microprisms, inspired by the work of Grumann *et al.* [46], to couple light through the optical channel to excite contained fluids. Light sources are held perpendicular to the chip and are pointed down towards a first clear window. A portion of the emitted rays reflect off an embedded microprism towards an air-filled rectangular channel.

Figure 4.1(b) provides a perspective view of the chip with labelled features. A noteworthy feature of this chip design is the air-filled channel that separates the top prism from the microfluidic channel. This air channel is necessary to transmit light from the prism through the opaque PMMA. At the same time, the air-filled channel helps separate the incident window from the fluorescence measurement window by provid-

ing more physical distance between the two. This helps reduce the amount of incident light detected by the light detector at the spectrometer window.

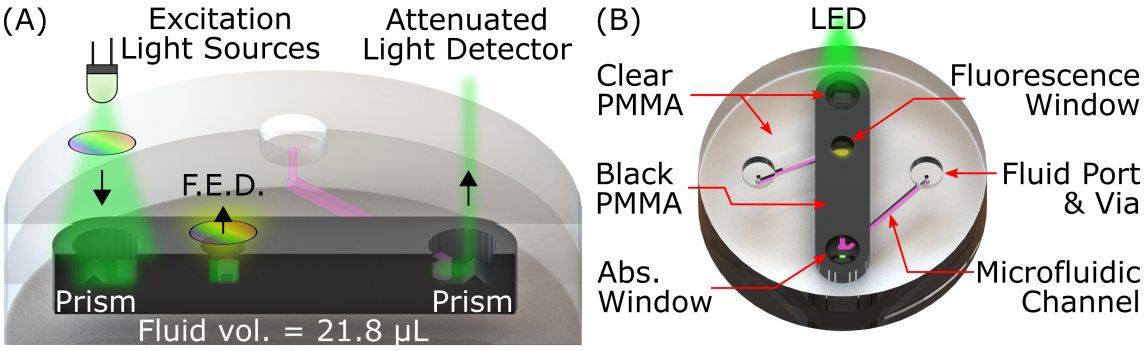

Figure 4.1: (a) Microfluidic absorbance/fluorescence chip cross-section CAD. F.E.D. is an abbreviation of fluorescence emission detector. (b) Chip perspective view CAD with labelled features. A rectangular air channel transmits light from the first clear PMMA window to the fluid channel

The same z-shaped microfluidic channel as discussed in Chapter 3 is used here. However, the design has been modified slightly in this case. At the top of the microfluidic channel – the portion observed by the fluorescence window – there is what we have called a "fluorescence well". Both the air-filled channel and the measurement well can be seen highlighted in Figure 4.2. Unlike the rest of the microfluidic channel which is rectangular, this portion is expanded and circular. The amount of fluorescence produced by a fluid is related to the amount of fluid the incident light source can excite. The amount of this total fluorescence that is measured is then related to the portion of it that reaches the light-detector. The well helps strengthen the measured fluorescence signal by increasing the total amount of excitable molecules in the region visible to the detector.

Figure 4.3 shows a flow diagram detailing the measurement process of one or more fluids. Each fluid is mixed in an equal ratio and injected into the microfluidic chip. One or more light sources are used to excite the fluid. The total amount of light absorbed by the fluid is measured using one spectrometer. Any light emitted by the

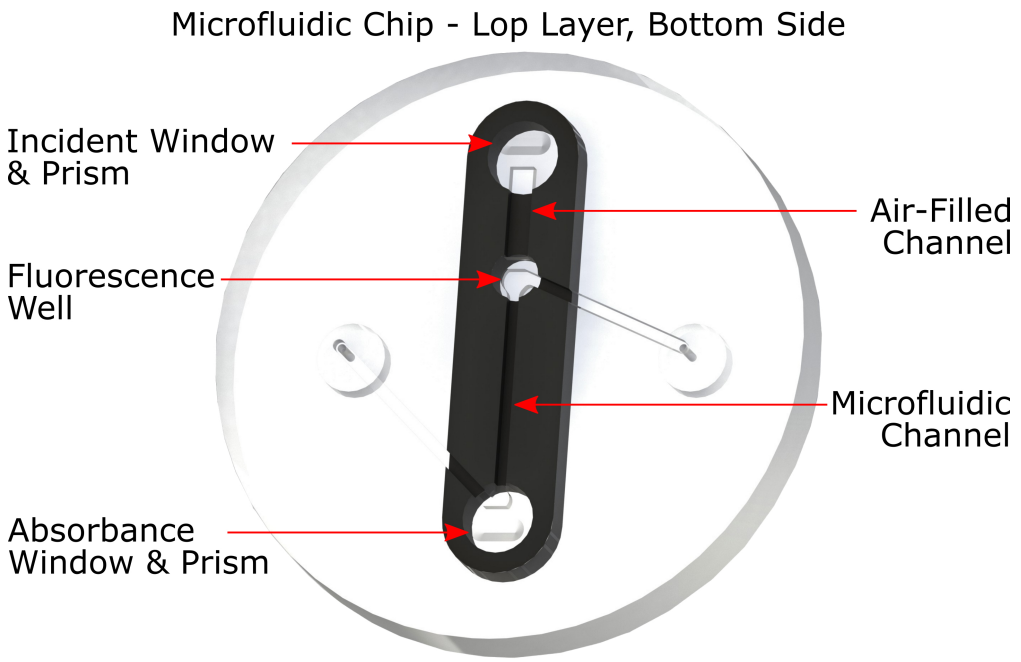

Figure 4.2: Microfluidic absorbance/fluorescence chip top layer bottom side with labelled features. The air-filled channel can be seen traversing through the opaque PMMA from the top clear window to the fluorescence window (containing the well).

fluid through fluorescence is measured simultaneously using a second spectrometer.

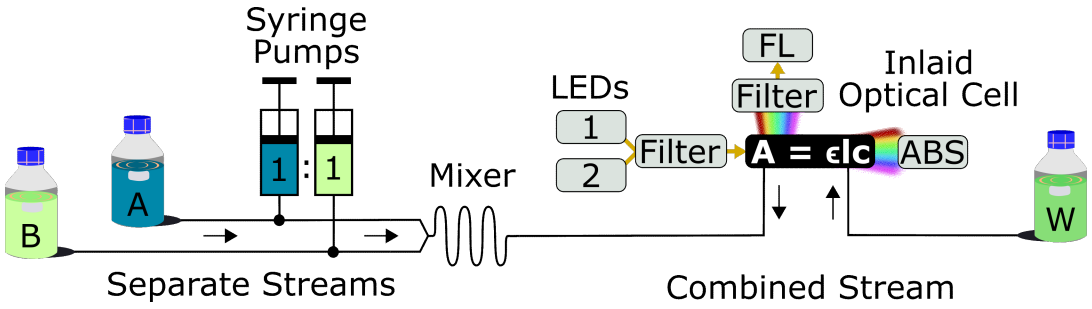

Figure 4.3: Sampling process: 2 separate fluids at intakes A and B combine in an equal ratio before inspection by light and ejection to waste (W).

As discussed in Chapter 2, any sensor designed for mass-production and long-term deployment must meet strict physical requirements. Power consumption, manufacturability, and sample volumes per measurement are critical metrics that define a sensor's compatibility towards wide-spread deployment with *in situ* sensing. Equally significant, however, is the performance of the sensor in acquiring accurate data.

Lab-on-chip sensors are particularly attractive due to their robustness in these areas [59].

Measurement consistency and sensitivity can be reasonably assessed in a controlled setting, *i.e.* through bench tests using calibration standards. Rhodamine dyes are excellent calibration standards due to their photostability [60, 61], high quantum yield [61], and well documented fluorescence emission lifetimes [59]. For example a fluorometer may be calibrated by measuring the fluorescence of a rhodamine B standard of known concentration [62, 63]. Our sensor was calibrated by measuring the light-absorbance and fluorescence of several prepared standards of rhodamine B. Figure 4.4 shows the absorption and emission spectra of rhodamine B. The relationships between absorbance, fluorescence, and sample concentration are examined over a concentration range of 0.1 – 10 μM.

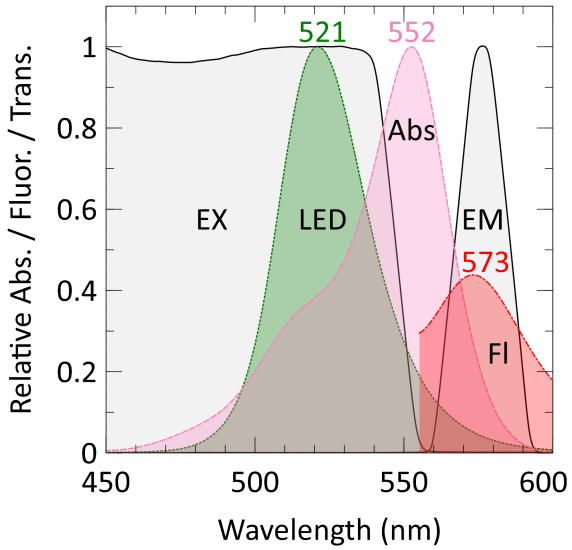

Figure 4.4: Experimental rhodamine absorbance and fluorescence spectra. The emission spectra of the excitation light source (LED) is also shown. Excitation (EX) and emission (EM) filters prevent spectral overlapping (experimental data shown).

4.2 Materials and Methods

4.2.1 Chemistry

The optical performance of the chip was first calibrated using seven different concentrations of the fluorescent dye rhodamine B. Milli-Q water was used as the solvent. The concentrations of each sample were: 0.1, 0.25, 0.5, 1, 2, 5, and 10 μM. First, a 2.5 g/L stock solution of rhodamine was prepared by diluting 0.5 g of rhodamine B ($C_{28}H_{31}ClN_2O_3$, $\geq$ 95 %, R6626, CAS 81-88-9, LOT SHBL5990, Sigma-Aldrich Canada) with Milli-Q water to a total volume of 200 mL. Each sample was then prepared, from highest to lowest concentration, through serial dilutions.

4.2.2 Chip Fabrication and Design

A bilayer microfluidic chip with an inlaid optical cell was used to simultaneously measure absorbance and fluorescence. The assembly of this chip is shown in Figure 4.5. A photograph of the fabricated chip is shown in Figure 4.6(a)-(b). The general process of inlaying opaque PMMA into clear PMMA has been described at great length in Chapter 3 Section 3.3.1. This will be summarized here with inclusion of any procedural changes to fabricate this chip. First, from a sheet of black extruded PMMA (9M001, Acrylite, USA), two black inserts were cut. In Figure 4.5, the design of the top insert is shown in the first step hovering over the clear sheet of PMMA. The straight thin strip of black PMMA with rounded ends and three cylindrical cuts is the top insert while the one without the cuts is the bottom insert. Upon completion, the cylindrical cuts of the top insert would be filled with clear PMMA and form a seamless interface. These act as optical windows for light to transmit into/out of the optical cell. The two cuts at either ends had diameters of 6 mm while the middle cut

had a 4 mm diameter. The dimensions of the bottom insert were identical to those of the top but without the described cylindrical cuts.

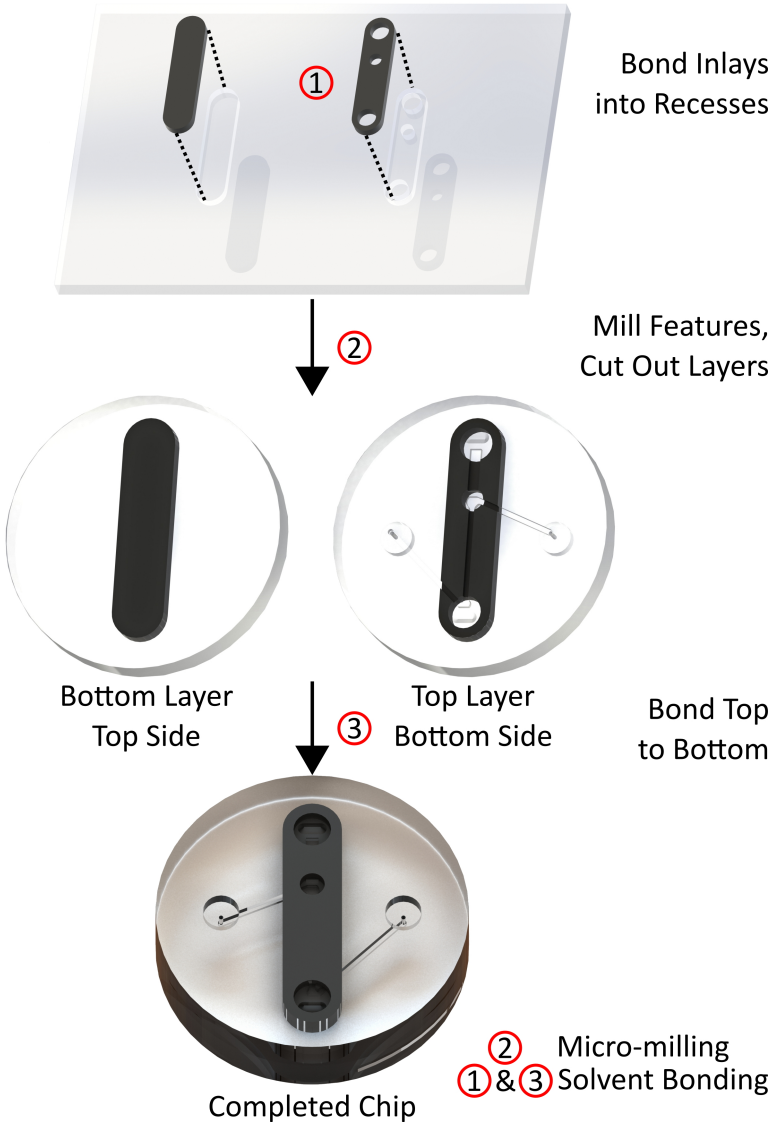

Figure 4.5: Absorbance/fluorescence chip CAD assembly

Second, from a sheet of clear extruded PMMA (0A000, Acrylite, USA), cavities were machined for each insert. The dimensions of each cavity matched their corresponding insert but with an added tolerance of 25 μm. The inserts were then pressed into their cavities to form a fluidic bond. The bonding process included a thermal, solvent, and pressure component: these parameters are detailed in Chapter 3 Section 3.3.1.

The added tolerance of 25 μm to the cavities was necessary to ensure that the inserts would press into the cavities with uniformity.

Third, now with black PMMA inlaid into the sheet of clear PMMA, features were milled. These features included microchannels, prisms, vias, and syringe ports. Two different channels were created. The first, the fluid channel, had a width and depth of 1 mm. The fluid channel was cut in a z-shape as seen in Figure 4.2. This channel could be filled with fluid by screwing a syringe or tubing into either syringe port. The second, an air channel, was 2 mm wide, 1 mm deep, and 7.7 mm long. This channel provided a path for light reflecting off the top prism to reach the fluid channel. Only a portion of the reflected light rays were directional enough to traverse the channel and reach the fluid channel. Non-directional rays were attenuated by the black surroundings.

Fourth and finally, the two layers of the microfluidic chip were cut from the sheet. The top layer was then bonded to the bottom layer using the same thermal, solvent, and pressure process detailed in Chapter 3 Section 3.3.1 to bond multiple layers together. After pressing, assembly of the microfluidic chip was complete.

4.2.3 Experimental Setup

Injection of fluids through the microfluidic chip was achieved using several off-the-shelf components. A Vici Cheminert C65Z 10-port selector valve (Valco Instruments Co. Inc., Houston, TX) was used to pull from different samples without cross-contamination. Tubing connected each sample to a respective intake port on the valve. The output connected to the intake of an off-the-shelf Cavro XC syringe pump (Tecan Systems, San Jose, CA) which was used to achieve fluid flow. The output of the syringe pump was directly connected to the input of the absorbance/fluorescence

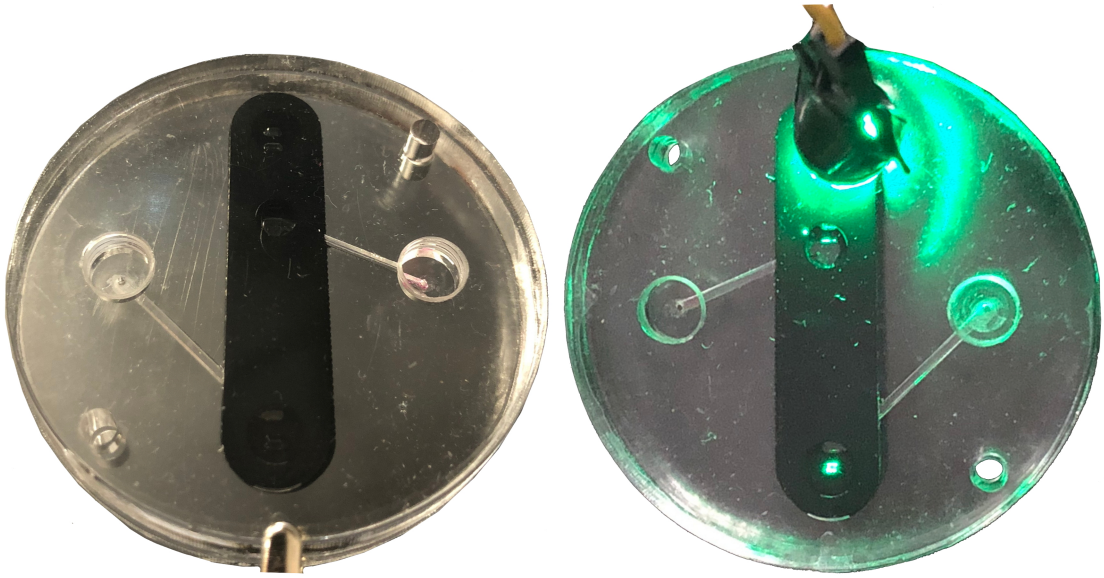

Figure 4.6: Microfluidic absorbance/fluorescence chip photographs. In (a), just the chip is shown. In (b), an LED light source is directed through the optical cell: in from the top prism and out from the bottom prism.

measurement chip. All fluids were pumped at a flow rate of 1.5 mL/min with stopped-flow during measurement data recording.

Figure 4.7 depicts the sampling and analysis flow diagram of the rhodamine absorbance and fluorescence measurement tests. Since only one fluid is inspected, this sampling procedure is a simplified version of Figure 4.3. Rhodamine excitation was achieved using a 521 nm LED (Cree C503B-GANCB0F0791-ND). This LED light source was chosen due to its strong emission output near the peak of the absorbance spectra of rhodamine B – see Figure 4.4(a). Excitation and emission filters were implemented – mounted onto the input and fluorescence windows – to prevent overlapping of excitation and fluorescence spectra. The choice of filters was dependent on the spectra of the measured species and the excitation light source. A 550 nm shortpass filter (Edmund Optics, 84695) and a 578 nm bandpass filter with a 16 nm bandwidth (Edmund Optics, 87738) were used as the excitation and emission filters.

All optical components were mounted and aligned to the chip using a 3D printed holder. —

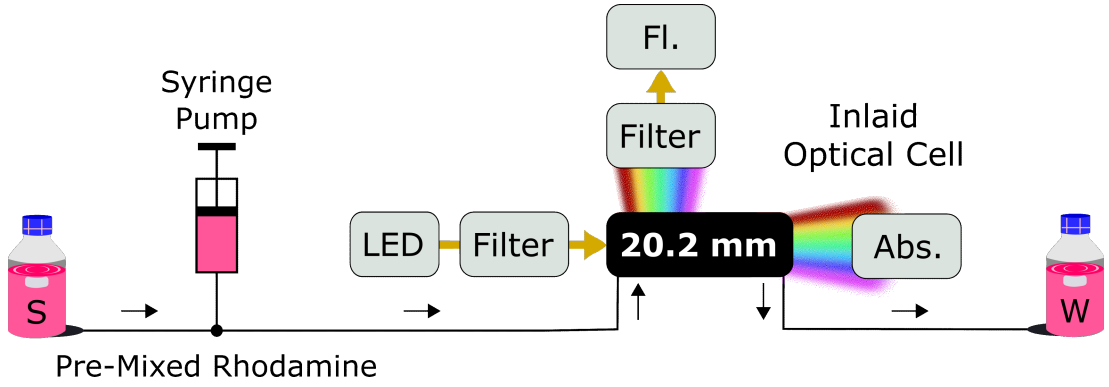

Figure 4.7: Rhodamine sampling procedure; S = sample intake, W = waste output. Fl. and Abs. indicate fluorescence and absorbance measurements.

Two spectrometers were used to acquire spectral measurement data. The first spectrometer (USB2000+, Ocean Optics) was interfaced via fibre optic cable to the absorbance measurement window labelled in Figure 4.1(b). The second spectrometer (Flame, Ocean Optics) was interfaced via fibre optic cable to the fluorescence window labelled in Figure 4.1(b). Both spectrometers were connected to a personal computer via USB. Data acquisition was controlled using software supplied by the manufacturer. Table 4.1 details the acquisition parameters used for each spectrometer.

Table 4.1: Data acquisition details

	Absorbance Window	**Fluorescence Window**
Spectrometer Model	USB2000+	Flame
Integration Time	20 ms	10 s
Scans Averaged / Measurement	3	3
Measurements / Sample	3	3
Filter	N/A	578 BP (16 BW)

4.2.4 Measurement Procedure

Before each sample measurement, a blank measurement was captured by filling the optical cell with Milli-Q. Blank measurements help quantify any carryover between successive sample measurements and provide a reference spectrum from which absorbance and fluorescence can be calculated. At each wavelength λ, absorbance is calculated such that:

$$A(\lambda) = -\log_{10}\left(\frac{S_a(\lambda)}{B_a(\lambda)}\right), \tag{4.1}$$

where $A(\lambda)$ is absorbance. $S_a(\lambda)$ is the counts of the spectrometer at the absorbance window when sample is in the optical cell. $B_a(\lambda)$ is the same as $S_a(\lambda)$ but during the prior blank. Fluorescence at each wavelength is calculated in a similar manner:

$$F(\lambda) = S_f(\lambda) - B_f(\lambda), \tag{4.2}$$

where $F(\lambda)$ is fluorescence. $S_f(\lambda)$ and $B_f(\lambda)$ are the counts of the spectrometer at the fluorescence window when sample or blank is in the optical cell.

The absorbance and fluorescence of each sample concentration was measured in triplicate to assess measurement consistency. The following details the measurement procedure of any given concentration. First, 3 mL of Milli-Q was pumped through the chip. Upon stopped-flow, the readings of both spectrometers were recorded simultaneously following the parameters detailed in Table 4.1. Three measurements were taken, each the average of three scans, for a total of nine scans per measurement. Next, 3 mL of sample was pumped through the chip, and the same readings are recorded after flow has stopped. This is repeated three times to acquire three measurements (27 scans) of the sample. The total data set would then include 27 absorbance and 27 fluorescence scans for each sample concentration with an equal

amount of blanks.

A LabVIEW program was written to process the acquired spectrometer data. The following details the function of the LabVIEW program in processing the data for each sample and blank. Firstly, the acquired data from either the absorbance or the fluorescence spectrometer would be loaded into the program: one text file per measurement snapshot. A total of 9 absorbance and 9 fluorescence measurements were recorded for every sample concentration – equivalent to 27 individual scans. These data were loaded into the LabVIEW program via a single prompt wherein several text files could be selected and uploaded at once. The program then produced several graphs from the uploaded data. Three plots of counts vs. wavelength was shown: one for each individual sample, averaged from the 9 scans. Another plot showed the average of the three samples. Several text files containing the processed averaged data could then be exported to a user-specified directory. This process was then repeated for the data set of the other spectrometer, thus concluding the data processing of one sample concentration. Using this program, the complete data processing of 7 samples (with blanks) took roughly 1 hour.

4.3 Results and Discussion

Figure 4.8 shows the results of a Rhodamine calibration series. Seven samples of Rhodamine B ranging from 0.1 – 10 μM were analyzed following the procedure detailed above. Figure 4.8(a) plots absorbance vs. wavelength for a series of rhodamine samples. Each curve, differentiated by colour, represents a different sample concentration – labelled in the legend of the plot. Each concentration was measured in triplicate: thus, each curve represents the averaged absorbance vs. wavelength data. A trend can be observed in the data such that more concentrated samples of rhodamine absorbed

more of the incident light source. Interestingly, the 0.1 and the 0.25 μM concentrations produced negative absorbance readings just above 550 nm. In both samples, these slightly ($<$ 500 mAU) negative readings were the result of a single outlier trial. It is likely that the cause of this was an air bubble being present within the optical channel. The fluorescence readings, however, were unaffected: this suggests that the bubble must have been beyond the fluorescence window.

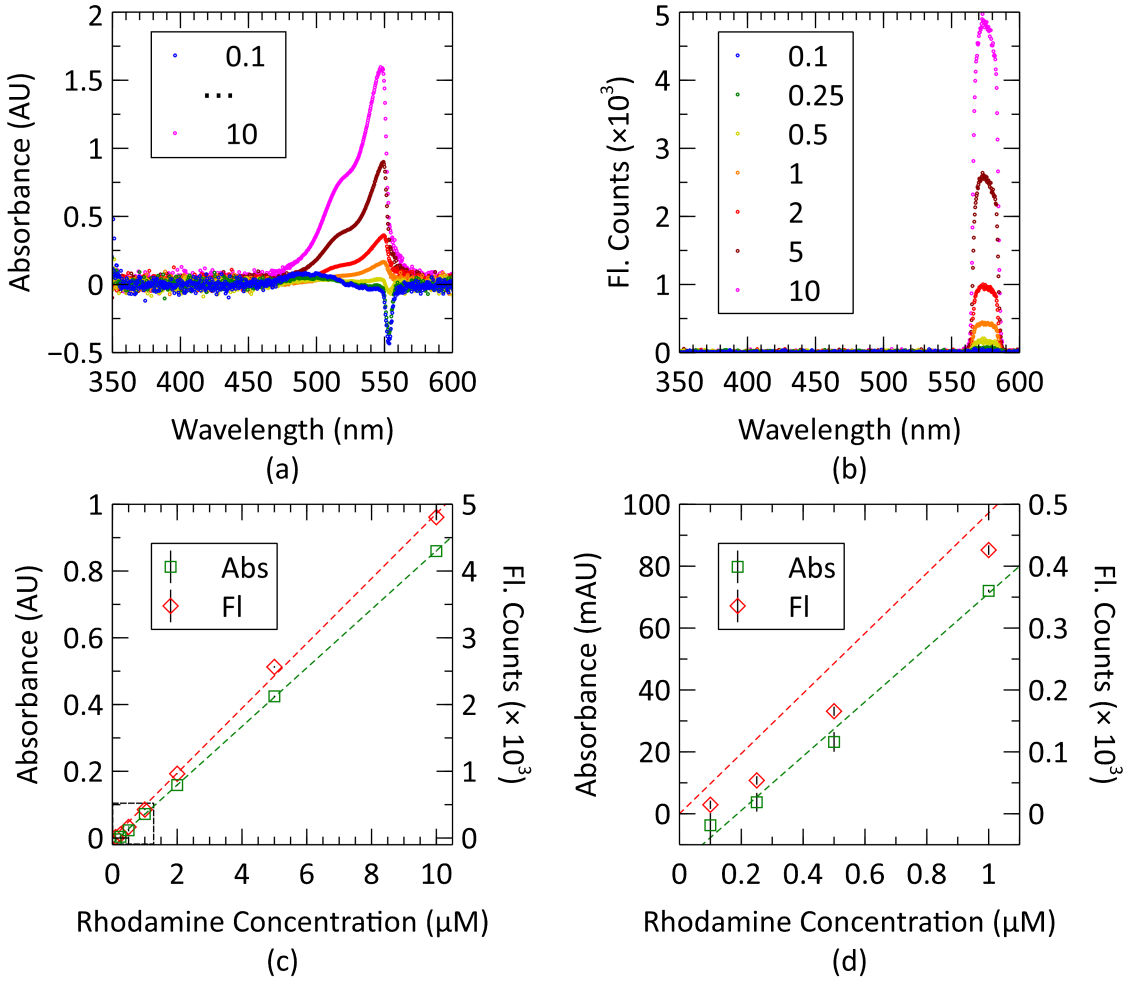

Figure 4.8: Rhodamine calibration testing results from seven rhodamine concentrations (n = 3). (a) Average absorbance at each wavelength for each sample. (b) Average fluorescence vs. wavelength for each sample. (c) Average absorbance and fluorescence plotted against wavelength (error = standard deviation). (d) Closer-view of the $\leq$1 μM samples in (c).

Figure 4.8(b) plots fluorescence vs. wavelength for the same samples. Sample concen-

trations are differentiated by colour using the same colour scheme as Figure 4.8(a). The measured fluorescence of each sample had a sharp cut-off on either end due to the cut-off of the emission filter mounted to the fluorescence optical window. As seen in the plot, the lowest concentration sample produced the lowest amount of fluorescence – shown by the blue data points. As sample concentration increased, so too did their emitted fluorescence output. The most concentrated sample, 10 μM, produced the most fluorescence as expected by this trend – shown by the pink data points.

Figure 4.8(c) combines the findings of figures 4.8(a) and 4.8(b). The data of the lowest-concentrations samples can be better observed in Figure 4.8(d). Here, both absorbance and fluorescence are plotted against concentration. Absorbance measurements are in green while fluorescence measurements are in red. The absorbance of each sample concentration is calculated as the average absorbance over a 5 nm window centered at 527 nm. Likewise, the fluorescence of each is calculated by averaging the fluorescence measurements between 570 – 575 nm. A line of best-fit between absorbance and concentration was calculated such that A = (0.0877 $\pm$ 0.0007)C - (0.016 $\pm$ 0.003). Similarly, a line of best-fit between fluorescence and concentration was calculated such that F = (486 $\pm$ 11)C. When applied to each data set, R^2 values of 0.9999, and 0.9988 were obtained. This demonstrates that, in either case, a linear model is justified to describe these data.

4.4 Conclusions

A microfluidic chip was successfully fabricated to simultaneously measure the light absorbance and fluorescence of injected fluids. Similar to the chip designs of Chapter 3, this chip design uses embedded microprisms to couple light through the optical channel to excite contained fluids. Measurement consistency and sensitivity evaluated

through calibration testing by measuring the light-absorbance and fluorescence of several prepared standards of rhodamine B over a concentration range of 0.1 – 10 μM. Two off-the-shelf spectrometers were used to collect spectral measurements. This work will provide the foundation for a more complicated *in situ* sensor that uses fluorescence measurements of pigments in cells to identify HAB-susceptible environments.

Chapter 5

Conclusions

5.1 Thesis Summary

The purpose of this thesis was to enable the creation of robust low-cost oceanographic sensor systems for wide scale deployment. In Chapter 2, the motivation behind the creation of these sensor systems was discussed with reference to current methods of oceanographic variable monitoring. In Chapter 3, a novel type of microfluidic light absorbance cell was introduced and applied to the measurement of three key nutrients to ocean environments: nitrite, nitrate, and phosphate. This optical cell was then successfully integrated within a completely automated lab-on-chip nitrite sensor. In Chapter 4, the light absorbance cell of Chapter 3 was modified to simultaneously acquire fluorescence data. The new design was successfully applied towards the measurement of a fluorescent dye rhodamine B.

5.2 Future Directions and Applications

The work of Chapter 3 will provide the foundation for more complicated system integrations of the inlaid optical cell for *in situ* measurement. A prototype lab-on-chip nitrite sensor was introduced and successfully calibrated on the bench using ideal testing standards of single nutrient concentrations. However, when deployed in a real environment, a number of challenges will be introduced. Firstly, the sensor must be able to withstand the hydrostatic pressure of the surrounding ocean: a function of

its depth. The maximum pressure tolerance of the sensor should first be thoroughly tested before deployment. In collaboration with Dartmouth Ocean Technologies, we have created a more robust version of the sensor introduced in Chapter 3 – this is shown in Figure 5.1. The sensor was designed with this hydrostatic pressure issue in mind but, as of this writing, has not yet been pressure tested.

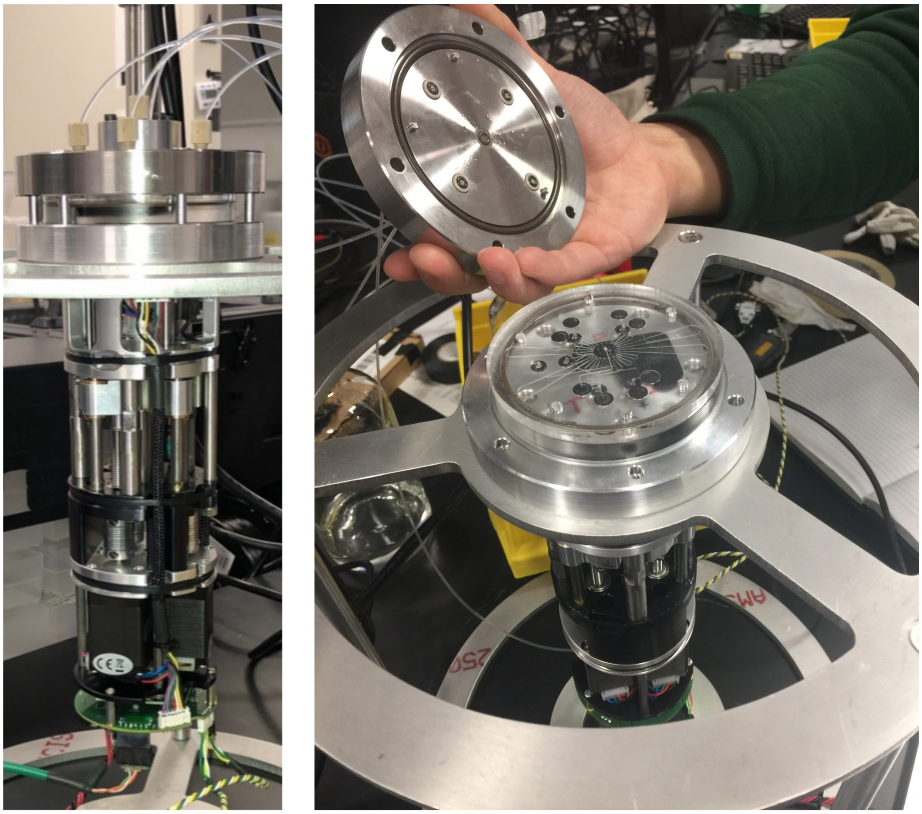

Figure 5.1: Professionally engineered lab-on-chip nutrient sensor developed with Dartmouth Ocean Technologies. (a) Side view. (b) Perspective view with microfluidic chip containing two inlaid light absorbance optical cells.

Secondly, the nutrient calibration performed here was done under ideal conditions. Testing standards were comprised of only one nutrient at a time using heavily filtered water. In a deployment, environmental samples will need to be heavily filtered at the sensor intake to remove unwanted particulate matter. Furthermore, for any of the explored colourimetric techniques, any interferences from other nutrients must be

well quantified. For example, it is known that arsenic and silicate can interfere with the blue method phosphate method [41]. A multiplexed calibration series could be performed to quantify the influence of a known interfering species. This would be a useful study to obtain more accurate environmental readings.

Finally, Chapter 3 discussed the issue of bubbles and light absorbance measurements. When performing benchtop tests, bubbles are sometimes introduced to the system when pumping. These bubbles are usually introduced at either the off-the-shelf syringe pump or the selector valve. While this issue is not relevant when deployed, as the entire sensor is submerged underwater, it can hinder a benchtop calibration. Implementation of an in-line bubble trap may be beneficial for testing, but not many commercial options exist. Addressing this issue during the chip manufacturing process may make for an interesting thesis project for a future student. Similarly, the heated nitrate calibration series showed that dissolved gases within a sample may expand under certain temperature and pressure conditions. This expansion has a similar influence on measurements to bubbles. It may be beneficial for future studies to first de-gas standards using a vacuum oven.

The work of Chapter 4 is the first step towards integration of our simultaneous absorbance and fluorescence inlaid cell within an *in situ* environmental sensor. A stable fluorescent dye rhodamine B was used here with a high quantum yield to benchmark the performance of the system. Next, the sensing unit should be applied towards detection of cells in fluids. At the time of writing this thesis, cell cultures containing chlorophyll a and c-phycocyanin have been inoculated for testing pigment detection with the absorbance/fluorescence chip shown in Chapter 4. Figure 5.2 shows the absorption and emission spectra of both chlorophyll a (dashed) and c-phycocyanin (dotted). Both Chl-a and C-PC are useful indicators of potential HAB-spawning environments. In the future, the microfluidic absorbance/fluorescence chip will be in-

tegrated into a complete *in situ* lab-on-chip sensor capable of simultaneously detecting both pigments.

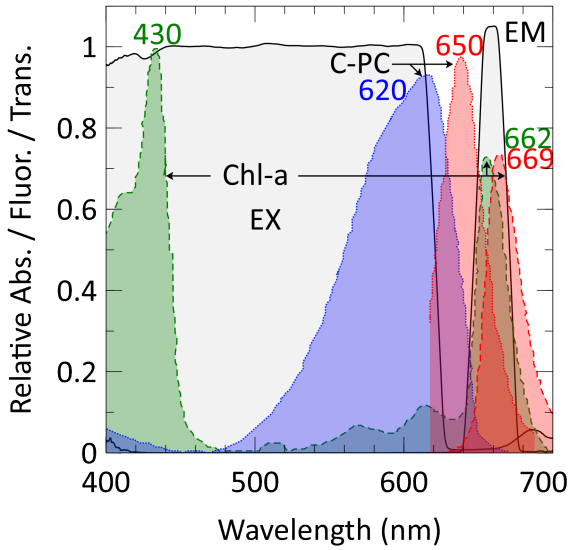

Figure 5.2: Reference Chl-a and C-PC absorbance and fluorescence spectra from [64]. The transmission spectra of proposed excitation (EX) and emission (EM) filters are shown to prevent spectral overlapping (experimental filter data).

Speaking more generally, the inlaid technology presented here will enable numerous future projects. Currently, three future publications are near completion that each rely on the use of these inlaid cells to obtain measurement data. A variant of the lab-on-chip nitrite sensor introduced in Chapter 3 has already been manufactured to measure phosphate. In the future, this will be applied to nitrate, silicate, ammonium, and various other species as well.

In this thesis, I have demonstrated absorbance and fluorescence configurations using this inlaid design. These two techniques, however, are by no means limiting. The inlaid technology seems suitable for a number of optical techniques. As one example, making a microfluidic flow cytometer using the inlay could be a very interesting future project. I anticipate that this work can provide the foundation for dozens of projects with wide scale and impact.

References

[1] Edward Arthur Luy, Sean Christopher Morgan, Joshua J Creelman, Benjamin J Murphy, and Vincent Joseph Sieben. Inlaid microfluidic optics: absorbance cells in clear devices applied to nitrite and phosphate detection. *Journal of Micromechanics and Microengineering*, 30(9):15, 2020.

[2] H. P. Hansen and F. Koroleff. Determination of nutrients. In *Methods of Seawater Analysis*, pages 159–228. John Wiley & Sons, Ltd, 2007.

[3] Emilio Garcia-Robledo, Alfonso Corzo, and Sokratis Papaspyrou. A fast and direct spectrophotometric method for the sequential determination of nitrate and nitrite at low concentrations in small volumes. *Marine Chemistry*, 162:30–36, May 2014.

[4] Maxime M. Grand, Geraldine S. Clinton-Bailey, Alexander D. Beaton, Allison M. Schaap, Thomas H. Johengen, Mario N. Tamburri, Douglas P. Connelly, Matthew C. Mowlem, and Eric P. Achterberg. A Lab-On-Chip Phosphate Analyzer for Long-term In Situ Monitoring at Fixed Observatories: Optimization and Performance Evaluation in Estuarine and Oligotrophic Coastal Waters. *Frontiers in Marine Science*, 4, 2017.

[5] Porter Hoagland, Donald Anderson, Y. Kaoru, and AW White. The Economic Effects of Harmful Algal Blooms in the United States: Estimates, Assessment Issues, and Information Needs. *Estuaries*, 25:819–837, August 2002.

[6] Ronald C. Antweiler, Charles J. Patton, and Howard E. Taylor. Automated, colorimetric methods for determination of nitrate plus nitrite, nitrite, ammonium and orthophosphate ions in natural water samples. Report 93-638, U.S. Department of the Interior, 1996.

[7] Petra Paiè, Rebeca Martínez Vázquez, Roberto Osellame, Francesca Bragheri, and Andrea Bassi. Microfluidic Based Optical Microscopes on Chip. *Cytometry. Part A : the journal of the International Society for Analytical Cytology*, 93(10):987–996, October 2018.

[8] Hyungkook Jeon, Suhyeon Kim, and Geunbae Lim. Electrical force-based continuous cell lysis and sample separation techniques for development of integrated microfluidic cell analysis system: A review. *Microelectronic Engineering*, 198:55–72, October 2018.

[9] Erin Gross, Hannah Durant, Kenneth Hipp, and Rebecca Lai. Electrochemiluminescence Detection in Paper-Based and Other Inexpensive Microfluidic Devices. *ChemElectroChem*, 4, June 2017.

[10] Anna Tycova, Jan Přikryl, and Frantisek Foret. Recent strategies toward microfluidic-based surface-enhanced Raman spectroscopy. *Electrophoresis*, 38, April 2017.

[11] Douglas B Weibel and George M Whitesides. Applications of microfluidics in chemical biology. *Model systems / Biopolymers*, 10(6):584–591, December 2006.

[12] Bidhan Chandra Dhar and Nae Yoon Lee. Lab-on-a-Chip Technology for Environmental Monitoring of Microorganisms. *BioChip Journal*, 12(3):173–183, September 2018.

[13] Alexander D. Beaton, Christopher L. Cardwell, Rupert S. Thomas, Vincent J. Sieben, François-Eric Legiret, Edward M. Waugh, Peter J. Statham, Matthew C. Mowlem, and Hywel Morgan. Lab-on-Chip Measurement of Nitrate and Nitrite for In Situ Analysis of Natural Waters. *Environmental Science & Technology*, 46(17):9548–9556, September 2012.

[14] Vincent J. Sieben, Cedric F. A. Floquet, Iain R. G. Ogilvie, Matthew C. Mowlem, and Hywel Morgan. Microfluidic colourimetric chemical analysis system: Application to nitrite detection. *Analytical Methods*, 2(5):484–491, 2010.

[15] Jae-Hoon Ahn, Kyoung Jo, and Jong Hahn. Standard Addition/Absorption Detection Microfluidic System for Salt Error-Free Nitrite Determination. *Analytica chimica acta*, 886:114–22, July 2015.

[16] Mohammad F. Khanfar, Wisam Al-Faqheri, and Ala'aldeen Al-Halhouli. Low Cost Lab on Chip for the Colorimetric Detection of Nitrate in Mineral Water Products. *Sensors (Basel, Switzerland)*, 17(10), October 2017.

[17] Pablo González, Nicolás Pérez, and Moisés Knochen. Low Cost Analyzer for the Determination of Phosphorus Based on Open-Source Hardware and Pulsed Flows. *Química Nova*, 39:305–309, 2016.

[18] Gillian Duffy, Ivan Maguire, Brendan Heery, Charles Nwankire, Jens Ducrée, and Fiona Regan. PhosphaSense: A fully integrated, portable lab-on-a-disc device for phosphate determination in water. *Sensors and Actuators B: Chemical*, 246:1085–1091, July 2017.

[19] Yan Chen, Xiao-Liang Guo, Jun-Chao Yan, Yun-Fei Zhao, Yu Pang, Jin-Ming Jian, Michael Morikado, Xiao-Ming Wu, Yi Yang, and Tian-Ling Ren. Toward an In Situ Phosphate Sensor in Natural Waters Using a Microfluidic Flow Loop Analyzer. *Journal of The Electrochemical Society*, 165(14):B737–B745, January 2018.

[20] Jun-Chao Yan, Jun Ren, Lin-Lin Ren, Jin-Ming Jian, Yi Yang, Si-Fan Yang, and Tian-Ling Ren. Development of a portable setup using a miniaturized and high precision colorimeter for the estimation of phosphate in natural water. *Analytica Chimica Acta*, 1058:70–79, June 2019.

[21] Jayan Ozhikandathil, Simona Badilescu, and Muthukumaran Packirisamy. Polymer Composite Optically Integrated Lab on Chip for the Detection of Ammonia. *Journal of The Electrochemical Society*, 165(8):B3078–B3083, January 2018.

[22] Peicong Li, Yao Deng, Huilin Shu, Kunning Lin, Nengwang Chen, Yiong Jiang, Jixin Chen, Dongxing Yuan, and Jian Ma. High-frequency underway analysis of ammonium in coastal waters using an integrated syringe-pump-based environmental-water analyzer (iSEA). *Talanta*, 195:638–646, April 2019.

[23] Gillian Duffy, Ivan Maguire, Brendan Heery, Pauline Gers, Jens Ducrée, and Fiona Regan. ChromiSense: A colourimetric lab-on-a-disc sensor for chromium speciation in water. *Talanta*, 178:392–399, February 2018.

[24] V S Anusuya Devi and V Krishna Reddy. Spectrophotometric Determination of Iron(II) and Cobalt(II) by Direct, Derivative, and Simultaneous Methods Using 2-Hydroxy-1-Naphthaldehyde-p-Hydroxybenzoichydrazone. *International journal of analytical chemistry*, 2012:981758–981758, 2012.

[25] Mazeyar Parvinzadeh Gashti, Jérémie Asselin, Jean Barbeau, Denis Boudreau, and Jesse Greener. A microfluidic platform with pH imaging for chemical and hydrodynamic stimulation of intact oral biofilms. *Lab on a Chip*, 16(8):1412–1419, 2016.

[26] X Cao, S Zhang, D Chu, N Wu, H Ma, and Y Liu. A design of spectrophotometric microfluidic chip sensor for analyzing silicate in seawater. *IOP Conference Series: Earth and Environmental Science*, 82:012080, August 2017.

[27] Tengyue Fang, Peicong Li, Kunning Lin, Nengwang Chen, Yiyong Jiang, Jixin Chen, Dongxing Yuan, and Jian Ma. Simultaneous underway analysis of nitrate and nitrite in estuarine and coastal waters using an automated integrated syringe-pump-based environmental-water analyzer. *Analytica Chimica Acta*, 1076:100–109, October 2019.

[28] Cedric F.A. Floquet, Vincent J. Sieben, Ambra Milani, Etienne P. Joly, Iain R.G. Ogilvie, Hywel Morgan, and Matthew C. Mowlem. Nanomolar detection with high sensitivity microfluidic absorption cells manufactured in tinted PMMA for chemical analysis. *Talanta*, 84(1):235–239, March 2011.

[29] Bruno Costa, Henrique Rezende, Liliam Tavares, Luciana Coelho, Nívia Coelho, Priscila Sousa, and Thais Néri. Application of Flow-Injection Spectrophotometry to Pharmaceutical and Biomedical Analyses. In *Spectroscopic Analyses - Developments and Applications*. IntechOpen, December 2017.

[30] Douglas A. Skoog, Donald M. West, F. James Holler, and Stanley R. Crouch. *Fundamentals of Analytical Chemistry*. Cengage Learning, Belmont, CA, 9th edition, 2014.

[31] Cathy M. Rushworth, Joanna Davies, João T. Cabral, Philip R. Dolan, Jason M. Smith, and Claire Vallance. Cavity-enhanced optical methods for online microfluidic analysis. *Chemical Physics Letters*, 554:1–14, December 2012.

[32] Daniela Giustarini, Ranieri Rossi, Aldo Milzani, and Isabella Dalle-Donne. Nitrite and Nitrate Measurement by Griess Reagent in Human Plasma: Evaluation of Interferences and Standardization. *Methods in enzymology*, 440:361–80, February 2008.

[33] Yanming Shen, Quanjuan Zhang, Xuhong Qian, and Youjun Yang. Practical Assay for Nitrite and Nitrosothiol as an Alternative to the Griess Assay or the 2,3-Diaminonaphthalene Assay. *Analytical Chemistry*, 87(2):1274–1280, January 2015.

[34] Pubchem. Cadmium.

[35] John Brian Mullin and John P. Riley. The spectrophotometric determination of nitrate in natural waters, with particular reference to sea-water. *Analytica Chimica Acta*, 12:464–480, January 1955.

[36] A. Henriksen. An automatic method for determining nitrate and nitrite in fresh and saline waters. *Analyst*, 90(1067):83–88, January 1965.

[37] Katrina M. Miranda, Michael G. Espey, and David A. Wink. A rapid, simple spectrophotometric method for simultaneous detection of nitrate and nitrite. *Nitric Oxide: Biology and Chemistry*, 5(1):62–71, February 2001.

[38] Shoji Motomizu and Zhen-Hai Li. Trace and ultratrace analysis methods for the determination of phosphorus by flow-injection techniques. *Analysis of Phosphorus in Environmental and Agricultural Samples*, 66(2):332–340, April 2005.

[39] François-Eric Legiret, Vincent J. Sieben, E. Malcolm S. Woodward, Samer K. Abi Kaed Bey, Matthew C. Mowlem, Douglas P. Connelly, and Eric P. Achterberg. A high performance microfluidic analyser for phosphate measurements in marine waters using the vanadomolybdate method. *Talanta*, 116:382–387, November 2013.

[40] J. Murphy and J.P. Riley. A modified single solution method for the determination of phosphate in natural waters. *Analytica Chimica Acta*, 27:31–36, January 1962.

[41] Geraldine S. Clinton-Bailey, Maxime M. Grand, Alexander D. Beaton, Adrian M. Nightingale, David R. Owsianka, Gregory J. Slavik, Douglas P. Connelly, Christopher L. Cardwell, and Matthew C. Mowlem. A Lab-on-Chip Analyzer for in Situ Measurement of Soluble Reactive Phosphate: Improved Phosphate Blue Assay and Application to Fluvial Monitoring. *Environmental Science & Technology*, 51(17):9989–9995, September 2017. Publisher: American Chemical Society.

[42] Richard Beck, Min Xu, Shengan Zhan, Hongxing Liu, Richard Johansen, Susanna Tong, Bo Yang, Song Shu, Qiusheng Wu, Shujie Wang, Kevin Berling, Andrew Murray, Erich Emery, Molly Reif, Joseph Harwood, Jade Young, Mark Martin, Garrett Stillings, Richard Stumpf, and Yan Huang. Comparison of Satellite Reflectance Algorithms for Estimating Phycocyanin Values and Cyanobacterial Total Biovolume in a Temperate Reservoir Using Coincident Hyperspectral Aircraft Imagery and Dense Coincident Surface Observations. *Remote Sensing*, 9:538, May 2017.

[43] Claudia Schmid, Robert L. Molinari, Reyna Sabina, Yeun-Ho Daneshzadeh, Xiangdong Xia, Elizabeth Forteza, and Huiqin Yang. The Real-Time Data Management System for Argo Profiling Float Observations. *Journal of Atmospheric and Oceanic Technology*, 24(9):1608–1628, September 2007.

[44] Iain R. G. Ogilvie, Vincent J. Sieben, Matthew Mowlem, and Hywel Morgan. Temporal Optimization of Microfluidic Colorimetric Sensors by Use of Multiplexed Stop-Flow Architecture. *Analytical Chemistry*, 83(12):4814–4821, June 2011. Publisher: American Chemical Society.

[45] The Argo Revolution, NOAA Climate.gov. Last Accessed September 25 2020.

[46] M. Grumann, I. Moser, J. Steigert, L. Riegger, A. Geipel, C. Kohn, G. Urban, R. Zengerle, and J. Ducree. Optical beam guidance in monolithic polymer chips for miniaturized colorimetric assays. In *18th IEEE International Conference on Micro Electro Mechanical Systems, 2005. MEMS 2005.*, pages 108–111, February 2005.

[47] I.R.G. Ogilvie, Vincent Sieben, C.F.A. Floquet, R. Zmijan, Matthew Mowlem, and Hywel Morgan. Solvent processing of PMMA and COC chips for bonding devices with optical quality surfaces. *14th International Conference on Miniaturized Systems for Chemistry and Life Sciences 2010, MicroTAS 2010*, 2:1244–1246, January 2010.

[48] Antonio Liga, Jonathan A. S. Morton, and Maïwenn Kersaudy-Kerhoas. Safe and cost-effective rapid-prototyping of multilayer PMMA microfluidic devices. *Microfluidics and Nanofluidics*, 20(12):164, November 2016.

[49] Arshya Bamshad, Alireza Nikfarjam, and Hossein Khaleghi. A new simple and fast thermally-solvent assisted method to bond PMMA–PMMA in micro-fluidics devices. *Journal of Micromechanics and Microengineering*, 26(6):065017, May 2016.

[50] Holger Becker and Claudia Gärtner. Polymer microfabrication methods for microfluidic analytical applications. *Electrophoresis*, 21(1):12–26, January 2000. WOS:000085065800003.

[51] Adrian M. Nightingale, Sammer-Ul Hassan, Gareth W.H. Evans, Sharon M Coleman, and Xize Niu. Nitrate measurement in droplet flow: Gas-mediated crosstalk and correction. *Lab on a Chip*, 18, June 2018.

[52] Nerdy Nerdy and Effendy De Lux Putra. Spectrophotometric Method for Determination of Nitrite and Nitrate Levels in Broccoli and Cauliflower with Different Fertilization Treatment. *Oriental Journal of Chemistry*, 34:2983–2991, December 2018.

[53] Sammer-ul Hassan, Adrian M. Nightingale, and Xize Niu. Micromachined optical flow cell for sensitive measurement of droplets in tubing. *Biomedical Microdevices*, 20(4):92, October 2018.

[54] W. Gomes. Spectrophotometric determination of nitrite and nitrate in doped potassium chloride crystals. *Fresenius' Zeitschrift für analytische Chemie*, 216(4):387–391, December 1966.

[55] Lisa A. Ridnour, Julia E. Sim, Michael A. Hayward, David A. Wink, Sean M. Martin, Garry R. Buettner, and Douglas R. Spitz. A Spectrophotometric Method for the Direct Detection and Quantitation of Nitric Oxide, Nitrite, and Nitrate in Cell Culture Media. *Analytical Biochemistry*, 281(2):223–229, June 2000.

[56] Bernhard Schnetger and Carola Lehners. Determination of nitrate plus nitrite in small volume marine water samples using vanadium(III)chloride as a reduction agent. *Marine Chemistry*, 160:91–98, March 2014.

[57] John Cleary, Conor Slater, and Dermot Diamond. Field-deployable microfluidic sensor for phosphate in natural waters. In *SENSORS, 2007 IEEE*, pages 1001–1004. IEEE, October 2007.

[58] Alankar Shrivastava. Methods for the determination of limit of detection and limit of quantitation of the analytical methods. *Chronicles of Young Scientists*, 2:21–25, June 2011.

[59] Arne S. Kristoffersen, Svein R. Erga, Børge Hamre, and Øyvind Frette. Testing Fluorescence Lifetime Standards using Two-Photon Excitation and Time-Domain Instrumentation: Rhodamine B, Coumarin 6 and Lucifer Yellow. *Journal of Fluorescence*, 24(4):1015–1024, July 2014.

[60] Mariana Beija, Carlos A. M. Afonso, and José M. G. Martinho. Synthesis and applications of Rhodamine derivatives as fluorescent probes. *Chemical Society Reviews*, 38(8):2410–2433, 2009. Publisher: The Royal Society of Chemistry.

[61] Yang Jiao, Lu Zhou, Haiyang He, Jiqiu Yin, Qianmiao Gao, Junnan Wei, Chunying Duan, and Xiaojun Peng. A novel rhodamine B-based "off-on" fluorescent sensor for selective recognition of copper (II) ions. *Talanta*, 184:143–148, July 2018.

[62] Hugh Macintyre and John Cullen. Classification of phytoplankton cells as live or dead using the vital stains fluorescein diacetate and 5-chloromethylfluorescein diacetate (FDA and CMFDA). *Journal of Phycology*, 52:n/a–n/a, March 2016.

[63] Hugh L. MacIntyre, John J. Cullen, Trina J. Whitsitt, and Brian Petri. Enumerating viable phytoplankton using a culture-based Most Probable Number assay following ultraviolet-C treatment. *Journal of Applied Phycology*, 30(2):1073–1094, April 2018.

[64] Barbara Poniedziałek, Halina Falfushynska, and Piotr Rzymski. Flow cytometry as a valuable tool to study cyanobacteria: A mini-review. *Limnological Review*, 17:89–95, June 2017.

Appendix A

Calculating Light Absorbance with Background

This appendix provides more context to the discussion in the Theory section of Chapter 3 and is taken almost verbatim from the supplemental material of Edward Arthur Luy, Sean Christopher Morgan, Joshua J Creelman, Benjamin J Murphy, and Vincent Joseph Sieben. Inlaid microfluidic optics: absorbance cells in clear devices applied to nitrite and phosphate detection. *Journal of Micromechanics and Microengineering*, 30(9):15, 2020.

The Beer-Lambert law states that the light-absorbance of a fluid can be calculated by directing light through the fluid and comparing its incident to transmitted intensity. Assuming the incident light has an intensity of I_0 and the transmitted beam has an intensity I, the absorbance A of the fluid can be calculated such that $A = -\log_{10}(I/I_0)$. Typically, light-to-voltage converters (photodiodes) are used to measure absorbance by converting light intensity into a proportional voltage. When photodiodes are used, the voltage outputs can be used with the Beer-Lambert law to calculate absorbance such that,

$$A = -\log_{10}\left(\frac{V}{V_0}\right), \tag{A.1}$$

where V is the voltage produced by a light-to-voltage converter when measuring light that has passed through the sample and V_0 is the blank reference. From this point onwards, it will be assumed that any log term has base 10.

In practice, however, photodiode measurements will be offset by the amount of background light detected during these measurements, *i.e.* light that reaches the detector without passing through the sample. With other designs, it is possible that the photodiode may detect light which has partially travelled through the sample (*i.e.* passes through the optical channel diagonally towards the detector), but out inlay prevents this from ever happening as the opaque surrounds will attenuate such rays. Therefore, the voltage produced by the photodiode when measuring samples or blanks is offset by the background light at each measurement:

$$V_{P,S} = V + V_{bg} \qquad V_{P,B} = V_0 + V_{bg}, \tag{A.2}$$

where $V_{P,S}$ and $V_{P,B}$ are the photodiode voltage readings produced when measuring samples or blanks respectively. The quantity V_{bg} corresponds to the voltage output that the photodiode would produce when measuring only background light. With regards to Chapter 3, $V_{P,S}$ and $V_{P,B}$ correspond to the raw voltage time-series data collected during a light-absorbance trial (as in Figure 3.10). Under the case where there is no background light, $V_{P,S}$ and $V_{P,B}$ can be used directly with equation (A.1) to calculate absorbance. When background is measured by the photodiode, however, it must be subtracted off:

$$A_{Corr} = -\log\left(\frac{V_{P,S} - V_{bg}}{V_{P,B} - V_{bg}}\right). \tag{A.3}$$

Equation (A.3) can be used directly to calculate the light absorbance of a sample with correction for any detected background. However, it is sometimes useful to quantify the correction term itself: the difference between A and A_{Corr}. Equation (A.3) can be factored such that:

$$A_{Corr} = -\log\left(\frac{V_{P,S}(1 - V_{bg}/V_{P,S})}{V_{P,B}(1 - V_{bg}/V_{P,B})}\right), \tag{A.4}$$

and, making use of the logarithm identities $\log(AB) = \log(A) + \log(B)$ and $-\log(A) = \log(A^{-1})$, equation (A.4) can then be re-written as:

$$A_{Corr} = -\log\left(\frac{V_{P,S}}{V_{P,B}}\right) + \log\left(\frac{1 - V_{bg}/V_{P,S}}{1 - V_{bg}/V_{P,B}}\right)^{-1}. \tag{A.5}$$

Recall that the first term is equal to the uncorrected absorbance A and that $\log(A^{-1}) = \log(1/A)$; equation (A.5) can then be re-expressed in terms of the uncorrected absorbance plus an offset:

$$A_{Corr} = A + \log\left(\frac{1 - V_{bg}/V_{P,B}}{1 - V_{bg}/V_{P,S}}\right) = A + \delta, \tag{A.6}$$

where A is the uncorrected absorbance, *i.e.* the absorbance that would be calculated if the photodiode measurements were used with the Beer-Lambert law without considering background influences. The corrected absorbance measurement A_{corr} is equal to the sum of the uncorrected absorbance A plus an offset $\delta = \log\left(\frac{1-V_{bg}/V_{P,B}}{1-V_{bg}/V_{P,S}}\right)$. In the main text, the quantities $V_{P,B}$ and $V_{P,S}$ are simply referred to as V_0 and V.

We now seek to prove that the offset term δ is always non-negative or, consequently, that the corrected absorbance is either equal to or greater than the uncorrected absorbance. Firstly, under the special case of zero background, the modified Beer-Lambert law should reduce to the usual Beer-Lambert law. Evaluating equation (A.6) with $V_{bg} = 0$ yields:

$$A_{Corr} = A + \log\left(\frac{1-0}{1-0}\right) = A + \log(1) = A,$$

and no correction is needed as expected. A final special case exists; assuming V_{bg} remains constant, the equation (A.6) reduces to equation (A.1) when $V_{P,B} = V_{P,S}$ (*i.e.* when measuring a sample with zero absorbance):

$$A_{Corr} = A + \log\left(\frac{1 - V_{bg}/V_{P,B}}{1 - V_{bg}/V_{P,S}}\right)^{-1} = -\log(1) + \log(1) = 0 = A,$$

and thus no correction is needed for samples with zero absorbance assuming V_{bg} remains constant between both measurements. When either of the two conditions above are met, $\delta = 0$ and equation (A.1) may be used directly. This can be summarized in the following statement:

$$V_{bg} = 0 \vee V_{P,B} = V_{P,S} \longrightarrow A_{Corr} = A$$

If neither of these conditions are met, $\delta > 0$ and the corrected absorbance measures higher than without correction. Firstly, we must note that $V_{P,S}$ should not measure higher than $V_{P,B}$ since the reference should be a colourless blank that allows maximum light detection. In practice, a sample may momentarily transmit more light than a blank due to blank contamination or Schlieren mixing effects, but these will be ignored as this scenario would produce a negative absorbance value for the sample which is invalid. The scenario in which $V_{P,S}$ and $V_{P,B}$ are equal has already been discussed above, so we continue with the assumption that

$$V_{P,S} < V_{P,B}, \tag{A.7}$$

as a sample should block more light from reaching the detector than a colourless blank. With this assumption and recalling that $V_{bg} \neq 0$, it follows directly from equation (A.7) that:

$$V_{P,S} < V_{P,B} \tag{A.8a}$$
$$1/V_{P,S} > 1/V_{P,B} \tag{A.8b}$$
$$V_{bg}/V_{P,S} > V_{bg}/V_{P,B} \tag{A.8c}$$
$$-(V_{bg}/V_{P,S}) < -(V_{bg}/V_{P,B}) \tag{A.8d}$$
$$1 - (V_{bg}/V_{P,S}) < 1 - (V_{bg}/V_{P,B}) \tag{A.8e}$$
$$1 < \frac{1 - (V_{bg}/V_{P,B})}{1 - (V_{bg}/V_{P,S})} \tag{A.8f}$$
$$0 < \log\left(\frac{1 - (V_{bg}/V_{P,B})}{1 - (V_{bg}/V_{P,S})}\right) \tag{A.8g}$$
$$0 < \delta \tag{A.8h}$$

where equation (A.8c) requires that $V_{bg} \neq 0$ (recall that $V_{bg} < 0$ is impossible). Since it has been shown that $\delta > 0$, it follows from equation (A.6) that $A_{Corr} - A > 0$ and therefore $A_{Corr} > A$ as claimed. This can be summarized by the following logical statement:

$$V_{bg} \neq 0 \wedge V_{P,B} \neq V_{P,S} \longrightarrow A_{Corr} > A.$$

When measuring the light-absorbance of a fluid, equation (A.1) may be used if there is no background or if the sample does not absorb more than the blank. In practice, neither of these conditions are typically met. Otherwise, equation (A.6) must be used as equation (A.1) will calculate artificially-low absorbance values.